Università degli Studi di Salerno

Dipartimento di Ingegneria dell'Informazione ed Ingegneria Elettrica

Dottorato di Ricerca in Ingegneria dell'Informazione
IX Ciclo – Nuova Serie

TESI DI DOTTORATO

Modelling and Performance Analysis of A Neurostimulation System

CANDIDATA: **SIMONA ELIA**

TUTOR: **PROF. VINCENZO TUCCI**

CO-TUTOR: **ING. PATRIZIA LAMBERTI**

COORDINATORE: **PROF. ANGELO MARCELLI**

Anno Accademico 2009 – 2010

"*The important thing is not to stop questioning*."
Albert Einstein

A tutte le persone che amo e da cui sono amata.

Acknowledgments

Un ringraziamento di cuore va al Prof. Tucci, al Prof. Egiziano e all'Ing. Lamberti, per la disponibilità e il supporto con cui in questo periodo di studio hanno fatto crescere in me la voglia di maturare e di prendere consapevolezza dei miei pregi, per potenziarli e dei miei limiti, per superarli.

Un sincero grazie va poi a Biagio De Vivo e a Raffaele Raimo, con cui ho condiviso bei momenti di serenità e che mi hanno spesso stimolato con riflessioni di vita sempre affettuose e partecipi.

Un grazie davvero speciale va al Dott. Antonio Starita per il "supporto tecnico" che mi ha dato e per le "illuminanti perle di saggezza informatica".

Un grazie va ad Annamaria, una persona speciale che ha saputo interpretare questo periodo della mia vita con la simpatia, il garbo e la generosità, che solo i veri amici sanno dimostrare.

Grazie alla mia famiglia che mi ha lasciato essere chi sono, sopportando anche qualche "leggera" intemperanza, ma sempre vicina nel momento del bisogno.

Un grazie profondo e velato di una certa malinconia, va, poi, a chi in vario modo ha intrecciato le sue vicende personali con le mie in questo intenso periodo presso l'Università di Salerno, con la consapevolezza che tutto ciò che le persone ci lasciano è sempre prezioso bagaglio e le fa vivere dentro di noi anche quando la vita ci tiene lontano.

Grazie davvero.

Table of Content

List of Tables

List of Figures

Chapter 1

Introduction

1.1 Interest of the matter

Computational modelling and analysis in biology and medicine have received major attention in recent years. The interdisciplinary efforts developed so far aimed at elucidating structures and functions of living systems with major challenges in computational modelling and analysis to understand, analyze and predict the complex mechanisms of biological systems. Continued research investigations in computational biology and physiology have addressed important issues across many applications spanning from molecular dynamics, biological signalling pathways, cellular biology and communication, tissue mechano-biology, organ function and performance, systemic auto regulation, all the way up to lifestyle and environmental influences and behavioural responses. Researchers are now beginning to address the grand challenge of multi-scale computational modelling and analysis: effectively capturing biological and physiological interdependencies across multiple observational scales –not only in time and space, but also in physiochemical modality– and doing so in a computationally efficient manner. The development of many such models involves the design of multimodal data acquisition instrumentation and systems capable of measuring and monitoring of structural and functional properties in vivo and in minimally invasive manner [1],[2]. Over the last few years, the research work is being extended not only to further improve the basic understanding of biological and physiological models but also to explore translational biomedical research. For example, multi-scale and multi-modal modelling approaches are now paving the way to better understanding of the mechanisms of disease and its treatment, thus helping to

establish diagnostic biomarkers, physiology-based patient selection criteria, and more principled strategies for choosing, personalizing and optimizing therapeutic options.

Multi-scale computational modelling [3] promises to become a fundamental contributor to future biomedical sciences and technologies, and personalised predictive healthcare.

In particular, current and emerging neural prostheses and therapies based on nerve stimulation and recording involve electrodes chronically interfaced to the central and peripheral nervous systems.[4]-[11] Applications include theoretical understanding on how networks of neurons develop over time and change in response to stimuli. Because of the interest in this field, many scientific studies have been carried out of neural development and plasticity focus on the spatiotemporal dynamics of neural activity.

Although neurons are complex electrochemical systems, they encode a large portion of the information that they process in quick voltage transients, known as action potentials (APs) [12]; thus, the ability to accurately measure the effects of stimulating and recording neural tissue main activities is essential to many scientific and engineering efforts.

From a much more practical point of view, other applications include upper and lower limb prostheses for spinal cord injury [13] and stroke; bladder prostheses, cochlear and brain-stem auditory prostheses, cortical recording for cognitive control of assistive devices [10], vagus nerve stimulation for epilepsy and depression and deep brain stimulation (DBS) ([14]-[17]) for essential tremor, Parkinson's disease, epilepsy, dystonia or depression, as well as the design of biosensors for research aims and retinal and cortical visual prostheses.

All these research fields strongly require electrodes characterized by low impedance for recording or safe reversible charge injection for stimulation.

In particular, as far as retinal prosthetics are concerned, since photoreceptors may degenerate or cease to exist, as in age-related macular degeneration (AMD) and in retinitis pigmentosa (RP), leading to partial or complete blindness, great effort in research field([18],[27]), indeed, has been taken in the last years to tailor devices, capable of partly restoring sight, bypassing the

photoreceptors retinal layer[28].

There are two main approaches to retinal implants currently being studied by scientists across the globe; *subretinal* and *epiretinal* [29]. The subretinal approach [19],[24],[30] involves implanting the chip underneath the retina, specifically in the macular region. In this case, the macular region is believed to be the ideal location because this is the most sensitive area, which is responsible for producing clear images in sighted people. Instead, the epiretinal approach involves placing the chip on top of the macular region of the retina and requires additional equipment—like cameras or special glasses—to properly function.

Therefore, while *subretinal* prosthesis relay signals to the bipolar cells, *epiretinal* ones pass them directly to the ganglion cells, in turn, carrying them to specific brain areas for elaboration.

Focalizing on this latter case, passing through various stages of development, since the 70s-80s, plenty of studies have been conducted on arrays of microelectrodes (MEAs) [4],[30], for interfacing with the Central Nervous System (CNS) in general and with retina, in particular. Nevertheless, because of this technology intrinsic limitations (large size of the electrodes, causing pour spatial resolution, lack of control on the local electrical and chemical activity of axons and their neurotransmitters as well as the open-loop nature of the stimulation), new solutions have been sought and have emerged recently, thanks to the ongoing development of nanotechnology [1],[31]-[38].

In addition to this, for further improving retinal stimulation effectiveness, other constraints must be taken into account, concerning its main electrophysiological features.

Since as we will briefly discuss in Chapter 2, retina performs an *encoding* (compression) of images to fit the limited capacity of the optic nerve and this is necessary since there are almost one hundred times more photoreceptors than ganglion cells. Indeed, in correspondence with *fovea* (retinal area responsible for sharp central vision, necessary for any activity where visual detail is strongly required) there are relatively few ganglion cells, leading APs to brain areas through their axons (Fig. 1).

Moreover, an increase in stimulation intensity does not proportionally change the intensity of the singular AP (which depends

non linearly by various parameters), but it is, instead, translated into an increase in the number of transmitted pulses per unit of time (*all-or-nothing* axon response, frequency codification).
This implies that, especially in epiretinal stimulation devices, the primary goals are multiple.

First of all they can be identified in gaining *axon spatial selectivity* [39], as well as in the ability to *elicit APs as readily as possible*: in response to a change of the visual scenario the coded information the neuron has to carry to the brain changes and thus the ideal triggering should be as prompt as possible, because instead information distortion can be generated.

This objective is, in turn, in trade-off with the other fundamental aim: the respect of axonal refractory periods, which prevent, after a first AP elicitation, a further excitation stimuli to be effective in producing new APs. Thus, it is clear how, especially in ganglion axons stimulation, in order to reduce information distortion, it is of paramount importance to accurately (and possibly systematically) investigate the effectiveness that the excitation instrumentation gains when it is interfaced with the cells. In literature, indeed, as we have seen, many investigations can be found differently addressing the topic of the neurostimulation and its effectiveness but less is done to precisely evaluate nanoscale effects (the system has intrinsically high nonlinearities thus severe reduction in some of its geometrical parameters -nanoelectrode vs microelectrode- are likely to lead to different system responses) or to approach the topic from a more analytical/systematic point of view.

1.2 Finite Element modelling and sensitivity analysis on the neurostimulating system

This thesis is focussed on the description of the main results obtained applying Design of Experiment procedures on Finite Element Method (FEM) models, on purpose implemented, of a simple neurostimulating nanoelectrode system. Thus particular focus is cast on the description of the activity devoted to obtain the model tools on which to perform the investigations and on the study of the system performances.

Furthermore, the nanoelectrode system is thought as a constitutive part of a nanoporous alumina (biocompatible) layer supporting the growth of nanoelectrodes, realizable with a bundle of MWCNTs, in interface with neural cells.

The implemented models are, indeed, different, depending on the neuron or system most prominent feature that was necessary to highlight and observe.

In particular, once defined the desired performance functions of the system (the elicitation of the APs, the speed at which this phenomenon starts when it starts, the space resolution of the neurostimulating stress), Response Surface Methodology (within the theoretical context of the Design of Experiments) is exploited to deduce particularly meaningful information on the system dynamics and on the most significant factors leading them.

The 3D FEM models range from a “nanostimulated” axon segment, to a whole complex structure constituted by soma, axon hillock and the very first segment of the departing axon, built in order to evaluate geometrical parameters and ionic channels distributions affecting APs activation. In the end, a system made up of a couple of axons is implemented to obtain a tool where it is possible to verify the space resolution (space selectivity among fibres) gained in the neurostimulation performed.

Chapter 2

A brief review on retina and neuron electrophysiology

The retina in vertebrates is a light sensitive tissue covering the inner surface of the eye. The optical properties characterizing the eye are capable of creating an image of the on the retina, operating as the film in a camera. As previously said, when the light strikes this tissue, it initiates a sequence of chemical and electrical events that end by activating nerve impulses. Optic nerve then sends them to various visual centers of the brain, by means of the fibers it contains. Since during the embryonic development the retina and the optic nerve originate as outgrowths of the developing brain, retina is considered part of the central nervous system (CNS), constituting the only part of it that can be visualized in a non-invasive manner. The structure of this tissue is a complex superimposition of several layers of neurons interconnected by synapses. However, the only neurons directly sensitive to light are the photoreceptor cells: they can be classified in two subtypes, rods and cones. The first one work mainly in dim light and provide black-and-white vision, while cones are the main actors in daytime vision and in the perception of colours. The cones respond to bright light and mediate high-resolution colour vision during daylight illumination (also called "photopic" vision). The rods are saturated at daylight levels and don't contribute to pattern vision. However, rods do respond to dim light and mediate lower-resolution, monochromatic vision under very low levels of illumination (called "scotopic" vision), There is also another, less common type of photoreceptor, the photosentitive ganglion cell, which is important for reflexive responses to bright daylight. Neural signals from the rods and cones undergo a complex processing sequence by other neurons belonging to the retina itself . The output is in the form of APs in retinal ganglion cells axons. Several important features of visual perception can be

traced to the retinal encoding and processing of light.

2.1 Anatomy of vertebrate retina

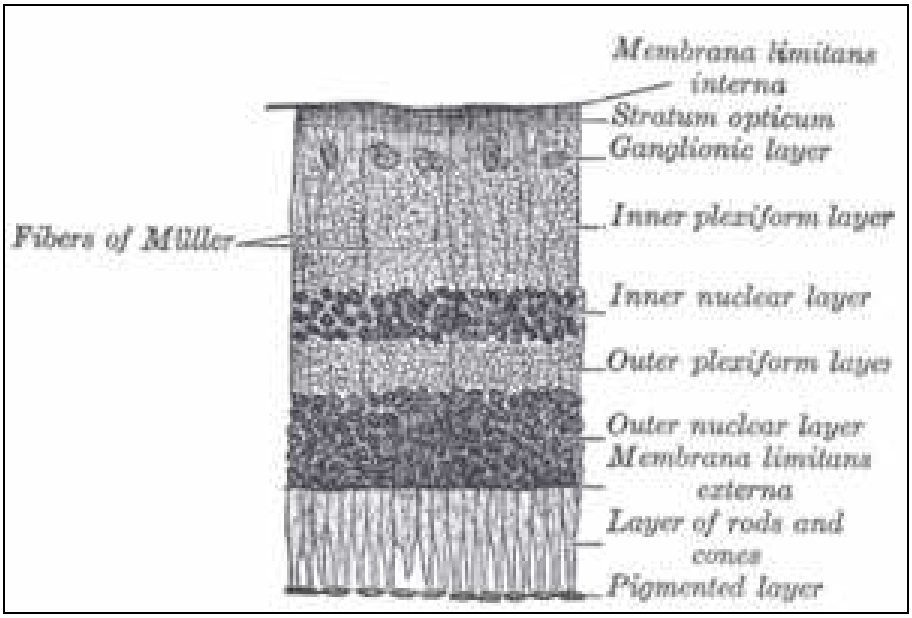

Fig. 1 Section of retina. [40]

From innermost to outermost, the ten retinal layers include:

- Inner limiting membrane - Müller cell footplates
- Nerve fiber layer - Essentially the axons of the ganglion cell nuclei.
- Ganglion cell layer - Layer that contains nuclei of ganglion cells and gives rise to optic nerve fibers.
- Inner plexiform layer.
- Inner nuclear layer contains bipolar cells, which correspond to heat and touch sensory skin receptors, capable of transmitting signals to the spinal cord or its continuation, the medulla.
- Outer plexiform layer
- Outer nuclear layer
- External limiting membrane - Layer that separates the inner

segment portions of the photoreceptors from their cell nucleus.

- Photoreceptor layer - Rods and Cones
- Retinal pigment epithelium

Of these the four main layers of the ten, from outside in: pigment epithelium, the photoreceptor layer, bipolar cells, and finally, the ganglion cell layer. Therefore, the optic nerve is less a nerve than a central tract, connecting the bipolars to the lateral geniculate body, a visual relay station in the diencephalon (the rear of the forebrain). In adult humans the entire retina is approximately 72% of a sphere about 22 mm in diameter. An area of the retina is the optic disc, sometimes known as "the blind spot" because it lacks photoreceptors. It appears as an oval white area of 3 mm^2. In the direction of the temples there is the macula. At its centre is the fovea, a pit most sensitive to light and responsible for our sharp central vision. Around the fovea extends the central retina for about 6 mm and then the peripheral retina. In section the retina is no more than 0.5mm thick. It has three layers of nerve cells and two of synapses, including the unique ribbon synapses. The optic nerve carries the ganglion cell axons to the brain and the blood vessels that open into the retina. The ganglion cells lie innermost in the retina while the photoreceptive cells lie outermost. Because of this counter-intuitive arrangement, light must first pass through and around the ganglion cells and through the thickness of the retina, (including its capillary vessels) before reaching the rods and cones. However it does not pass through the epithelium or the choroid (both of which are opaque). Between the ganglion cell layer and the rods and cones there are two layers of neuropils where synaptic contacts are made. The neuropil layers are the outer plexiform layer and the inner plexiform layer. In the outer the rods and cones connect to the vertically running bipolar cells, and the (horizontally oriented) horizontal cells connect to ganglion cells. The central retina is cone-dominated and the peripheral retina is rod-dominated. In the central macular fovea zone the cones are smallest and arranged in a hexagonal mosaic, the most efficient and highest density.The area directly surrounding the fovea has the highest density of rods converging on single bipolars. Since the cones have a much lesser power of merging signals, the fovea allows for the sharpest vision the eye can attain .Since, as we said there are much more receptors than optic nerve fibers, and the horizontal action of the horizontal and

amacrine cells can allow one area of the retina to control another (e.g., one stimulus inhibiting another), the messages are merged and mixed. An image is produced by the "patterned excitation" of the cones and rods in the retina. The information retina sends is processed by the neuronal system and various parts of the brain working in parallel to form a representation of the external environment. The response of cones to various wavelengths of light is called their “spectral sensitivity”. In normal human vision, the spectral sensitivity of a cone falls into one of three subgroups. These are often called "red, green, and blue" cones but more accurately are short, medium, and long wavelength sensitive cone subgroups. When light falls on a receptor it sends a proportional response synaptically to bipolar cells which in turn signal the retinal ganglion cells. The receptors are also 'cross-linked' by horizontal cells and amacrine cells, which modify the synaptic signal before the ganglion cells. In the retinal ganglion cells there are two types of response, depending on the receptive field of the cell. Since there are more retinal receptors, than axons in the optic nerve; a large amount of pre-processing is performed within the retina. The fovea produces the most accurate information. Despite occupying about 0.01% of the visual field (less than 2° of visual angle), about 10% of axons in the optic nerve are devoted to the fovea. The resolution limit of the fovea has been determined at around 10,000 points. The information capacity is estimated at 500,000 bits per second without colour or around 600,000 bits per second including colour. The retina, unlike a camera, does not simply send a picture to the brain. It spatially *encodes* (compresses) the image to fit the limited capacity of the optic nerve. We remind that compression is necessary because there are 100 times more photoreceptors cells than ganglion cells as mentioned above. The retina does so by "decorrelating" the incoming images. These operations are carried out by the center surround structures as implemented by the bipolar and ganglion cells. Finally, the horizontal and amacrine cells play a significant role in this process. Once the image is spatially encoded by the center surround structures, the signal is sent out the optical nerve (via the axons of the ganglion cells) through the optic chiasm to the LGN (lateral geniculate nucleus) and then to the V1 Primary visual cortex.

2.2 Anatomy of vertebrate retina: the nervous cell

The nerve cell [41] can be divided into four different zones in terms of morphological features: cell body (soma), dendrites, axon and presynaptic axon terminals, each playing a particular role in the genesis of nerve signals. The cell body (soma) is the metabolic center of the neuron, gives rise to two types of extensions, axon and dendrites, which branch off as a harborization from the cell body and the human body apparatus are intended to receive the messages arriving to the neuron from other nerve cells The cell body also gives rise to the axon is a cylindrical process, with a diameter (in humans) from 0.2 to 20 μm. It is also capable of transmitting information over long distances by propagating an electrical signal of all-or-nothing of very short duration, called indeed the Action Potential; it is the major route of conduction of the signals of the neuron. Once the transmembrane voltage has reached the critical threshold, an AP is typically generated at a specialized area where the axon originates, the axon hillock. The axon is divided into many thin branches, each of which has specialized swellings, called presynaptic terminations, which are the support for messages transmission.

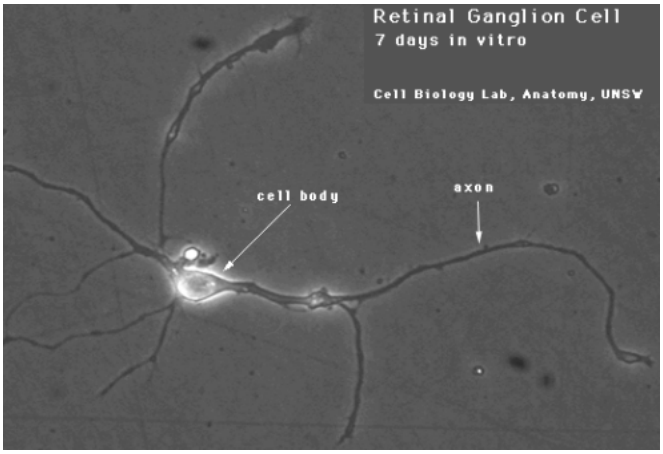

Fig. 2 The nervous cell

It is through these terminals that neurons transmit information about its activities at the interfaces of other neurons (dendrites and cell

bodies). The “contact” points are called synapses and therefore the cell that transmits the information is that the presynaptic cell, while the receiving is called postsynaptic. Between the two there is a space called the synaptic cleft, which communicates freely with the extracellular space. Most of the presynaptic neurons finish close to the postsynaptic dendrites of the neuron but contact between neurons can be sometimes with the soma or, less frequently, with axon initial or terminal segment.

Chapter 3

Modelling of the Neurostimulation System

3.1 Neurostimulation system issues and choices

Carbon nanotubes are attractive as neural electrodes because of a very wide range of reasons. A very high Electrical Superficial Area / Geometrical Superficial Area ratio, (ESA/GSA), is inherent in the nanotube geometry, which gives rise to a large double-layer charge capacity; for neural stimulation: in literature charge-injection capacities have been found of 1–1.6 mC cm^{-2} with vertically aligned nanotube electrodes. Works on the development of nanotube and nanofibre neural interfaces have been reported, as introduced in Chapter 1. The discovered excellent biocompatibility of carbon nanotubes, especially with CNS, [42]-[44], has paved the way for deeper investigation into the possibility of using them to improve microelectrode performances or even to obtain nanoelectrodes. Moreover, microelectrodes coated with CNTs have been proposed [36] , in order to obtain a rougher surface, providing a better electrical coupling with the cells. Furthermore, thanks to their additional properties (high mechanical resistance and electrical conductivity, extremely small diameters, good experienced Signal-to-Noise-Ratio and capability to be functionalized and to be used as neurotransmitters sensors), CNTs have been suggested as strongly efficient nanoelectrodes [31]-[38].The resulting advantages are clearly understood: tri-modal Nanoelectrode Arrays (NEA) have been investigated in [33], allowing much higher spatial resolution for the electrical stimulation and capability of recording and monitoring of neurotransmitters levels (closed-loop control). Carbon nanotubes may also be chemically modified to enhance biocompatibility or provide

other functional properties (they are even investigated in literature as anticorrosive coating agents for general purpose metallic electrodes [45]).Their usage, thus, deeply favours quantitative improvement of the neurostimulating apparatus and outperforms the metallic more corruptible metallic electrodes.

These are the reasons why we have chosen to investigate the properties of a system realizable with CNT based nanoelectrodes.

Another particularly meaningful issue to decide for has been the type of modelling approach.

3.1.1 The necessity of a modeling approach

Keeping in mind the objective of this work, it is clear that it is of paramount importance to develop an accurate mathematical model to the entire system. We are moving within the field of virtual engineering (specifically applying DoE- Design of Experiments-techniques), in order to benefit of all its advantages. In particular, virtual engineering integrates geometric models and related engineering tools such as analysis, simulation, eventual optimization and decision making tools, etc., within a computer-generated environment that facilitates multidisciplinary product development. This requires a model that includes the geometry, physics, and any quantitative or qualitative data from the real system, so that is possible to observe how it works and how it responds to changes in design, operation or any other engineering modification. A model requires selecting and identifying *relevant* aspects of a situation in the real world and exploits mathematical language. In this way, the real system can be analyzed, in order to be controlled or optimized, using the mathematical model to take into account its peculiar and most meaningful features and to try to estimate how an unforeseeable event could affect it. The system is described by a set of variables and of equations that establish relationships between the variables, representing some properties of the system, for example, signals or events occurrence. The actual model is the set of functions that describe the relations between the different variables, classifiable as decision, input, state, exogenous, random and output variables. Different system constraints and objective functions (also called indexes of performance) can be identified whose interest strongly

depends on the specific application. Mathematical models can be classified in *linear (*or *nonlinear), deterministic (*or *stochastic), static* (*or dynamic).* In general, model complexity involves a trade-off between simplicity and accuracy. Occam's Razor is a principle particularly relevant to modelling; the essential idea being that among models with roughly equal predictive power, the simplest one is the most desirable. While added complexity usually improves the realism of a model, it can make it difficult to understand and analyze, and can also pose computational problems, including numerical instability.

3.1.2 The field solution and the Finite Element Method adoption

As far as this thesis work is concerned, our choice has been to model the reality under study by means of a nonlinear, deterministic and dynamic model, taking into account the nature of the reality to emulate. In particular, it has been necessary to decide which was the best modelling technique to capture the main features of the problem under analysis. We have opted for a field solution model and the Finite Element Method to implement it. Very often in literature the matter is addressed by using biomolecular or compartmental approaches .[3],[46]-[48]. Indeed, it is very difficult to (e.g.) “tailor” appropriate density fluxes lines for currents or electric field lines or analyzing systematically different electrode configurations, adopting biomolecular or compartmental typical modelling solutions. The first one has a much deeper and detailed breath than what is necessary for our investigation: it is focused more on the study of proteins, properties of enzymes, metabolic pathways, than on their interactions with the applied electric fields and the higher scale phenomena related, making it very uneasy to explore the performances we wanted to explore. For the second classically used model, the compartmental, it must be said that one of its big disadvantages (evidenced in many models used so far) is that on the one hand it is not possible to simulate the interaction between activated fibres and the surrounding tissue (making the implemented models less extensible and thus less useful), on the other hand it is very difficult to integrate geometrical aspects and time dependency.

Thus, within this thesis work, our choice has fallen on the field solution (which has started to be more appreciated in the last years also thanks to greater power of calculus), because it allows to overcome all the cited troubles, especially in the flexible and manageable FEM implementation [8]. We are, thus, enabled to couple, quite simply, multiphysical parameters and descriptive equations into a whole system and to have the opportunity to quite easily make parametric geometrical variations and adaptations.

In the end, our modelling of neuron membrane highly nonlinear behaviour has been based on the set of equations that the two Nobel Prizes, A. L. Hodgkin and A. F. Huxley, published [49], paving the way for the research in the field. Their mathematical theory on neural membrane electrophysiology uncovered the gating mechanisms in axons and represents a milestone in understanding and modelling the excitation and spike propagation in nerve and muscle fibres. Therefore it is by far the most broadly adopted in literature to simulate neural activities [12]. These equations, indeed, once coupled with Maxwell equations for electromagnetic fields, represent the suitable tool for describing sufficiently accurately neuron response to nanoelectrode stimulation. In particular, since the typical frequencies involved in neural stimulation are quite low, their quasi static formulation has been adopted. Finally, in the next subsection a brief overview of the Finite Element Method is reported to better clarify its advantages and the reasons of its choice, while the subsequent sections of the chapter follow the modelling phases. Once obtained the 2D representation of the main axon features, we have proceeded (following a a step by step procedure) towards the implementation of a valid 3D model tool, which is supposed to take into account more sophisticated and spatially differentiated neuron operating conditions.

3.1.2.1 Notes on the theory of FEM

The finite element method (FEM) is a very widely adopted numerical technique employed to obtain approximate solutions to partial differential equations (PDE) and to integral ones. Euler's and Runge-Kutta method together with other standard techniques are used to perform numerical integration for solving the ordinary differential system of equations (ODE) in which the PDE are approximated.

Indeed, in this context, the primary goal is to determine equations that approximate those under study, with the constraint of a good numerical stability. This means that errors in the input and in the intermediate calculations phases should not accumulate, causing the resulting output to be less meaningful or meaningless at all. In literature there are various possible techniques, but FEM is a good choice for solving partial differential equations over complicated or time changing domains, when the desired precision varies over the entire domain or when the solution lacks smoothness. This paragraph very briefly describes how the FEM approximates the PDE problem with a problem that has a finite number of unknown parameters, leading to a discretization of the original problem. To do so an introduction must be done to finite elements and shape functions, that describe the possible forms of the approximate solution.
The starting point for the finite element method is a mesh, a partition of the geometry into small units of a simple shape: mesh elements. Different types of elements are available in 1D, 2D, and 3D. Sometimes the term “mesh element” means any of the mesh elements—mesh faces, mesh edges, or mesh vertices. In particular, mesh elements of a particular domain in the geometry (a subdomain, boundary, edge, or vertex) have its dimensionality: a *d*-dimensional domain is discretized with *d*-dimensional mesh elements (Fig. 3).

Once performed this first problem partitioning task, it is possible to introduce approximations to the dependent variables. An example is clarifying. Let us consider the case of a single variable.

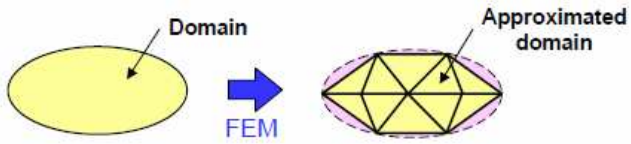

Fig. 3 Geometry approximation by meshing

If we analyze it, from a basic point of view, the FEM solves equations in the matrix form, as synthesized in Fig. 4, where the analogy is reported with the mechanics terminology, form which it inherited the approach. Written in a very simple and intuitive form, what the solver

has to obtain at the end of all the geometrical problem discretizing and linearization , is the solution of a matrix equation in the form reported in Fig. 4., where ***u*** is the vector of the unknown values assumed by the dependent variable on the nodes of the discretized geometry. Attention must be paid to avoid situations like the one reported in Fig. 5 where there is a so called ill conditioning of the problem, since (keeping the analogy with elastic constants and mechanics) the two elastic constants (in general the elements of the stiffness matrix ***K***) are extremely different in amplitude, thus posing computational problems.

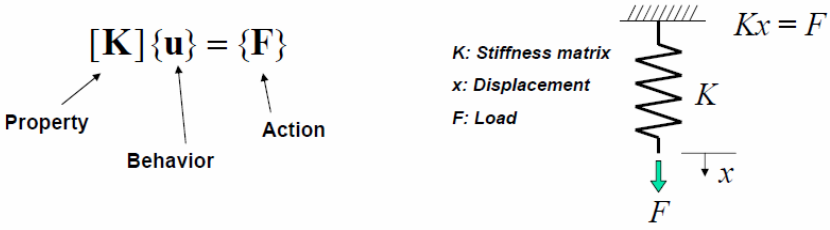

Fig. 4 The philosophy and also terminology of FEM borrowed from the mechanics

In particular, the general idea is to approximate *u* with a function that it is possible to describe with a finite number of parameters, the so-called *degrees of freedom* (DOF). Inserting this approximation into the weak form (that we will later briefly discuss) of the equation generates a system of equations for the degrees of freedom.

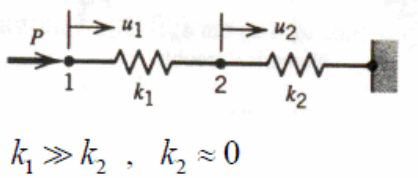

Fig. 5 Simple example of an ill conditioned problem

This simple example can help immediate understanding: linear

elements in 1D. Let us assume that a mesh consists of just two mesh intervals: $0 < x < 1$ and $1 < x < 2$. Linear elements means that on each mesh interval the continuous function u is linear (affine). Thus, the only thing there is need to know in order to characterize u uniquely is its values at the *node points* $x_1 = 0$, $x_2 = 1$, and $x_3 = 2$. Denote these as $U_1 = u(0)$, $U_2 = u(1)$, $U_3 = u(2)$. These are the *degrees of freedom*.
Now it is possible to write:

$$u(x) = U_1\varphi_1(x) + U_2\varphi_2(x) + U_3\varphi_3(x) \qquad (1)$$

where $\varphi_i(x)$ are certain piecewise linear functions. Namely, $\varphi_i(x)$ is the function that is linear on each mesh interval, equals 1 at the i^{th} node point, and equals 0 at the other node points. For example,

$$\varphi_1(x) = \begin{cases} 1-x & \text{if } 0 \le x1 \le 1 \\ 0 & \text{if } 1 \le x1 \le 2 \end{cases} \qquad (2)$$

The $\varphi_i(x)$ are called the *basis functions*. The set of functions $u(x)$ is a linear function space called the *finite element space*.
For better accuracy, it is possible to consider other finite element spaces corresponding to quadratic, cubic, etc. elements. Functions u in this space are 2^{nd}, 3^{rd}, etc. polynomials on each mesh interval.
Moreover, in general, a finite element space is specified by giving a set of basis functions.

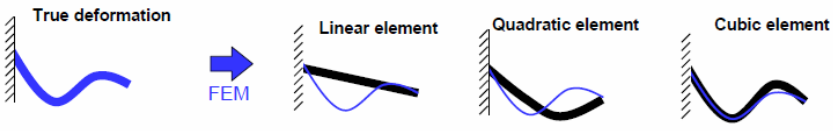

Fig. 6 An example showing the degree of approximation due to different orders of the elements

The description of the basis functions is, furtherly, simplified by the introduction of *local coordinates* (or *element coordinates*). Let us consider a d-dimensional mesh element in an n-dimensional geometry (whose space coordinates are denoted by $x_1,..., x_n$) and the *standard d-*

dimensional simplex:

$$\xi_1 \geq 0, \xi_2 \geq 0, ..., \xi_d \geq 0, \xi_1 + \xi_2 + ... \xi_d \leq 1 \qquad (3)$$

which resides in the local coordinate space parametrized by the local coordinates ξ_1, …, ξ_d. If d = 1, then this simplex is the unit interval. If d = 2, it is a triangle with two 45 degree angles, and if d = 3 it is a tetrahedron.

If we consider the mesh element as a linear transformation of the standard simplex, namely, by letting the global space coordinates x_i be suitable linear (affine) functions of the local coordinates, it is possible to get the mesh element as the image of the standard simplex; when described in terms of local coordinates, the basis functions assume one of a few basic shapes. These are the *shape functions*.

Moreover, when using higher-order elements (that is, elements of an order > 1), the solution has a smaller error. The error also depends on how well the mesh approximates the true boundary. To keep errors in the finite element approximation and the boundary approximation at the same level, it is wise to use *curved mesh elements*. They are distorted mesh elements that can approximate a boundary better than ordinary straight elements (if the boundary of the problem is curved). It is possible to get curved mesh elements by writing the global coordinates x_i as polynomials of order k (the *geometry shape order*) in the local coordinates ξ_j For mesh elements that do not touch the boundary, there is no reason to make them curved, so they are straight.

The order k is determined by choosing the *geometry shape order* for the coordinate system associated with the finite element.

Nevertheless, if a curved mesh element becomes too distorted, it can become inverted and cause problems in the solution. This is exactly what happens in one of the models described in the following sections. More details for the solution adopted for this inconvenient are indeed reported in § 3.3.2.2

In this brief overview, it must be pointed out that our choice for all the modeled structures has fallen on the *Lagrange* element type (piecewise polynomials of degree k). They are indeed widely used since they are available with all types of mesh elements.

In these quick notes on FEM, it is certainly important to

mention the choice of the type of analysis (linear, non linear, time dependent non linear, etc.) strongly depending on the physical and mathematical features inherent the reality to model.

In general, the solvers break down each problem—whether linear or nonlinear—into one or several linear systems of equations by approximating the given problem with a linearized problem. The coefficient matrix of the discretized linearized problem is called the *Jacobian matrix* (or *stiffness matrix*), just the one cited in the introductory part of this paragraph. Moreover, since in this work we have used for all our models the time-dependent solver, it is necessary to highlight that it must be chosen (it is indeed the one we have used for all our investigations) to find the solution to linear or nonlinear *time-dependent PDE problems*, also known as *dynamic problems* or *unsteady problems*.

Indeed, the general formulation of a time-dependent PDE (defined on computational domains in 1D, 2D, or 3D) in coefficient form is:

$$e_a \frac{\partial^2 u}{\partial t^2} + d_a \frac{\partial u}{\partial t} + \nabla \cdot (-c\nabla u - \alpha u + \gamma) + \beta \cdot \nabla u + au = f \qquad (4)$$

where:
• e_a is called mass coefficient
• e_a is said to be damping coefficient, or mass coefficient.
• c is the diffusion coefficient.
• α is the conservative flux convection coefficient.
• β is called the convection coefficient.
• a is the absorption coefficient.
• γ is the conservative flux source term.
• f is the source term.

This PDE formulation together with boundary and initial conditions fully define the problem.

The time-dependent solver operates a discretization of the problem, leading to a differential-algebraic system (DAE) or to ordinary differential equations (ODE), solved by appropriately chosen algorithm. Thus the solver is an implicit time-stepping scheme, which implies that it must solve a possibly nonlinear system of equations at each time step. It solves the nonlinear system using a Newton

iteration, and it then solves the resulting systems with an arbitrary linear system solver.

Furthermore, it is sometimes essential for accuracy or performance to set absolute and relative tolerance parameters for the time-dependent solver. They are tolerances to control the error in each integration step. More specifically, let U be the solution vector corresponding to the solution at a certain time step, and let E be the solver estimate of the (local) error in U committed during this time step. The step is accepted if

$$\sqrt{\frac{\sum_{i=1}^{N}\left(\frac{E_i}{A_i+R|U_i|}\right)^2}{N}} < 1 \qquad (5)$$

where A_i is the absolute tolerance for DOF i, R is the relative tolerance, and N is the number of degrees of freedom. The accumulated (global) error can be larger than the sum of the local errors for all the integration steps. However, the solver's error estimate is often too pessimistic, which means that the estimated local error typically is of the same order of magnitude as the true global error.

To conclude our brief digression on FEM, it is very useful to point out, as in some cases it has been used in modelling the neural cell structures that we will describe in the following sections, that there is an alternative formulation of the problem, different from the one defined in (4): it is the so-called *weak formulation.*
Indeed, eq. (4) is a *strong definition*, while the problem can be also solved working on the integral formulation (the weak one) of the PDE, using test functions. In the practice, they are adopted to multiply both members of eq. (4) and then integrate over the domain of interest to solve the problem in its integral definition. Thus, unlike the other formulation, the weak form takes on the character of generality, allowing greater flexibility in setting the conditions: it is possible to assign constraints on subdomains, boundaries , edges and points. Moreover, it is always possible to translate a strong formulation into the weak one, if the used test function is a well-behaved function,

while the converse is not always true. Moreover in the *boundary weak form*, it is possible to solve for variables defined only on boundaries and couple this equation with other equations defined on a subdomain.

This technique is particularly useful in modelling adsorption processes (where it is necessary for balances on the edges to “agree” with those in adjacent domains) for a smart-handling of extremely thin layers. This will be clearly demonstrated in the next sections by the reduction in computational burden attained exploiting the well known technique of the thin layers approximation and validating the obtained results with a non-approximated model.

To summarize: modelling with FEM requires a preprocessing, the solving phase and the analysis of the results, proceeding following the reported steps:

1) Selection of the analysis type (transient dynamic analysis with time dependent solver is the one we use in this thesis work);

2) Selection of the element dimensionality and type, depending on the problem to solve and on the geometry analyzed (2-D, 3-D) leading to linear, quadratic, etc. elements;

3) Choice of the primary material properties to model;

4) Choice of nodes positioning;

5) Construction of the elements by assigning connectivity between the nodes (these last two are typically implemented automatically by an algorithm, in our case the Delaunay one);

6) Application of the boundary conditions and “input stresses”;

7) Processing: solution of the (eventually time-varying) boundary value problem;

8) Postprocessing: evaluation and analysis of the results.

3.2 Hodgkin-Huxley lumped circuit set of differential equations translated into field ones (2D case).

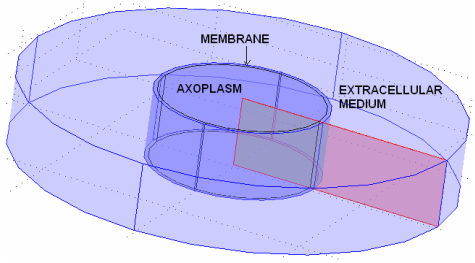

Fig. 7 The axon slice under analysis (3D sketch). The section in r-z plane is highlighted in pink

Here a description is performed of the FEM model For a nanoelectrode-axon segment stimulation system.

A 2D FEM model of the stimulating equipment and of the axon segment is implemented that simulates the most relevant dynamics of spatiotemporal transmembrane voltage (TMV) [50].

Bases on Hodgkin and Huxley (HH) set of highly non linear differential equations (linking the phenomena of chemical transport through the membrane with the electrical dynamics of the neuron), a translation is performed in terms of electromagnetic parameters in three dimensions. Coupling this model with the quasi-static formulation of Maxwell equations the elicitation and propagation of APs is obtained by exploiting the high nonlinearity of the medium membrane. Indeed, the nonlinearity of the membrane is not modelled as classically in literature by using the so-called "cable equation" which has the disadvantage of having to estimate in advance the speed of propagation of the AP along the axon, but is implemented "implicitly", using the definition itself of the equivalent conductivity which is gained by the translation itself of Hodgkin-Huxley equations suitable for a field solution.

The adopted modelling approach has been modular and incremental since, in order to have a first comparison with literature data, before starting with a three dimensional modelling activity, a 2D

accurate model has been realized, for a section of tubular segment of a nervous cell axon (the neuronal structure carrying nervous signals) which takes into account, through the so called Hodgkin-Huxley (HH) equations , the non linear and time varying behaviour of the membrane that surrounds it. The lumped-circuit quantities of the HH electrophysiological model are transformed into parameters adapt to a *field solution* study. In fact, the Electro Quasi Static (EQS) formulation of the Maxwell equations describing the relevant phenomena is faced by using the Finite Element Method (FEM). The non linear differential equations describing the membrane behaviour are efficiently and accurately combined with the FEM solution in a numerical procedure performed by using COMSOL Multiphysics®. The proposed procedure is then employed to evaluate the space and time dynamics of the Action Potential (AP) along the axon segment. Due to its simple implementation the proposed model can be easily used to simulate the behaviour of more complex nervous structures. The simulation procedure encompasses three phases: the first, in which the resting (static) solution is calculated, thus ensuring that the correct starting point for dynamic simulations is obtained, the second one, exploited to simulate *non-propagated APs* and the third one to reproduce their propagation along the segment under examination.
The *extrusion* feature of COMSOL Multiphysics proves to be a very helpful tool in projecting variables (voltages) from cell membrane boundaries onto the domain itself, where the calculation of its voltage-dependent electric conductivity needs to be performed.
In addition, the very small dimension of the membrane thickness compared to the other geometrical dimensions of the system is approximated, in an alternative version of the model, as a thin layer thus leading to a sensible reduction of the computation burden. A comparison between the two model versions has led to very satisfactory results, as far as APs elicitation and propagation are concerned.

3.2.1 The extrusion tool in FEM modelling

In FE modeling an *extrusion coupling variable* maps values from a source domain to a destination domain. When the domains are of the same space dimension, and it is typically a point-wise mapping. When

the destination domain has higher dimension than the source one, the mapping is done by extruding point-wise values to the higher dimensions. It is possible to define the transformation between the source and destination in two ways: as a *linear* or a *general transformation*.

The linear transformation maps between domains of the same dimension. The domains can exist in geometries of different space dimensions. For example, it is possible to couple from edges in 2D to those in 3D or 2D subdomains to 3D faces. In these cases obviously there is need of geometries of different space dimensions for the source and destination. The linear transformation is defined by specifying points in both the source and destination.

As far as the *general transformation* is concerned, instead, the extrusion coupling variable defines a more general transformation between source and destination than the linear one. Specifically, when the destination domain has more space dimensions than the source domain, the variable performs extrusion of values.

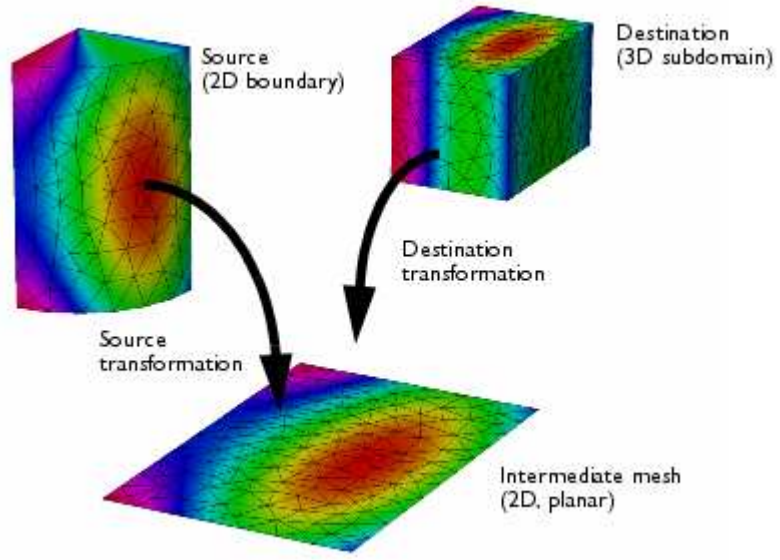

Fig. 8 Example of a general transformation mapping from a 2D to a 3D domain [51]

The definition of any extrusion coupling variable involves two mesh transformations, which are important to understand. The *source*

transformation is a one-to-one mapping that maps the mesh of the physical source domain to an *intermediate mesh* embedded in a space of the same dimension as the source. The *destination transformation* is a mapping from the destination domain, where the value of the variable is defined, to the same space that contains the intermediate mesh.When the value is requested of the coupling variable somewhere in the destination domain, the transformation of the destination points is realized, using the destination transformation. It compares the resulting coordinates to the elements in the intermediate mesh to find corresponding locations in the physical source domain. This means that the source transformation must be inverted but not the destination transformation. The latter can in fact be noninvertible, which is, for example, the case for a linear extrusion.

To avoid the need to solve a nonlinear system of equations for every destination point, the software solver assumes that the source transformation is linear on each element of the intermediate mesh. In practice, the transformation is often trivial and leaves the coordinates unchanged, but it can also rescale, stretch, bend, or reflect the mesh. It is important to notice that the definition must be performed of the source transformation that maps the source domain to the intermediate domain of the same dimension. *The source transformation has the same number of fields as the dimension of the source domain*. Expressions can be used containing space coordinates in the source geometry when defining the transformation. It is moreover necessary to highlight that the transformation must be approximately linear within each mesh element. When defining the transformation it is, also, permissible to use expressions containing space coordinates in the destination geometry and specifying an arbitrary transformation, which can be highly nonlinear or noninvertible.

To summarize the *general* case, we can say that if source and destination transformation are defined according to Table 1, the FEM solver operates a back substitution starting from the destination domain $\mathcal{D}$.

Table 1 Extrusion general transformation in the most general form: when the source domain is 3D

Source Transformation	Destination Transformation
$\begin{cases} X_{src} = S_x(x,y,z) \\ Y_{src} = S_y(x,y,z) \\ Z_{src} = S_z(x,y,z) \end{cases}$	$\begin{cases} X_{dest} = D_x(x,y,z) \\ Y_{dest} = D_y(x,y,z) \\ Z_{dest} = S_z(x,y,z) \end{cases}$

Here the final goal, in extruding the assigned variable *Var* from the source domain $\boldsymbol{S}$ to $\boldsymbol{\mathcal{D}}$, is to calculate its value in every point $P_i(x_i,y_i,z_i)$, belonging to the destination domain mesh. In order to do so, it is necessary for the solver to determine, once given P_i which are the coordinates (x_j,y_j,z_j) of the corresponding point $P_j(x_j,y_j,z_j)$ in $\boldsymbol{S}$, where $Var(P_i)=Var(P_j)$. In particular, going through the following series of passages for every assigned point $P_i(x_i,y_i,z_i)$, the solver firstly determines X_{dest}, Y_{dest} and Z_{dest} (this way destination transformation can be also non invertible) (6) and then matches them with the values of X_{src} , Y_{src} and Z_{src} respectively (7).

$$\begin{cases} X_{dest} = D_x(x,y,z)\big|_{P_i} = X^* \\ Y_{dest} = D_y(x,y,z)\big|_{P_i} = Y^* \\ Z_{dest} = D_z(x,y,z)\big|_{P_i} = Z^* \end{cases} \tag{6}$$

$$\begin{cases} X_{src} = X_{dest} \\ Y_{src} = Y_{dest} \\ Z_{src} = Z_{dest} \end{cases} \tag{7}$$

Now, since source transformation must be invertible the coordinates can be finally determined of the point $P_j(x_j,y_j,z_j)$ as in (8), obviously including as third equation (there are three d.o.f.) the geometrical constraint assuring Pj to belongs to the its particular subdomain

$$\begin{cases} S_x(x_j, y_j, z_j) = X^* \\ S_y(x_j, y_j, z_j) = Y^* \rightarrow (x_j, y_j, z_j) \\ S_z(x_j, y_j, z_j) = Z^* \end{cases} \quad (8)$$

3.2.2 Membrane nonlinearity exploitation for propagative effect simulation.

The schematic structure of an axon segment of nerve cell surrounded by its membrane (or axolemma) is pictured in Fig. 7. Due to its axial symmetry, it is possible to consider only the highlighted section by modelling it in a cylindrical coordinate system as it will be shown in Fig. 9(a) and (b).The 2D axial symmetric transient analysis packet of the Quasi-Static Electric AC/DC module, the time dependent analysis of the PDE mode packet in general (version A) and weak form (version B), the extrusion tool and the possibility to perform a thin layer approximation given by COMSOL Multiphysics are exploited, in order to evaluate the behaviour of the considered structure [52]. .In particular, we model a section of 0.5μm×1.505μm (0.5μm×0.5μm for the axon domain, D_a, 0.5μm×5nm for the membrane domain, D_m, and 0.5μm×1μm for the external medium represented by D_e).

The small size of the system with respect to the characteristic wavelength of the electromagnetic field and the low contribution of the energy associated to the magnetic field compared to that stored in the electric field allow the adoption of the EQS approximation of Maxwell equations. Sub-domains D_a and D_e are considered as linear, homogeneous and isotropic dielectric materials, described by their constant electric conductivity σ_a and σ_e and dielectric permeability ε_a and ε_e respectively The corresponding values are reported in Table 1. On D_m, besides a linear permittivity ε_m and a non linear equivalent conductivity σ_m defined by (11), an external current density depending on the voltage across the membrane is imposed in order to approximate the nonlinear behaviour of the medium with respect to the imposed electric field (according to the HH model of the membrane). In particular, HH circuit-equations must be “converted” to obtain their *field equivalent*.

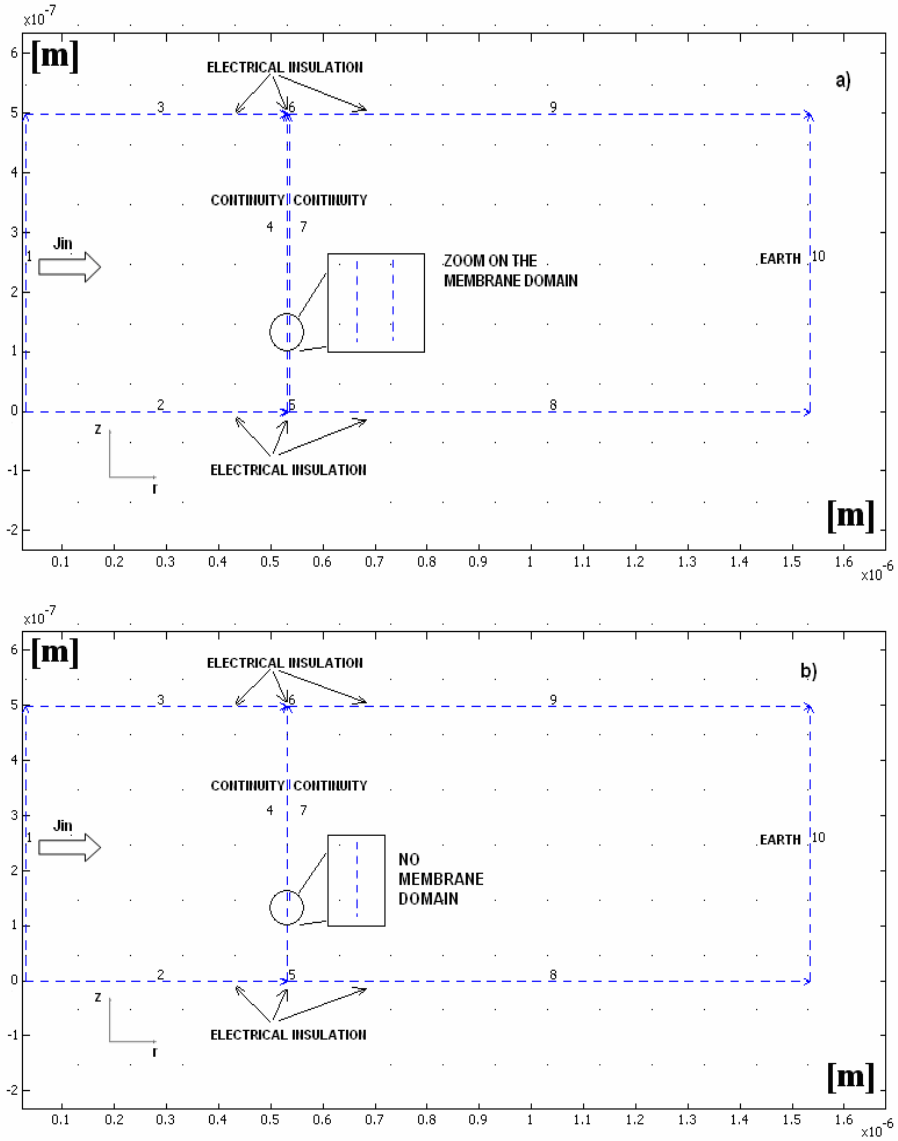

Fig. 9 (a) Axisymmetric 2D section in r-z plane, with boundary conditions chosen: model version A, (b) model version B

First of all, since membrane thickness is very small, to a first approximation it can be looked at as a parallel plate capacitor, when determining its dielectric and equivalent conductivity from values found in literature.Thus, once defined all constants as in Table 2, the dielectric constant per unit area is:

$$\varepsilon_m = \frac{C_m d_m}{\varepsilon_0} \tag{9}$$

whereas membrane equivalent conductivity σ_m can be derived by HH overall membrane conductance, G_m, defined as a function of the Sodium, Potassium and Leakage conductances, depending on Transmembrane Voltage (TMV) through the so called channel activation variables. Then, once defined Gm as in (10), σ_m becomes (11):

$$G_m = G_{Na} + G_K + G_l \tag{10}$$

$$\sigma_m = G_m \cdot d_m \tag{11}$$

The expressions of ionic channel conductances, reported in (12) and in (13) show their connection with the activation variables *m*, *n* and *h*, implicitly defined by the differential equations set (14) [53]:

$$G_{Na} = G_{Na\,max} m^3 h \tag{12}$$

$$G_K = G_{K\,max} n^4 \tag{13}$$

$$\frac{dx}{dt} = \alpha_x (1-x) - x\beta_x \quad \text{with } x \in \{m,n,h\} \tag{14}$$

The transfer rate coefficients, β_m, α_n, β_n, α_h, β_h in (14), are not constant numbers but, as shown in Table 3, depend on the value of the voltage across the axon membrane $V_m(x,y,z,t)$.

Table 2 Parameters appearing in the model.

Parameter	Value	Description
V_{sta}	*-60*[mV]	Static TMV, at which membrane is polarized in the simulation
ε_m	*5.65*	Membrane relative dielectric constant
C_m	*1*[μF/cm^2]	Membrane capacitance per unit area
d_m	*5*[nm]	Membrane thickness
G_{Namax}	*120*[mS/cm^2]	Conductance per unit area of the Na channel
G_{Kmax}	*36*[mS/cm^2]	Conductance per unit area of the K channel
G_l	*0.3*[mS/cm^2]	Conductance per unit area of the leakage channels
E_{Na}	*55* [mV]	Nernst voltage due the Na concentration
E_K	*-72* [mV]	Nernst voltage due the K concentration
E_l	*-49.387*[mV]	Nernst voltage due other ionic concentrations
a_{nsta}	*58.197*	Initial value[1/s]
b_{nsta}	*125*	Initial value [1/s]
a_{msta}	*223.563*	Initial value [1/s]
b_{msta}	*4000*	Initial value [1/s]
a_{hsta}	*70*	Initial value [1/s]
b_{hsta}	*47.425*	Initial value [1/s]
σ_{Ax}	*0.5*	Axoplasm conductivity
ε_{Ax}	*80*	Axoplasm diel. constant
σ_{Ext}	*1*	Ext. Med. conductivity.
ε_{Ext}	*80*	Ext. Med. diel..constant

Table 3 Expressions of the transfer rate coefficients. $V'=V_m-V_{sta}$ represents the TMV deviation from the resting value [mV].

$\alpha_n = 1000\frac{0.1-0.01V'}{e^{(1-0.1V')}-1}$	$\beta_n = 1000\frac{0.125}{e^{0.0125V'}}$
$\alpha_m = 1000\frac{2.5-0.1V'}{e^{(2.5-0.1V')}-1}$	$\beta_m = 1000\frac{4}{e^{(V'/18)}}$
$\alpha_h = 1000\frac{0.07}{e^{0.05V'}}$	$\beta_h = 1000\frac{1}{e^{(3-0.1V')}+1}$

The HH trans-membrane current density equation for a unit area patch of membrane can be expressed as:

$$I_m = C_m \frac{dV_m}{dt} + G_m V_m - J_e \tag{15}$$

with

$$J_e = G_{Na} E_{Na} + G_k E_k + G_l E_l \tag{16}$$

Furthermore, the equation of continuity implemented everywhere over the FEM model can be written as (17)

$$\nabla \cdot \frac{\partial(\varepsilon_i \nabla V)}{\partial t} + \nabla \cdot \left(\sigma_i \nabla V - \bar{\boldsymbol{J}}_{\boldsymbol{ext}}\right) = 0 \tag{17}$$

where

$$\bar{\boldsymbol{J}}_{\boldsymbol{ext}} = \begin{cases} J_e \hat{\boldsymbol{r}} & \text{on } \mathrm{D_m} \\ 0 & \text{on } \mathrm{D_a} \cup \mathrm{D_e} \end{cases} \tag{18}$$

The continuity equation (17) must be implemented on the whole model, whereas the HH equations system must be associated only to the membrane domain. As the three voltage-controlled conductances G_{Na}, G_K and G_l are meaningful *only on membrane domain* and not externally, they require to be *only locally* defined. The flexibility of COMSOL Multiphysics proves useful in handling variables, as well as in the post-processing phase. In the simulation session a *PDE packet in general form* is coupled to the Electrostatic module: the first one is employed in order to solve equation (17) with respect to the so-called dependent variable (in this case *electric potential*, *V*), whereas the second one is introduced to solve the three differential equations in *m, n, h (dependent variables)*, representing channel activation variables according to the HH model [49], as shown in equations (14) and Table 2. In order to obtain the voltage values along both sides of membrane, point by point along the z coordinate, the “extrusion” feature of COMSOL Multiphysics is conveniently employed. In fact the

equations implemented there, explicitly depend on transmembrane voltage $V_m(z, t)$:

$$V_m(z,t) = V_i(z,t) - V_o(z,t) \tag{19}$$

where V_i and V_o are the voltage along the boundaries 4 and 6 (as depicted in Fig. 9(a)), respectively extruded from those two 1D domain with the extrusion transformation reported in Table 4:

Table 4 Extrusion transformation from 1D boundaries 4 and 6 of Fig. 9 to 2D membrane domain.

Source Transformation	Destination Transformation
$X_{src} = S_x(x,y,z) = z$	$X_{dest} = D_x(x,y,z) = z$

In this way a sort of translation of the HH lumped-circuit quantities into parameters adapt to a field solution study, as previously highlighted, is achieved It must also be noticed that while ε_m obtained is a constant, σ_m depends on transmembrane voltage V_m *(z,t).*The simulation is carried out, fixing all initial conditions from nominal resting values. The iterative procedure is stopped when the numerical variations are *sufficiently* negligible leading to the "equilibrium" steady state conditions. This condition is adopted as a starting point for studying the membrane dynamical behaviour in the second step of the procedure in which the cellular responses elicitation are evaluated. Square window current density stimuli of different amplitude and duration have been applied to boundary 1 (Fig. 9) and the relative results will be shown in § 3.2.4.

3.2.3 Thin layer approximation

In finite element modelling (here in particular), in order to simplify meshing and to greatly reduce simulation time and memory request, it is preferable to avoid extremely thin structures as membrane subdomain could be, especially in the perspective of a generalization of this model to a more complex situation (taking into account soma, axon hillock, axon initial segment). For example, if it were necessary to simulate a motor neuron behaviour, this would result in a form

factor (length of the axon divided by membrane thickness) that could also, at worst, be of the order of 10^9. It is clear that the idea of completely avoiding membrane physical realization, using *thin layer approximation* [51]as an alternative to the model described in the previous section, appears very attractive. This is the reason why a new model (Fig. 9) has been implemented that exploits this approximation technique, whose hypotheses of applicability are completely satisfied in the case under examination:

1) there is a substantial difference between membrane domain conductivity and those of the other two domains;
2) lateral boundaries are insulated (null net flux);
3) current density components along φ and z are negligible with respect to that along r-axis.

In particular, since membrane is very thin, it is possible to approximate the potential distribution along its thickness as being linearly varying from V_o to V_i, so, using the continuity equation for the current, it is easy to derive, as explained in [51], the expression for an equivalent current density J_{eq} , where J_e is defined in (16):

$$J_{eq} = \sigma_m \frac{(V_2 - V_1)}{d_m} + J_e + \frac{\varepsilon_m \varepsilon_0}{d_m} \frac{\partial (V_2 - V_1)}{\partial t} \tag{20}$$

where V_1 and V_2 represent the voltage values along the membrane boundaries 4 and 7, respectively. This equation can be implemented by using two different Electrostatic systems of equations in order to allow the solver to "see" interface surface, which now substitutes membrane domain, once as belonging to axoplasm domain, once to external medium domain. It is clearly expectable that voltage on that boundary will have a discontinuity (V_2-V_1) almost equal to the value that transmembrane voltage would have reached, if the membrane were really implemented in the model as a 2D domain. Thus, V_1 is set as an *active* variable only in the axoplasm domain, V_2 only on the external medium domain, while both are defined on their interface. J_{eq} is imposed as an input current density to this boundary. In addition, an alternative formulation of the three non linear differential equation must be provided on this surface where all expressions are locally defined. The idea is to use a *weak form for boundary* approach, instead of the *PDE formulation in general form*, as that adopted in

version A. This choice allows to handle all the equations in the integral form, multiplying both sides of each equation by a test function and then integrating.

3.2.4 Comparison between the two 2D models

In order to make a fair comparison between the two modelling solutions, some common parameters as those reported in Table 5 are adopted. The same initial and boundary conditions are fixed everywhere, exception made for the various settings related to membrane domain since it is not present in the second model. This settings induce the meshes pictured in Fig. 10. Even before introducing any current density source to elicit membrane response, a clear improvement can be observed when adopting the weak solution B, instead of A, since the Delaunay algorithm does not lead to crowd the great amount of triangles next to the thin membrane domain, as Fig. 10 demonstrates.

The savings in terms of simulation time and amount of memory consumed are summarised inTable 6 to simulate a stationary equilibrium state.

Table 5 Parameters used for comparing the two models

Calculus and mesh parameters	Value
Simulation times	$0{:}10^{-4}{:}20$ms
Relative tolerance	10^{-4}
Absolute tolerance	10^{-8}
Max. elem. size scaling factor	1
Element growth rate	1.3
Mesh curvature factor	0.3
Mesh curvature cut off	0.001

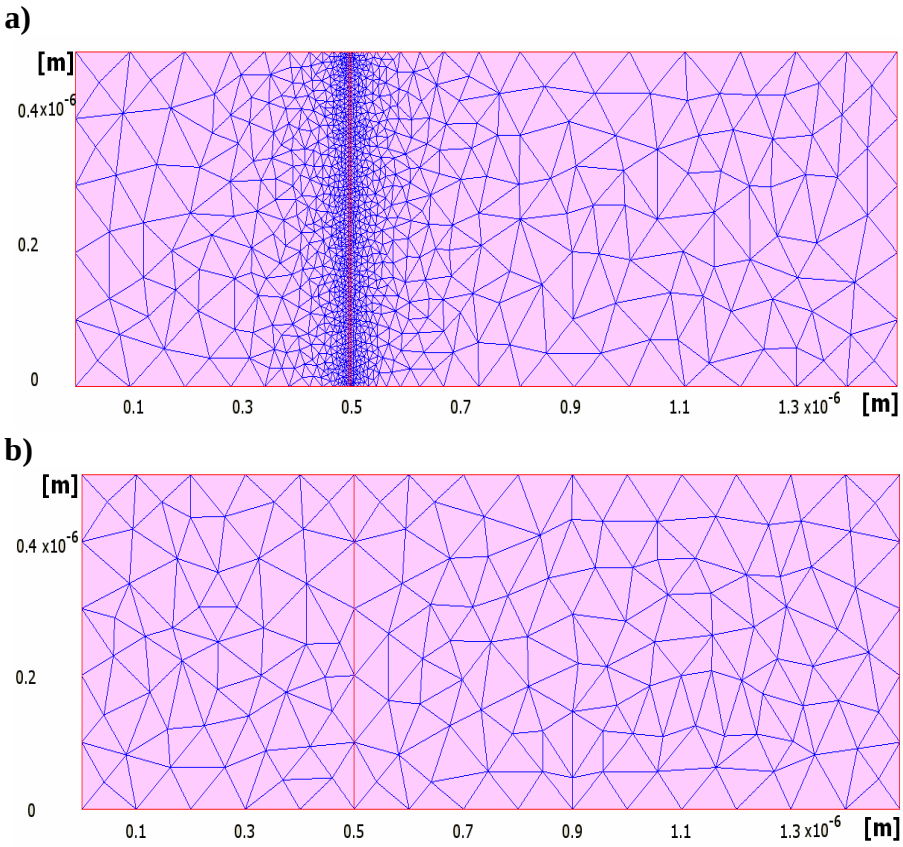

Fig. 10 Mesh in the model a) with membrane and b) without membrane using thin layer approximation

Table 6 Figures of merit concerning the two models

PARAMETER / MODEL	**A**	**B**
Degrees of freedom	7086	685
N. of boundary sides	220	45
N. of elements	2378	300
Minimum quality level	0.5867	0.5666
Simulation duration	13.000 s	2.630 s

In Table 7, instead, the case of 20ms of membrane behaviour simulation is reported when it undergoes a stimulus-induced response.

In this case an appropriate current density (J_{in}, the square window shown in the inset of Fig. 9 is applied at $r=r_1=1$nm, very close to the symmetry axis, in order to trigger the excitable membrane (if current density stimulus where injected exactly at r=0μm, current density would have been undefined).

Table 7. Simulation times in [s]. Stimulus duration: short (d), long (D). Stimulus amplitude: low (a), high (A)

	d/a	d/A	D/a	D/A
Model A	83.64	185.594	119.313	183.719
Model B	19.797	48.968	26.891	42.704

A great advantage is offered by Model B in the dynamic case too, as far as stimulation length is concerned (Table 7). It is interesting to observe how membrane responses, in the four corresponding cases (Fig. 11) almost coincide in the two modelling approaches and are in accordance with theoretical expectations [54]. In the first case (*da*), the stimulus is not sufficient to elicit any AP (sub-threshold behaviour, whose parameters, rise time and amplitude, are those expected) showing a passive electrotonic nature of the membrane, being it approachable (at least in first approximation) as an R-C circuit.

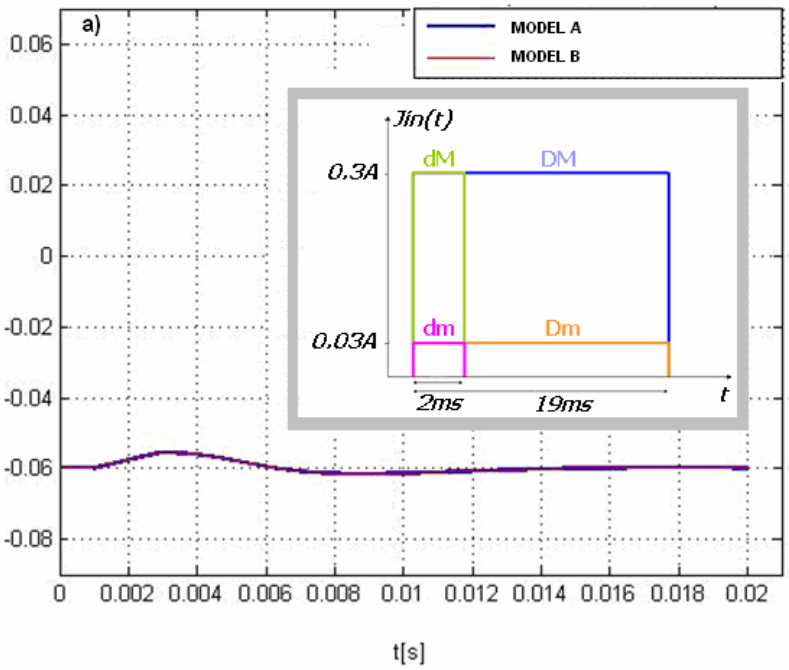
a)
MODEL A
MODEL B
Jin(t)
0.3A
dM
DM
0.03A
dm
Dm
2ms
19ms
t
0.06
0.04
0.02
0
-0.02
-0.04
-0.06
-0.08
0 0.002 0.004 0.006 0.008 0.01 0.012 0.014 0.016 0.018 0.02
t[s]

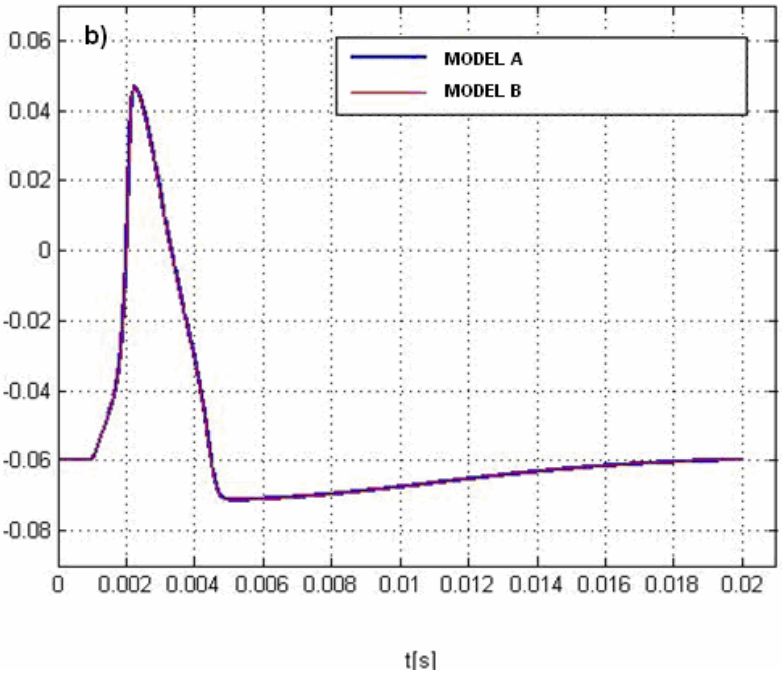
b)
MODEL A
MODEL B
0.06
0.04
0.02
0
-0.02
-0.04
-0.06
-0.08
0 0.002 0.004 0.006 0.008 0.01 0.012 0.014 0.016 0.018 0.02
t[s]

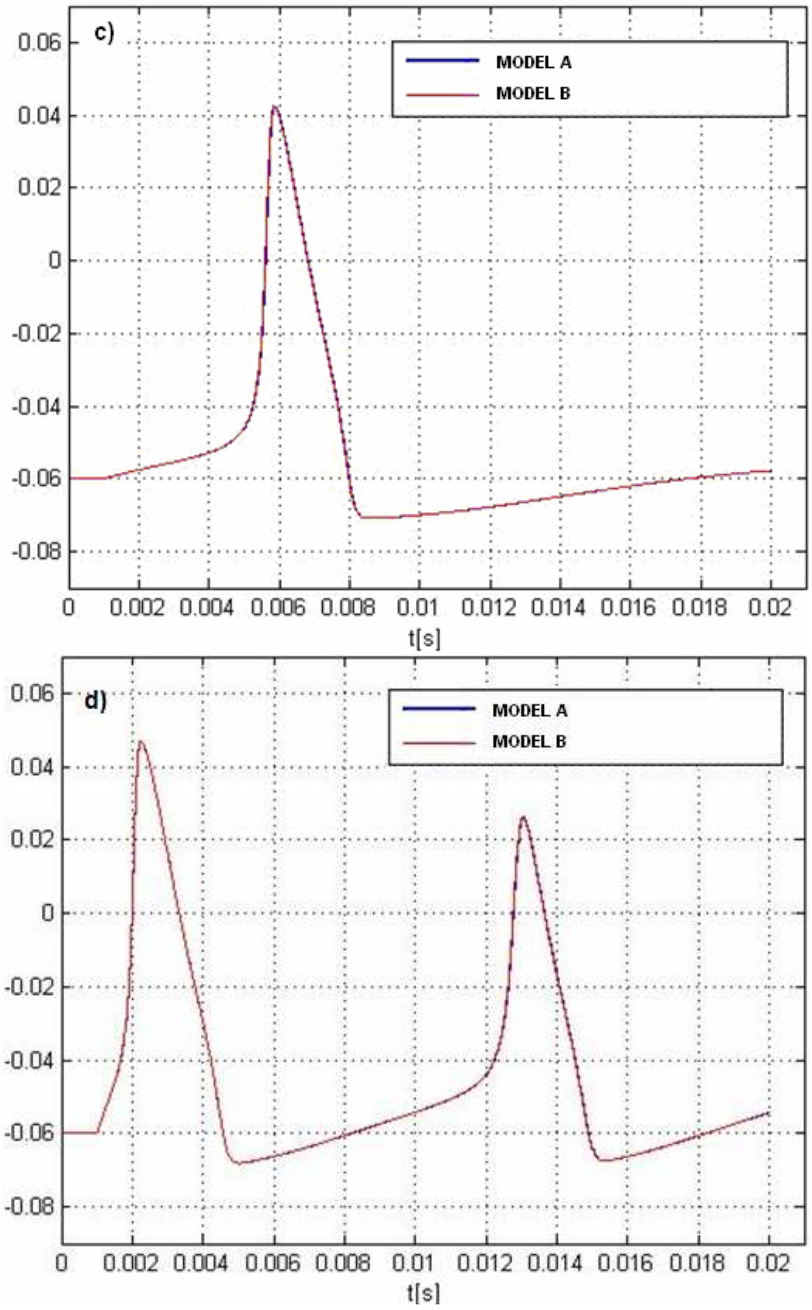

Fig. 11 (a),(b),(c),(d) Membrane response (T= 6.3°C) in cases *da, dA ,Da, DA,* respectively. Inset in (a): input stimulus parameters

In the second and in the third one, an AP is observed, while in the fourth one, since both strength and duration of the stimulus pulse are high, two APs are excited, the second of which is lower than the other, because refractory period is not respected.

Moreover, this simulations are carried out supposing an operation temperature of 6.3°C. Adding also temperature dependence to the model, it has been possible to obtain the results shown in Fig. 14. This picture shows how, as theoretically expected [55],[56] , the spiking of the neuron is affected by a change in the temperature parameter (here a step of 3°C separates the five reported cases). Moreover, it can be observed, in Fig. 14a) and particularly in Fig. 14b) (zooming on the first AP) that the maximum value assumed by the $V_m(t)$ gets lower and lower increasing the value of the ambient temperature, while the duration of the spikes gets minor in contrast with the number of them (three spikes for the case at T=9°C and seven for T=21°C). In particular, as a particular case exemplification in Fig. 14c) we have chosen to show when the temperature assumes a particular value of 18.5°C As theoretically expected, when the temperature assumes this value the membrane response results in a sequence of six APs, shorter than the two observed at lower temperature (Fig. 11). Indeed, channel time constants are all scaled by the factor $3^{(0.1T-0.63)}$, see [56], since the new differential equations become:

$$\frac{dx}{dt} = [\alpha_x(1-x) - \beta_x x] \cdot 3^{\frac{T-6.3}{10}} \tag{21}$$

with $x \in \{m,n,h\}$. This yields to:

$$\frac{dx}{dt} = [\alpha'_x(1-x) - \beta'_x x] \tag{22}$$

where α'_x and β'_x correspond to the old values times the factor just introduced, modifying the τ_x of the "channel-gating" processes as:

$$\tau'_x = \frac{1}{\alpha'_x + \beta'_x} = \frac{\tau_x}{3^{\frac{T-6.3}{10}}} \tag{23}$$

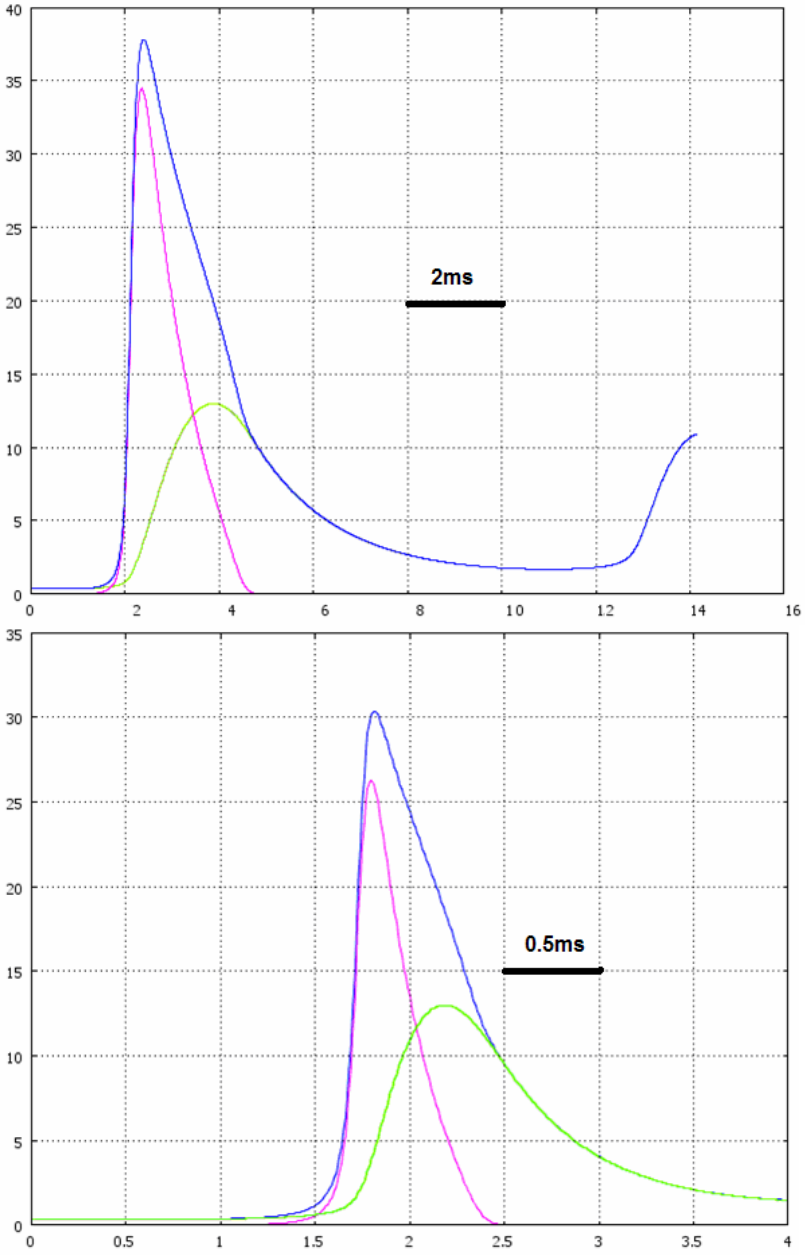

Fig. 12 Temporal shape of the GN_a (magenta), GK(green), G (blue), total membrane conductance in [mS/cm^2] vs [ms] , for Upper: T=18.5°C (also an initial phase of the second triggering is observed at the end depending on the stimulus time duration). Lower T=6.3°C

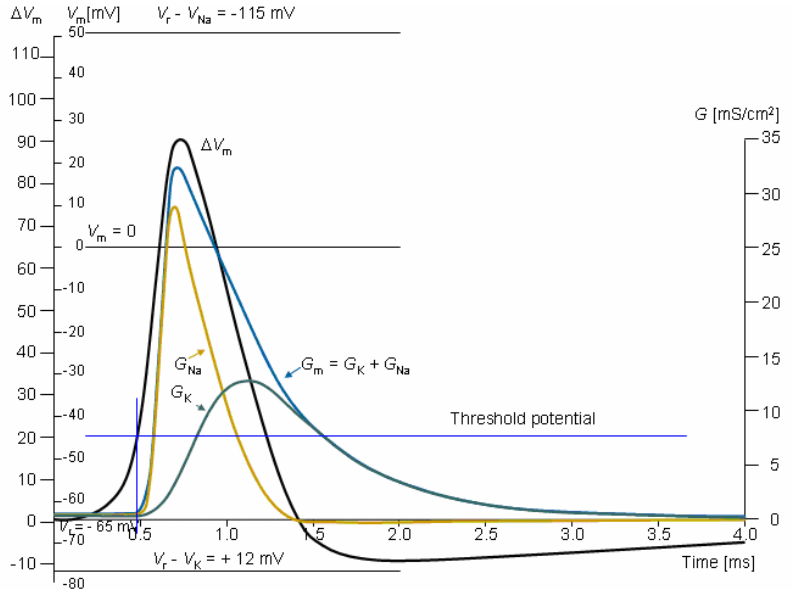

Fig. 13 [56] T=18.5°C

This results in a reduced time constant τ'_x, which induces faster dynamics in the TMV (it can be seen also through the reduction of time duration of the membrane conductances dynamics reported in Fig. 12).

A further validation of the model is performed by comparing these time shapes with those reported in [56]. together with the agreement of the simulated rate constant α_i and β_i with those reported in [49]

Another particularly meaningful remark concerns the possibility to reproduce nervous stimulus propagation offered by the models. Specifically, in accord to Hodgkin and Huxley experimental setup, once the resting state conditions have been achieved over all the structures, a potential difference, beyond the natural excitement threshold, can be fixed across membrane at any transversal section (in this case at $z = 0$) of the models to elicit a local action potential. This propagates along the considered axon segment, thanks to the well-known physiological mechanisms proper of non-myelinated fibres, whose reproduction was the objective of this phase of simulation.

a)

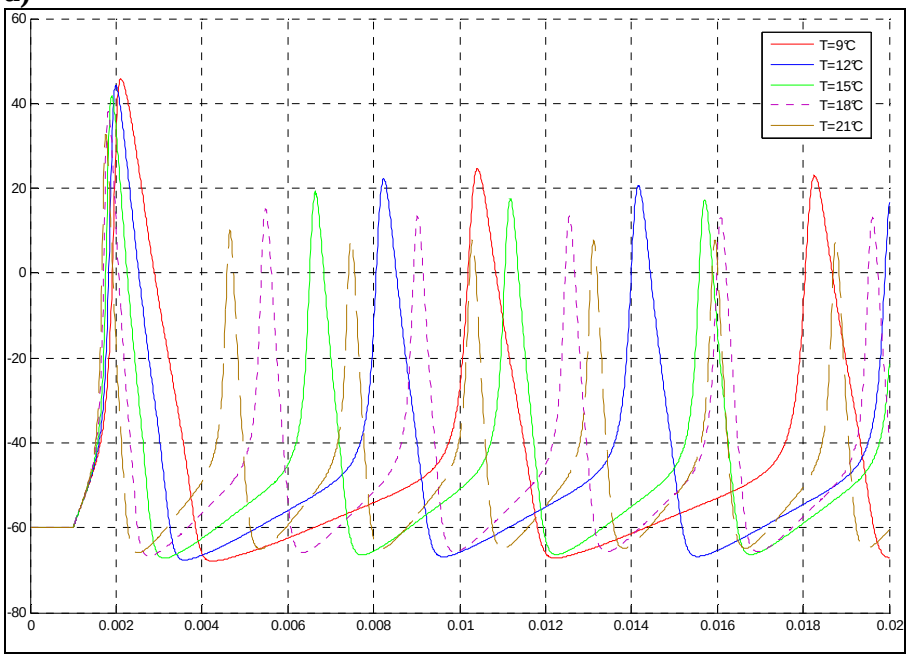
T=9℃
T=12℃
T=15℃
T=18℃
T=21℃
60
40
20
0
-20
-40
-60
-80
0
0.002
0.004
0.006
0.008
0.01
0.012
0.014
0.016
0.018
0.02

b)

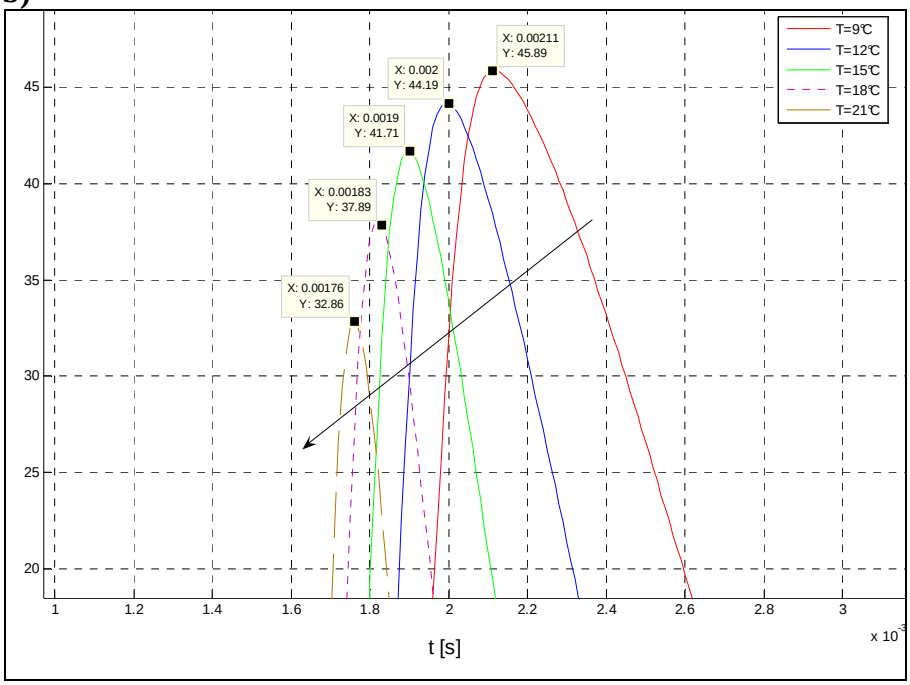
T=9℃
T=12℃
T=15℃
T=18℃
T=21℃
X: 0.00211
Y: 45.89
X: 0.002
Y: 44.19
X: 0.0019
Y: 41.71
X: 0.00183
Y: 37.89
X: 0.00176
Y: 32.86
45
40
35
30
25
20
1
1.2
1.4
1.6
1.8
2
2.2
2.4
2.6
2.8
3
x 10^-3
t [s]

c)

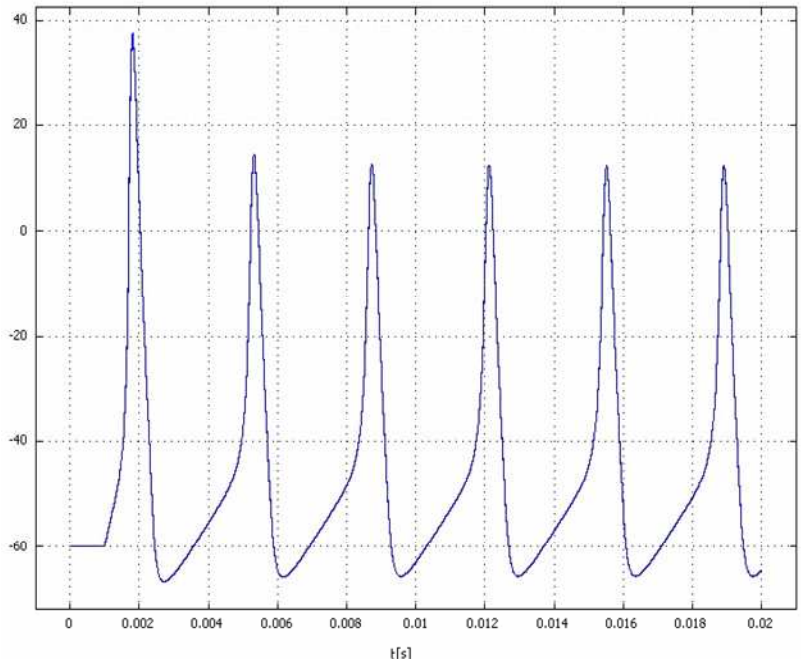

Fig. 14 a) Multiple APs at different temperatures b) Zoom on the first AP peak c) at a particular temperature: *T*=18.3°C

In particular, in the two model solutions this is achieved by fixing a 15mV voltage difference across axon membrane in the point whose coordinates are r=0.5μm and z=0, thus obtaining the propagation effect shown in Fig. 15.The explanation of these results is the presence in a certain instant of an AP in an area (the *active zone*, emulated constraining TMV).This implies that the inner side of the membrane is "more positive" with respect to the outer one. The charge distribution non-homogeneity, thus created, induces longitudinal potential gradients; these in turn generate electric currents (known as *local currents*) in both intra and extra-cellular media, whose lines merge into the active zone (Fig. 16(a) and (b)). All this process results, as it would have been expected theoretically, in the activation of the other near areas interested by these charge fluxes.

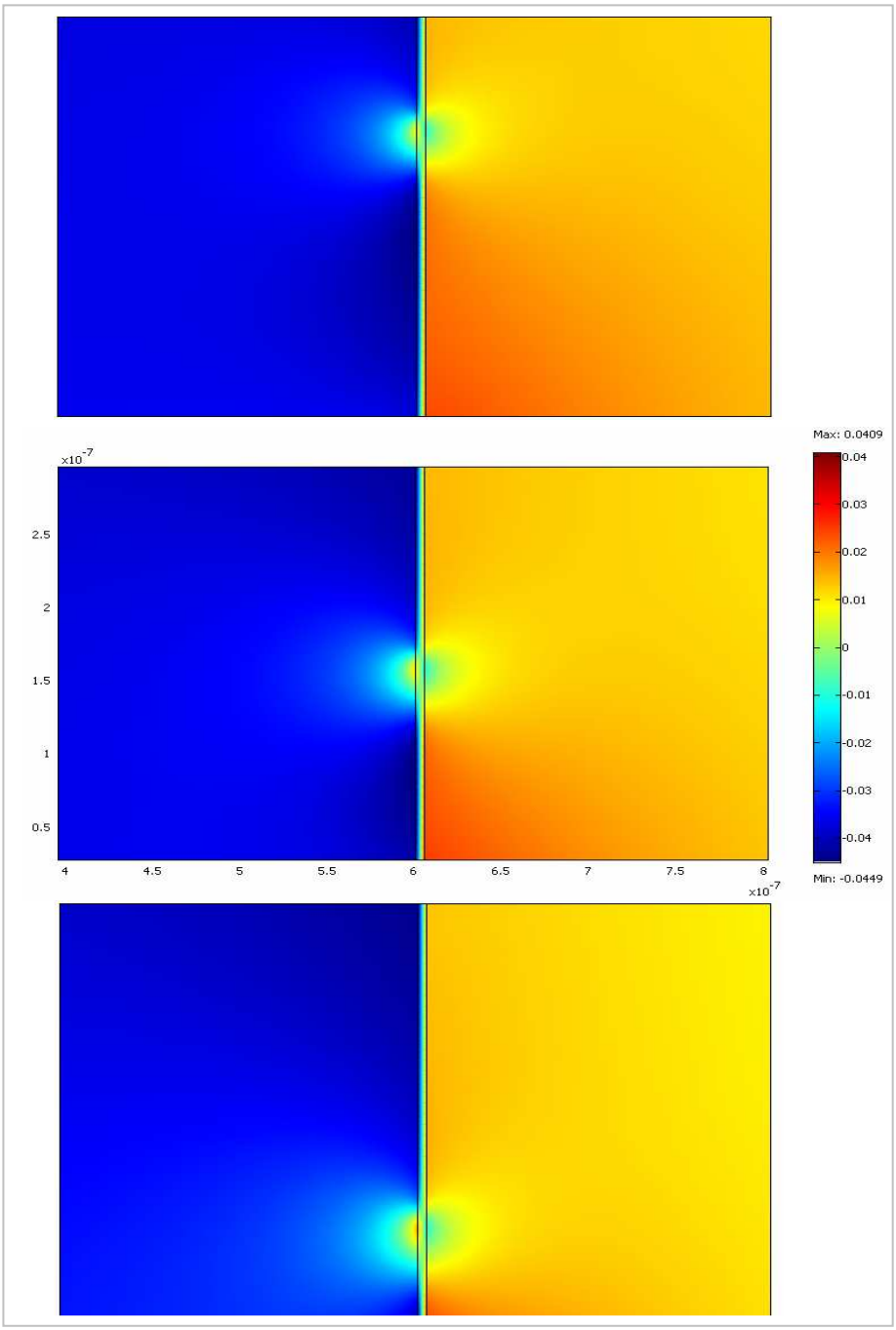

Fig. 15 Propagation phenomenon: the moving active zone. Potential map at three different times of pulse conduction (Axes [m], Voltage [V])

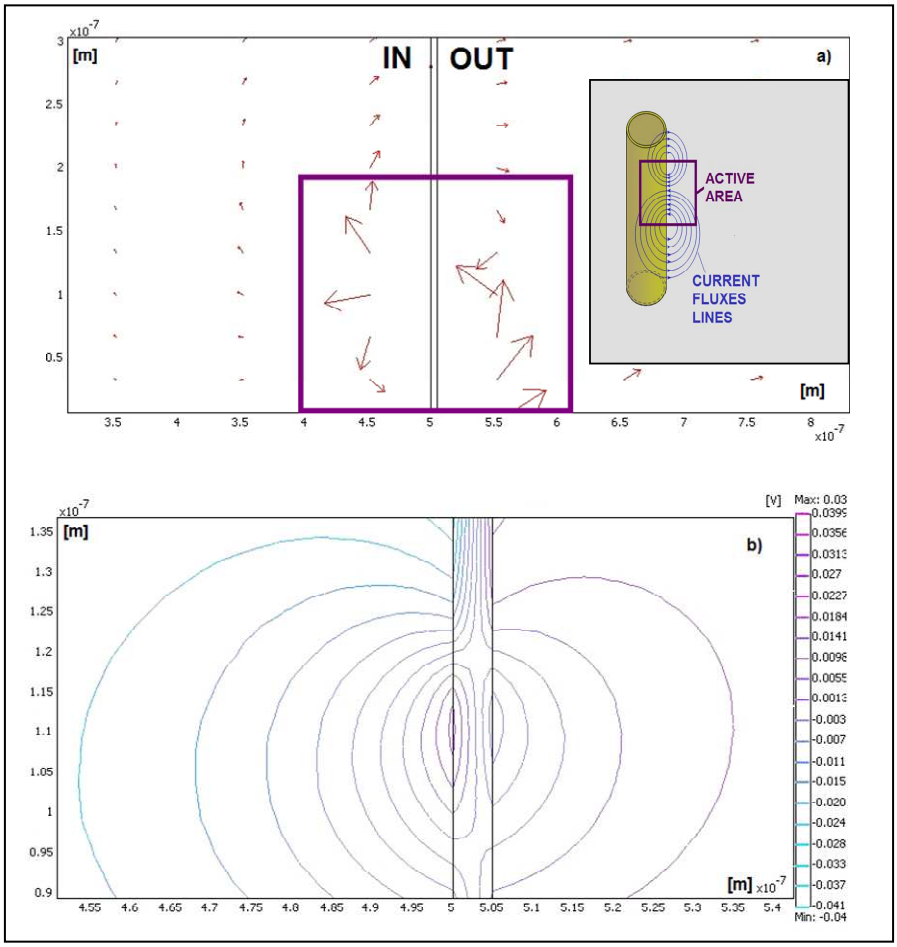

Fig. 16 a) Simulation results for local currents in an activated zone compared with literature behaviour in the inset [56]. b) Zoom on active zone: electric potential lines inside and outside membrane, for model A. (Axis [m], Voltage [V])

Simulation results for model A are reported to show equipotential lines distribution within an activated section of membrane domain (Fig. 16(b)). The visualization of the propagation effect would not have been easy if actual electric properties of external means and axoplasm domains had been used in the simulation environment: the time an AP needs to pass all along the segment implemented is of the same order of amplitude of a reasonable discretization time step.

So, in order to make propagation phenomenon not "instantaneous", but better "visible" at this phase of model testing, a choice has been done to divide the two dielectric constants and electric conductivities of those domains by the appropriate factor 10^6. Indeed, a theoretical approximation of propagation speed is (11):

$$v = \sqrt{\frac{Ka}{2C_m \rho_i}} \tag{24}$$

where v is propagation speed [m/s], K the constant 10470 [1/s], a axon radius [cm], ρ_i axoplasm resistivity [Ω cm] as those used by Hodgkin and Huxley. It is, thus, possible to understand why the simulated velocity is a thousand times smaller than the real one, since $\rho_{isimulated}=10^6\rho_{ireal}$.

3.3 3D model of the neurostimulation system

Once obtained the 2D representation of the main axon features, the steps towards the implementation of the whole neurostimulation system go through the realization, as previously cited, of the axon segment model.

3.3.1 Single axon segment FEM model

The structure depicted in Fig. 17 represents the segment of the axon with the alumina layer and the nanoelectrodes as stimulating agents.
We have started the 3D model construction, by modelling a segment of the axon to reduce calculus burden. The structure depicted in Fig. 17 represents the segment of the axon with the alumina layer and the nanoelectrodes as stimulating agents.
A 3D transient analysis packet of the Quasi-Static Electric AC/DC module (for the same reasons described in § 3.2.2) and a time dependent analysis of the PDE module in general form have been adopted to simulate the depicted piece of the system in the chosen commercial environment. In particular, the containing box is modelled by the domain D_e, a parallelepipedon whose dimensions are

5.1μm×4.5μm×4.8μm and characterized by its dielectric constant and electric conductivity, respectively ε_e and σ_e. The nanoelectrode is represented by a cylinder (length: 1.4μm and radius: 400nm).

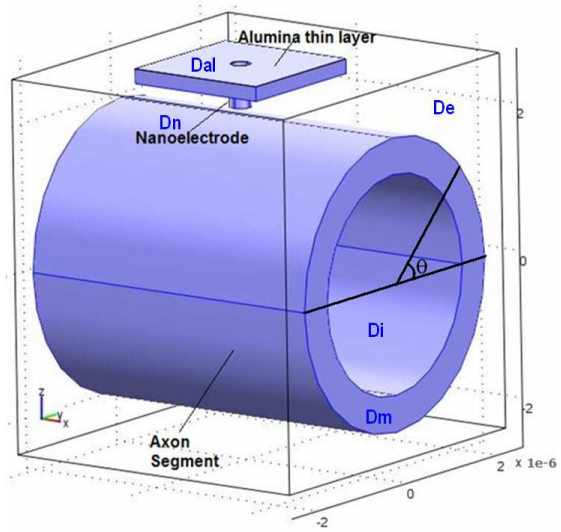

Fig. 17 Sketch of the modeled neurostimulation system (when only the axon segment is taken into account)

Alumina thin layer is modelled by D_{al} domain and its dimensions are 2μm×2μm×0.2μm , while its electromagnetic parameters are ε_e and σ_e. Moreover we have modelled the axon as a 4.5μm long segment, with a 2μm long.

As far as its membrane is concerned, it has been scaled (increasing its value) defining its corresponding domain, in order to avoid meshing troubles as those already mentioned for the 2D model. Trials with different scaling factors have been performed, to check the different extent of the approximation introduced. In the trade-off between the correctness of the result and the easiness of meshing in FEM modelling a maximum error (below 3%) in voltage values over the examined structure has been accepted associated to a scaling factor of 10^2[57].

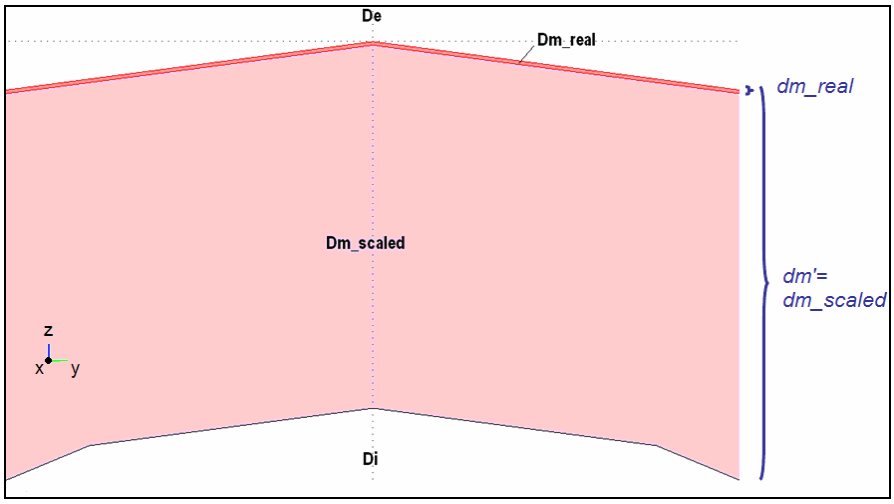

Fig. 18 Zoom at the top of the implemented membrane domain: visual comparison (in plane y-z) between the real value of the membrane domain thickness d_{m_real} and the actually implemented scaled one d_m'

Thus real membrane thickness is

$$d_m = 5 \cdot 10^{-9} \text{ [m]} \tag{25}$$

while its implemented scaled value is

$$d_m' = 5 \cdot 10^{-7} \text{ [m]} \tag{26}$$

Thus, the scaled membrane conductivity and dielectric permittivity can be determined as

$$\sigma_m' = \frac{\sigma_m d_m'}{d_m} \text{ [S/m]} \tag{27}$$

$$\varepsilon_m' = \frac{\varepsilon_m d_m'}{d_m} \text{ [F/m]} \tag{28}$$

where σ_m and ε_m are determined using equations (9), (10) and (11) together with all other previously reported HH set of equations (§3.2.2).

All EM parameters are reported in Table 8, other constants and general parameters linked to HH equations are the same as those reported in Table 2 and Table 3.

Table 8. Simulation times in [s]. Stimulus duration: short (d), long (D). Stimulus amplitude: low (a), high (A)

Parameter	Value	Description
σ_{Ax}	5[S/m]	Axon electric conductivity
ε_{Ax}	200[F/m]	Axon dielectric permittivity
σ_{Ext}	1[S/m]	External medium electric conductivity
ε_{Ext}	200[F/m]	External medium dielectric permittivity
σ_{Al}	10^{-3}[S/m]	Alumina electric conductivity
ε_{Al}	9.7[F/m]	Alumina dielectric permittivity
σ_{n}	10^{6}[S/m]	Nanoelectrode electric conductivity
ε_{n}	10[F/m]	Nanoelectrode dielectric permittivity

Current continuity equation, as in 2D case, is set on every domain, thus coupling Maxwell equations in their Quasi Static formulation with HH ones, implemented on D_m (exploiting the cited PDE packet for *m*, *n* and *h* activation variables determination) in full analogy with the method used and above described for the 2D case.
The main differences with it, nevertheless, concern the definition of the external current density impressed on the membrane domain (taking into account the Nernst Potentials), the definition of the initial conditions over it and of all the boundary conditions on the analysed structure and, in the end, the implementation method adopted for the extrusion of the external and internal electric potentials to define the TMV, V_m, within D_m.
First of all, it is necessary to highlight that, $\bar{\boldsymbol{J}}_{\boldsymbol{ext}}$, the externally impressed current density, in this case, becomes

$$\bar{\boldsymbol{J}}_{\boldsymbol{ext}} = \begin{cases} J_e \hat{\boldsymbol{r}} = J_e \cos(\theta(y,z))\,\hat{\boldsymbol{x}} + J_e \sin(\theta(y,z))\hat{\boldsymbol{y}} & \text{on } D_m \\ 0 \text{ elsewhere} \end{cases} \tag{29}$$

where J_e is defined as in (16)

$\bar{\boldsymbol{r}}$ is defined by:

$$\bar{\boldsymbol{r}} = \hat{\boldsymbol{r}}\, r = \hat{\boldsymbol{r}}\sqrt{\mathrm{y}^2 + \mathrm{z}^2} \tag{30}$$

and θ is:

$$\theta(y,\mathrm{z}) = \begin{cases} a\tan 2\,(z,y) \\ \left|a\tan 2\,(z,y)\right| + \pi \end{cases} \tag{31}$$

In addition to this, initial and boundary conditions settings are arranged as follows:

$$\begin{cases} V_m(t=0) = Ar + B \text{ on } \mathrm{D_m} \\ V(t=0) = \text{elsewhere} \end{cases} \tag{32}$$

where

$$\begin{aligned} A &= 10^{-3}\,\frac{V_{sta}}{r_1 - r_2} \\ B &= -Ar_2 \end{aligned} \tag{33}$$

fixing an initial linear distribution of electric potential over $\mathrm{D_m}$ ranging from -60mV at r_1 (1.5μm) to zero at r_2 (2μm) - respectively inner and outer radii defining $\mathrm{D_m}$ domain.

For the channel activation variables, initial conditions have been set to:

$$\begin{cases} m(t=0) = m_0 = \dfrac{a_{msta}}{a_{msta} + b_{msta}} \\ n(t=0) = n_0 = \dfrac{a_{nsta}}{a_{nsta} + b_{nsta}} \\ h(t=0) = h_0 = \dfrac{a_{hsta}}{a_{hsta} + b_{hsta}} \end{cases} \tag{34}$$

with a_{ista} and b_{ista} ($i \in \{m,n,h\}$) defined in Table 2.

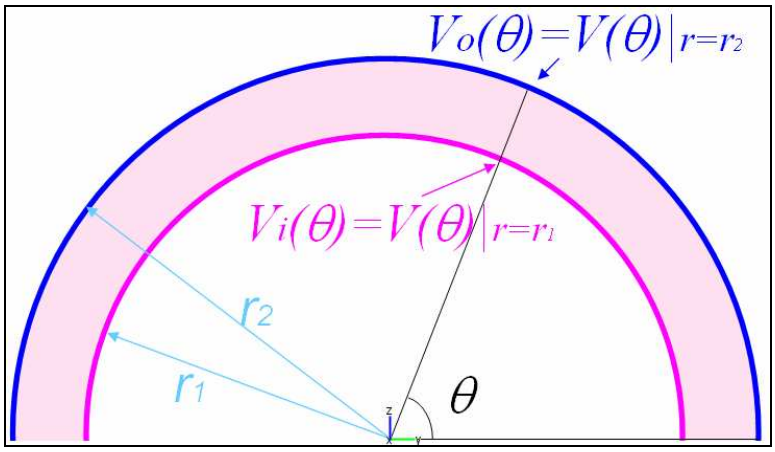

Fig. 19 Definition of inner and outer potential Vo and Vi for extrusion

Finally the extrusion of the external and internal electric potentials to define the TMV, V_m, within the membrane domain D_m is performed according to the transformation defined in Table 9.

Table 9 Extrusion transformation from n the most general form: when the source domain is 3D

Source Transformation	Destination Transformation
$\begin{cases} X_{src} = S_x(x) = x \\ Y_{src} = S_y(y,z) = \theta \end{cases}$	$\begin{cases} X_{dest} = D_x(x) = x \\ Y_{dest} = D_y(y,z) = \theta \end{cases}$
$V_o(\theta) = V(\theta)\big\|_{r=r_2}$ → Extruded Variable: $V_o(\theta) = V(\theta)\big\|_{r\in[r_1,r_2]}$	
$V_i(\theta) = V(\theta)\big\|_{r=r_1}$ → Extruded Variable: $V_i(\theta) = V(\theta)\big\|_{r\in[r_1,r_2]}$	

3.3.1.1 Analysis of some simulations results

Now that a description of the modelling phases has been performed and model settings have been delineated, it is possible to present some of the many simulations results obtained, in order to delineate the potentiality of the model just presented and to show that it behaves as theoretically expected.

In particular, since the implementation steps we have made are

based on an incremental approach (starting from the 2D model and its approximations to the 3D axonal until the model with soma, axon hillock and initial axon segment) we have tested all our models (as for the 2D case) with amplitudes supposed to elicit APs and with signal too low to induce and active response and we have observed whether they responded accordingly in both axon and model of the soma zone.
In this section we will go through a very brief description of only axonal model, while (after having described it) we will do the same for the much more complex one including soma, axon hillock and initial axon segment.
Therefore, under and overthreshold stimuli have been used to test the passive electrotonic potential generation and the active AP birth respectively.

As far as boundary conditions are concerned, the following assumptions are made (J_{sta}, 42.23μA/m^2, is the current density value at resting state of HH model, defined in eq.(15)):

Table 10 Boundary conditions assignments for the model depicted in Fig. 17

Boundary	**Imposed condition**
Bottom of the external box	Ground
Upper and later boundaries of the external box	Electrical insulation
Inner lateral surface defined by r_1	Current source: $\bar{\boldsymbol{J}}_{source} = \hat{\boldsymbol{r}} J_{sta}$
Circular upper base of the nanoelectrode	Electric potential: $V_{input}(t)$
Other inner boundaries	Continuity of the normal component of current density

where $V_{input}(t)$ is the externally applied electric stress. Whereas, over the boundaries delimiting domain D_m, for the activation variables, the Neumann condition is set, fixing to zero the normal derivative of them. Temperature coefficient is taken into account as in (21).

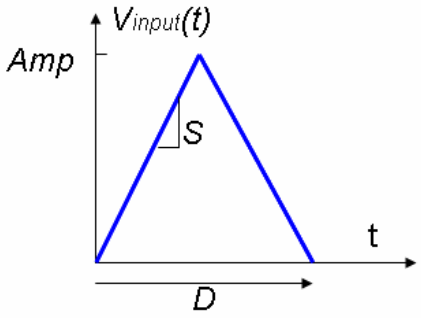

Fig. 20 Input voltage waveform

When $V_{input}(t)$ (Fig. 20) is an underthreshold symmetrical triangular waveform (amplitude -15mV, absolute slope S of 20V/s and duration of D=0.75ms) no AP is elicited, as theoretically expected and as shown in Fig. 21 and Fig. 22.

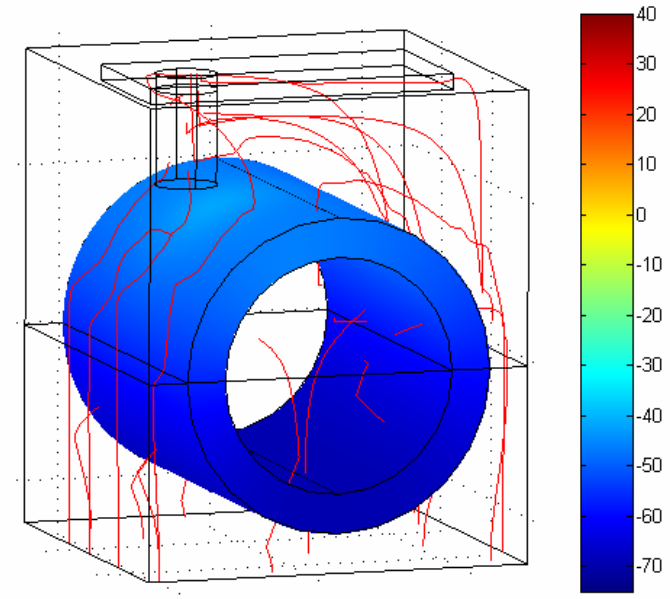

Fig. 21 Correct underthreshold behaviour of the axon. Colormap: V_m [mV] at t=1.4ms, near the time in which the maximum voltage is reached. In red current density flux lines

In particular, an electrotonic passive behaviour can be observed in Fig. 22, where the comparison with Fig. 24 clearly demonstrates the totally different membrane response.

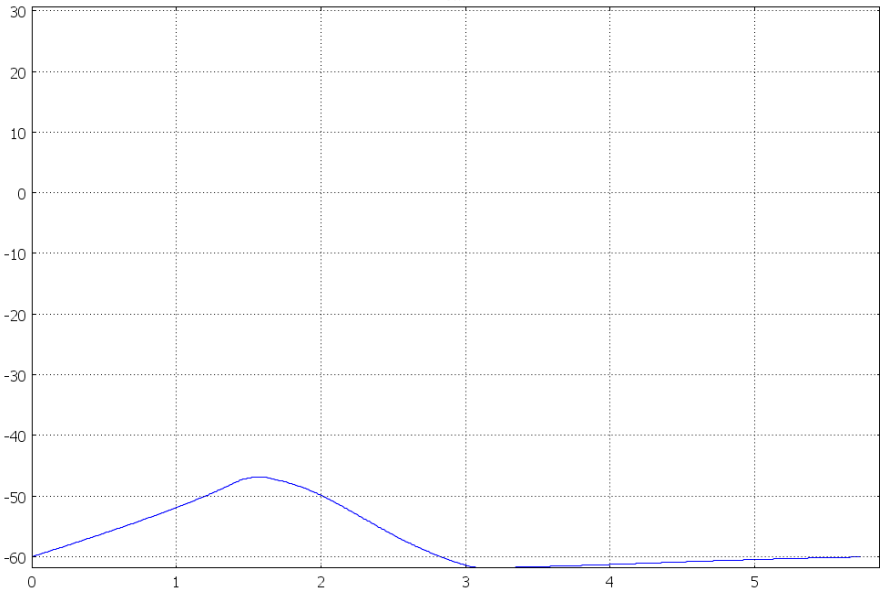

Fig. 22 $V_m(t)$ [mV] vs t[ms]. Understimulation: only electrotonic passive response

Indeed, it shows the effects of an overthreshold stimulus (triangular shaped voltage waveform, but with an amplitude of -100mV and a slope of 200V/s, D= 0.5ms) .

Another interesting test situation is the response to a repetitive stress. In Fig. 25 two APs elicited (the second lower in amplitude as expected, because the relative refractory period is not respected), when input voltage stress is a simple train of a couple of triangular waveforms (blue line). Instead with two nearer input pulses while a first AP is triggered the second one cannot start (Fig. 26).

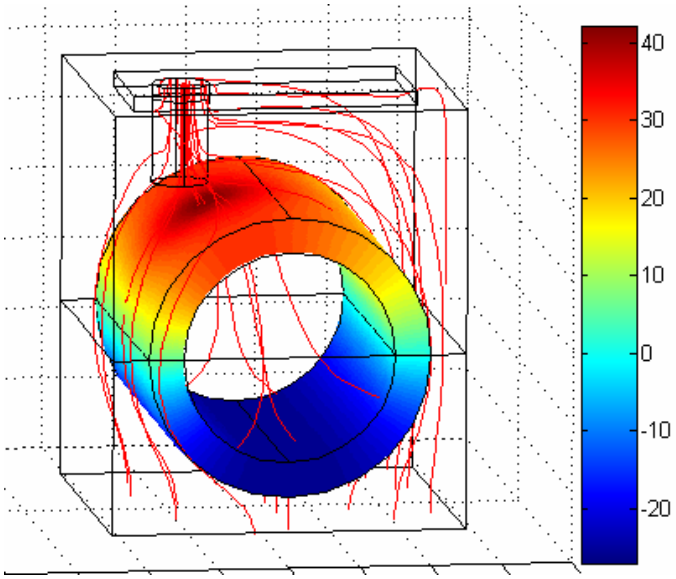

Fig. 23 Correct overthreshold behaviour of the axon. V_m [mV] at t=0.525ms, near the time in which the maximum voltage is reached. In red current density flux lines

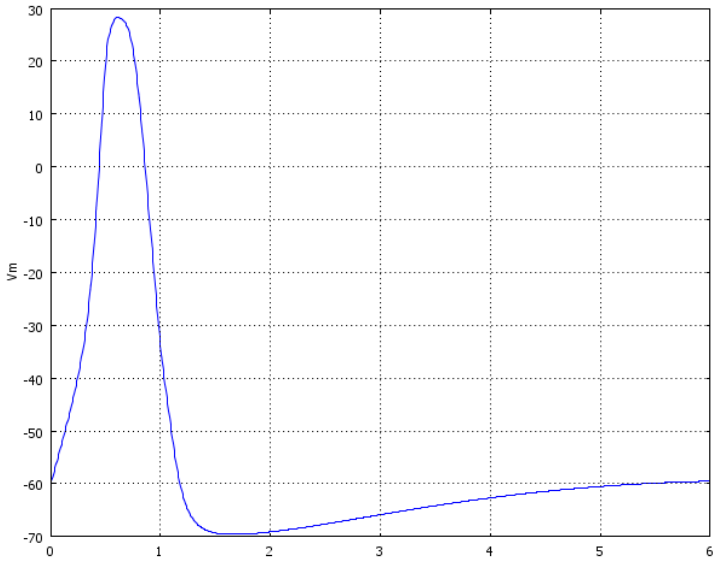

Fig. 24 Elicited AP in correspondence of a point 2.5µm translated along x from the projection of the nanoelectrode on the axon. *Vm*[mV], *t*[ms]

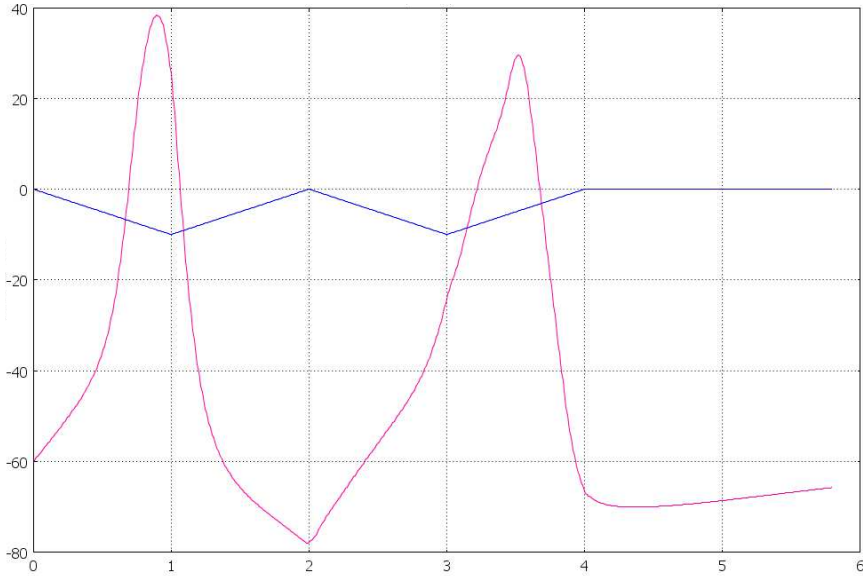

Fig. 25 Pink ($V_m(t)$[mV] vs t[ms]): two APs elicited (the second lower in amplitude as expected). Blue: input voltage stress

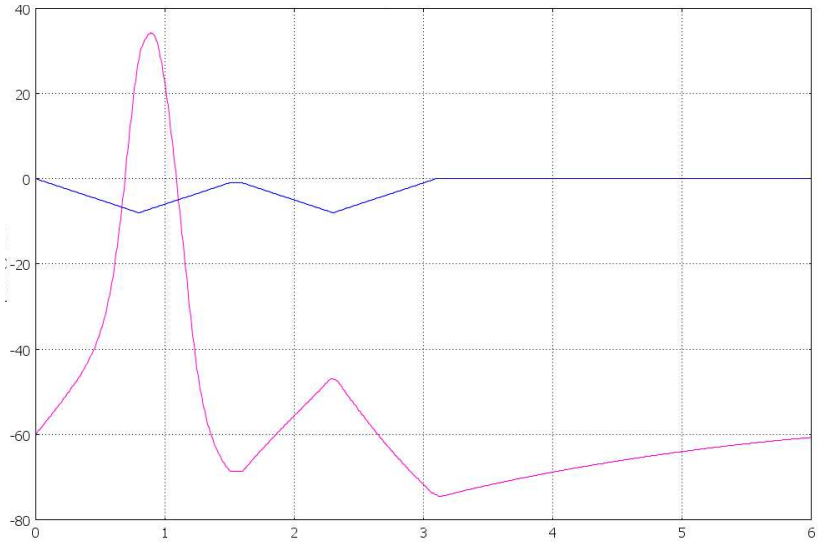

Fig. 26 Two nearer pulsed (blue) elicit only one AP: $V_m(t)$[mV] vs t[ms] (pink). The second peak is an electrotonic potential

Moreover, for the same reasons expressed in 3.2.4,(see also eq.(24)), exactly as we have done for the 2D case, we have scaled dielectric constants and electric conductivities of axon and internal medium domains to "slow down" the propagation velocity and make it more "appreciable", which, here too (see § 3.2.4) is a scaled version of the real one. Fig. 27 depicts the obtained time shift in AP triggering at two different points along the axon membrane (here the nanoelectrode is centred on the axon symmetry axis).

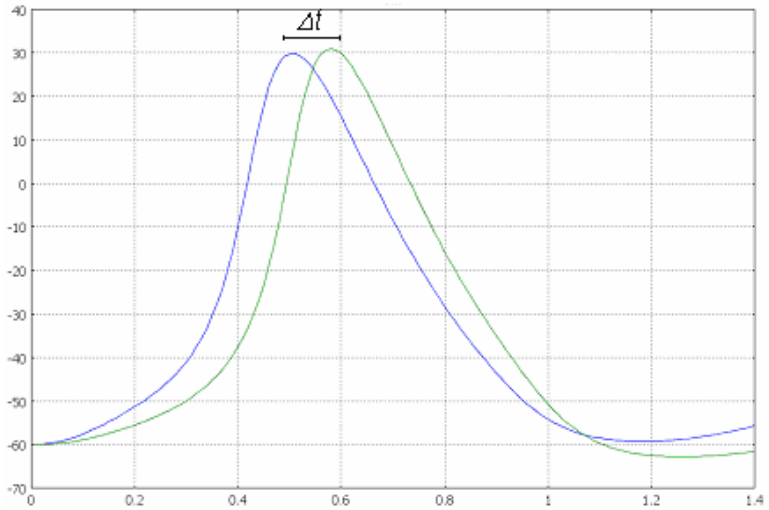

Fig. 27 APs (Vm(t) [mV] , t[ms]). Δt is the delay between two points shifted by a couple of microns

In the end, Fig. 28 depicts three different "pictures" of the model at three different time instant to show propagation effect. The colormap represents the TVM $V_m(t)$ From up to down, structure at t=0.5ms, t= 0.78ms, t=0.98ms: colormap V_m [mV]. Active zones (fluxes lines of current density in red) are moving from the "shadow zone" just under the nanoelectrode, spreading in all directions longitudinal (along x) and along θ. To sum up, as expected, when $V_{input}(t)$ has not a sufficient combination of amplitude and duration, indeed, only the

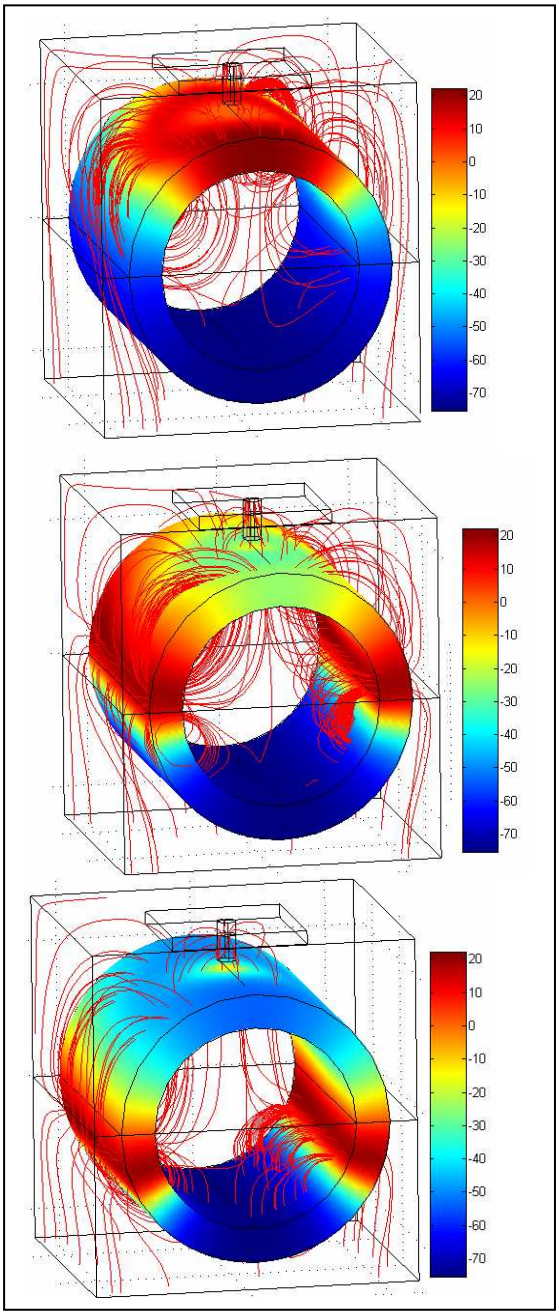

Fig. 28 From up to down, structure at *t*=0.5ms, *t*= 0.78ms, *t*=0.98ms: colormap V_m [mV]. Moving active zones (fluxes lines of current density in red)

passive electrotonic potential is generated [56], while, with an appropriate stimulus the elicitation of an AP is observed; moreover, an APs bursting is induced across the axon membrane when the refractory period is respected, while, as it should be, no second AP comes if it is not. In the end, propagative effect has been observed. All this checks attest the correctness of the model and make of it a possible tool to exploit for investigations on axonal response to the different main parameters if the neurostimulating system.

3.3.2 Model with soma, axon hillock and axon initial segment

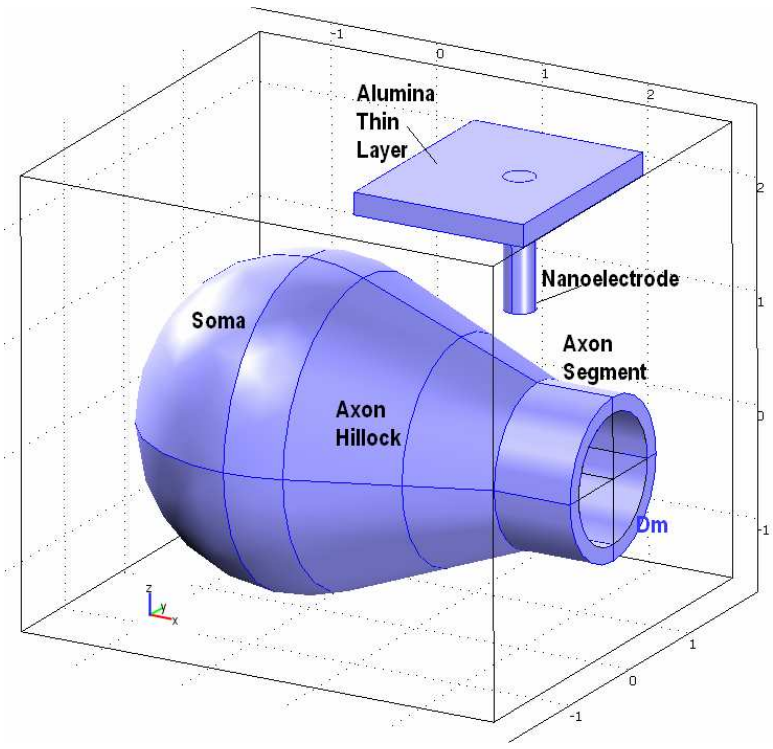

Fig. 29 Sketch of the modeled neurostimulation system when the neuron is stimulated in proximity of the soma(axes are in μm)

In Fig. 29, the sketch representation is reported of the modelled neurostimulation system when the operating condition contemplates

an external stress to be performed in proximity of the soma. Obviously, as it happened for the single axon segment, the majority of the settings referring to neuron membrane are made in analogy with those reported in 3.2.2, thus in this paragraph only the differences with the previously described model will be discussed.

First of all, here the soma and the axon hillock (where the physiological different distribution of channel density is taken into account) are modeled together with the initial segment of the axon departing from it.

Reminding that our primary goal is always to achieve the better model solution and, thus, a flexible and manageable tool to perform the automated procedure, in determining the most relevant factors, when interfacing with the neuron, as we have proficiently done in the bidimensional case, we, now, perform (in 3D) a comparison between a base model and a thin layer approximated one.

To reduce computational burden, which proves to be really high in the base model (the one with membrane domain implemented), a slight reduction in soma and axon dimensions has been introduced in the two geometries that we compare (obviously the same for both), with respect to the typical literature values, nevertheless, as we will show in the dedicated paragraph 4.3.2, the DoE implemented procedure is, obviously, based on more classical literature values.

The geometrical structure is, then, composed as follows: a sphere (3 μm diameter), intercepting a trunk of cone (and representing the axon hillock (1.6μm long) and cylinder corresponding to the axon initial tract (0.7μm long) inserted in an external box (4.5μm × 4μm × 4μm) .The nanoelectrode is 1.6 μm long and has a diameter of 300nm

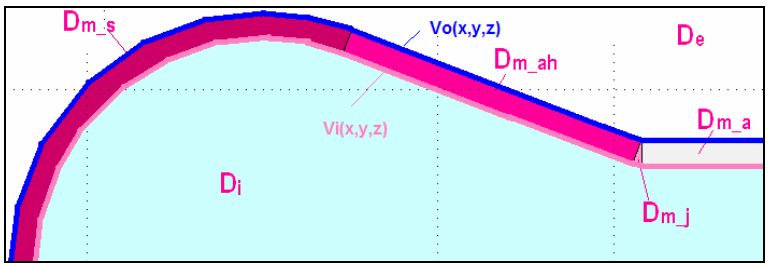

Fig. 30 Piece of the transversal section (in plane x-z) of the model depicted in Fig. 29. Different sections are highlighted whose union constitutes membrane domain Dm. Inner $V_i(x,y,z)$ (pink) and outer voltage $V_o(x,y,z)$ (blue)

As far as the physical settings are concerned, clearly the settings of the external current density, as well as initial and boundary conditions and the extrusion transformation must be rearranged depending on the zone where they apply (soma, axon, etc.). In particular, the externally impressed current density is differentiated in its definition as follows (it must be foregrounded that a junction section has been introduced as in Fig. 30 to connect continuously hillock and axon sections):[1]

Table 11 Summary of equations, variables, boundary and initial settings imposed on the different D_m sections.

Soma (D_{m_s})

$$\bar{\boldsymbol{J}}_{\boldsymbol{ext}} = J_e \hat{\boldsymbol{r}} = J_e \; f_x \; \hat{\boldsymbol{x}} + J_e \; f_y \hat{\boldsymbol{y}} + J_e \; f_z \; \hat{\boldsymbol{z}}$$

$$\begin{cases} f_x = sin(\theta_n(y,z)) \cdot cos(\varphi_n(y,z)) \\ f_y = sin(\theta_n(y,z)) \cdot sin(\varphi_n(y,z)) \\ f_z = cos(\theta_n(y,z)) \end{cases}$$

$$\bar{\boldsymbol{r}} = \hat{\boldsymbol{r}}\, r = \hat{\boldsymbol{r}} \sqrt{\mathrm{x}^2 + \mathrm{y}^2 + \mathrm{z}^2}$$

$$\begin{cases} \theta_n(\mathrm{x}, y, \mathrm{z}) = a\cos\left(\dfrac{z}{r}\right) \\ \varphi_n(\mathrm{x}, y, \mathrm{z}) = a\tan 2(y,x) + 2\pi \end{cases}$$

$$\begin{cases} \theta_s(\mathrm{x}, y, \mathrm{z}) = a\cos\left(\dfrac{z}{r}\right) \\ \varphi_s(\mathrm{x}, y, \mathrm{z}) = a\cos\left(\dfrac{x}{r}\right) \end{cases}$$

: modified set of variables used for the extrusion

Initial condition for electric potential:

$$V_m(t=0) = Ar + B$$

[1] The explanation of the choices made in the mathematical modelling of the different D_m sections is reported in §3.3.2.2.

$A = 10^{-3}\frac{V_{sta}}{r_1 - r_2}$, with ($V_{sta}$ = -60·10^{-3})

$B = -Ar_2$

r_1 and r_2 are: inner and outer radii defining soma membrane

Initial condition for the activation variables:

$$\begin{cases} m(t=0) = m_0 = \dfrac{a_{msta}}{a_{msta} + b_{msta}} \\ n(t=0) = n_0 = \dfrac{a_{nsta}}{a_{nsta} + b_{nsta}} \\ h(t=0) = h_0 = \dfrac{a_{hsta}}{a_{hsta} + b_{hsta}} \end{cases}$$

a_{ista} and b_{ista} ($i \in \{m,n,h\}$) (see Table 2)

Axon Hillock (D_{m_ah})

$\overline{\boldsymbol{J}}_{\boldsymbol{ext}} = J_e \hat{\boldsymbol{r}} = J_e\ f_x\ \hat{\boldsymbol{x}} + J_e\ f_y \hat{\boldsymbol{y}} + J_e\ f_z\ \hat{\boldsymbol{z}}$

$$\begin{cases} f_x = sin(\theta_y) \\ f_y = cos(\theta_y) \cdot cos(\vartheta_c) \\ f_z = cos(\theta_y) \cdot sin(\theta_c) \end{cases}$$

$$\begin{cases} \theta_x = \theta_c - \dfrac{\pi}{2} \\ \theta_y = a\tan(0.379) \\ \theta_z = 0 \end{cases}$$

$$\theta_c = \begin{cases} a\cos\left(\dfrac{y}{r_c}\right) \\ 2\pi - a\cos\left(\dfrac{y}{r_c}\right) \end{cases}$$

$$\bar{\boldsymbol{r}}_c = \hat{\boldsymbol{r}}\, r = \hat{\boldsymbol{r}}\sqrt{y^2 + z^2}$$

$$\begin{cases} x_2 = \cos(\theta_z)\cos(\theta_y)(x-a) + (\sin(\vartheta_z)\cos(\theta_x) + \cos(\vartheta_z)\sin(\theta_y) \\ \qquad + (\sin(\theta_z)\sin(\theta_x) - \cos(\theta_z)\sin(\theta_y)\cos(\theta_x))(z-c) \\ z_2 = \sin(\vartheta_y)(x-a) - \cos(\vartheta_y)\sin(\vartheta_x)(y-b) + \cos(\vartheta_y)\cos(\vartheta_x)(\end{cases}$$

$$\begin{cases} a = 4.601 \cdot 10^{-6} \\ b = r_{abc}\cos(\theta_c) \\ c = r_{abc}\sin(\theta_c) \\ r_{abc} = 1.211 \cdot 10^{-5} \end{cases}$$

$$\begin{cases} G_{Na} = G'_{Na\,max} m^3 h \\ G_K = G'_{K\,max} n^4 \\ \dfrac{G'_{Na\,max}}{G_{Na\,max}} = \dfrac{G'_{K\,max}}{G_{K\,max}} = 10 \end{cases}$$

Initial condition for electric potential:

$$V_m(t=0) = A|z_2| + B$$

$A = 10^{-3}\dfrac{V_{sta}}{z_{2_1} - z_{2_2}}$, with ($V_{sta}$ = -60·10^{-3})

$B = -Az_{2_2}$

$z_{2_1} = 0$, $z_{2_2} = d_m'$ where d_m' is the scaled membrane thickness (as in (26))

Initial condition for the activation variables:
The same as for the D_{m_s} section.

Junction Section(D_{m_j})

$$\bar{\boldsymbol{J}}_{\boldsymbol{ext}} = J_e \hat{\boldsymbol{r}} = J_e\ f_x\ \hat{\boldsymbol{x}} + J_e\ f_y \hat{\boldsymbol{y}} + J_e\ f_z\ \hat{\boldsymbol{z}}$$

$$\begin{cases} f_x = \cos(\pi + \beta_j - \gamma_r) \\ f_z = \sin(\pi + \beta_j - \gamma_r) \cdot \cos(\vartheta_c) \\ f_y = \sin(\pi + \beta_j - \gamma_r) \cdot \sin(\vartheta_c) \end{cases}$$

$$\beta_j = \begin{cases} a\tan 2(z_3, x_3) & \text{if } z_3 \neq 0 \\ 0 & \text{if } z_3 = 0 \end{cases}$$

$$\bar{\boldsymbol{r}}_j = \hat{\boldsymbol{r}}\, r = \hat{\boldsymbol{r}}\sqrt{y^2 + z^2}$$

$$\begin{cases} \theta_x = \theta_c - \frac{\pi}{2} \\ \theta_y = a\tan(0.183) \\ \theta_z = 0 \end{cases}$$

$$\theta_c = \begin{cases} a\cos\left(\frac{y}{r_j}\right) \\ 2\pi - a\cos\left(\frac{y}{r_j}\right) \end{cases}$$

$$\gamma_j = \vartheta_y$$

$$\begin{cases} x_3 = \cos(\theta_z)\cos(\gamma_r)(x - P_a) + \\ \quad + (\sin(\theta_z)\cos(\theta_x) + \cos(\theta_z)\sin(\gamma_r)\sin(\theta_x))(y - P_b) + \\ \quad + (\sin(\theta_z)\sin(\theta_x) - \cos(\theta_z)\sin(\gamma_r)\cos(\theta_x))(z - P_c) \\ \\ z_3 = \sin(\gamma_r)(x - P_a) - \cos(\gamma_r)\sin(\vartheta_x)(y - P_b) + \\ \quad + \cos(\gamma_r)\cos(\vartheta_x)(z - P_c) \end{cases}$$

$$\begin{cases} P_a = 2..16 \cdot 10^{-5} \\ P_b = r_{pabc}\cos(\theta_c) \\ P_c = r_{pabc}\sin(\theta_c) \\ r_{pabc} = 7.2 \cdot 10^{-6} \end{cases}$$

Initial condition for electric potential:

$V_m(t=0) = Az_3 + B$

$A = -\frac{B}{d_m'}$ where d_m' is the scaled membrane thickness (as in (26))

$B = \frac{V_{sta}}{1000}$, with (V_{sta} = -60·10^{-3})

Initial condition for the activation variables:
The same as for the D_{m_s} section.

Axon (D_{m_a})

$\bar{\boldsymbol{J}}_{\boldsymbol{ext}} = J_e\hat{\boldsymbol{r}} = J_e\cos(\theta_a(y,z))\,\hat{\boldsymbol{x}} + J_e\sin(\theta_a(y,z))\hat{\boldsymbol{y}}$

$\bar{\boldsymbol{r}} = \hat{\boldsymbol{r}}\,r = \hat{\boldsymbol{r}}\sqrt{y^2 + z^2}$

$\theta = \theta_a(y,z) = \begin{cases} a\tan 2(z,y) \\ |a\tan 2(z,y)| + \pi \end{cases}$

Initial condition for electric potential:

$V_m(t=0) = Ar + B$

$A = 10^{-3}\frac{V_{sta}}{r_1 - r_2}$, with ($V_{sta}$ = -60·10^{-3})

$B = -Ar_2$

r_1 and r_2 are: inner and outer radii defining soma membrane

Initial condition for the activation variables:
The same as for the D_{m_s} section.

3.3.2.2 Extrusion and meshing difficulties in 3D spherical geometries: adopted solutions and particular settings

Realizing a model for such a complex structure has frequently led, during its implementation, to several modifications in the adopted approaches and strategies, because from time to time different implementation troubles have been highlighted.
The most prominent of these are connected to the mathematical definition of angles, which in turn are necessary for the imposition of the external current density on D_m and for V_m extrusion on it, as well as to the meshing of a still tiny membrane in curved boundaries zones, often leading to inverted mesh elements. In this section a brief overview of the adopted solutions is presented.
It must be noticed that all parameters cited in this sections have been defined according with Table 11.

First of all on D_{m_s}, the definition of the couple of angles capable of univocally identifying a direction for the impressed current density on membrane domain and for the extrusion of inner and out electric potentials V_i and V_o (as depicted in Fig. 30) has initially fallen on the typical defined in the spherical coordinates systems. Nevertheless, the calculation of their values (in particular the function *atan(y/x)* for ϕ) was not correct in correspondence with the boundaries of D_{m_s} where it had a discontinuity. This brought to a change in the definition of the φ angle, leading to the definition of a new variable that (in couple with the usual expression of θ) have been used to define the direction:

$$\begin{cases} \theta_S(\mathrm{x}, y, \mathrm{z}) = a\cos\left(\dfrac{z}{r}\right) \\ \varphi_S(\mathrm{x}, y, \mathrm{z}) = a\cos\left(\dfrac{x}{r}\right) \end{cases} \tag{35}$$

while θ_n and ϕ_n (Table 11) are used to calculate impressed current density $\bar{\boldsymbol{J}}_{\boldsymbol{ext}}$. There are also other expressions adopted to solve modelling issues, but this was a particularly meaningful example in

order to show how a simple mathematical definition can necessitate of slight adjustment to be implemented in FEM.

In addition to this, failures of the solver due to its reported impossibility to invert source transformation in soma extrusion of V_o and V_i (see §3.2.1) have been discovered as effects of the presence of inverted mesh elements. Often along a curved boundary it is possible to have (if a not extremely refined mesh is used to reduce computational burden) a coarse mesh and this quite likely can cause problems with inverted mesh elements. This means that a mesh element is wrapped inside-out or has zero area (in 2D) or volume (in 3D). More precisely, there are some coordinates for which the Jacobian matrix for the mapping from local to global coordinates has a negative or zero determinant. In most cases, the linear (straight) mesh elements, visible in a mesh plot are not inverted, but the higher-order curved mesh elements used for computing the solution might be. [51]. Hence, studying the minimum element quality in the Mesh Statistics section of the software does not reveal the presence of inverted mesh elements in most cases. Inverted mesh elements in themselves do not pose any immediate threat to the overall accuracy of the solution. However, convergence is not assured. It is, anyway, worth bearing in mind that the faces along which there are inverted elements are less than perfectly resolved. If these faces are important, it is possible to pursue a mesh without inverted elements or at least make sure that the mesh resolution is sufficiently fine to guarantee an accurate solution. The easiest way to get an idea of the accuracy is to try a few different meshes and to see how the solution changes.

It is possible to avoid problems with inverted mesh elements by modifying the geometry or the mesh or reducing the geometry shape order and this is what we have done.

The last solution has allowed us to overcome the difficulty in inverting the source transformation for soma extrusion (Table 12) and inverted mesh elements were definitely avoided.

Moreover a general brief overview on the passages leading to the definition of the variables of Table 11 must be reported. Table is divided in four sections (soma,D_{m_s} ,axon hillock, D_{m_ah}, junction section, D_{m_j} and in the end axon, D_{m_a}).

Soma and axon settings have been already discussed, it is thus necessary to delineate the meaning of the subdomain expression set on

D_{m_ah} and D_{m_j}.

On the first of the two, a new set of coordinates (the base coordinates are fixed on soma spherical domain centre) has been exploited to define extrusion direction normal to the truncated cone external and internal surface. The most appropriate system has been identified in a rototranslated one (translated to the locus of points ($a,b(\theta_c),c(\theta_c)$) -which is the circle indicated in Fig. 31- and rotated with respect to the translated axis z_1 by θ_y see Table 11):

$$\begin{bmatrix} x_2 \\ y_2 \\ z_2 \end{bmatrix} = \overline{\overline{R}} \bullet \begin{bmatrix} x_1 \\ y_1 \\ z_1 \end{bmatrix} = \overline{\overline{R}} \bullet \left(\begin{bmatrix} x \\ y \\ z \end{bmatrix} - \begin{bmatrix} T_x \\ T_y \\ T_z \end{bmatrix} \right) \tag{36}$$

where $\overline{\overline{R}}$ is the well known matrix of axis systems rototranslation. [X_1 Y_1 and Z_1] is the translated system leading to the definition of x_2 , y_2, z_2. Instead θ_x θ_y and θ_z are the rotation angles of the [X_2 Y_2 Z_2] axis with respect to those of [X_1 Y_1 Z_1]) and

$$\begin{bmatrix} T_x \\ T_y \\ T_z \end{bmatrix} = \begin{bmatrix} a \\ b(\theta_c) \\ c(\theta_c) \end{bmatrix} \tag{37}$$

which, in our case does not represent a point, but. since its coordinates are function of θ_c (as indicated in the rough sketch of Fig. 31), it describes the depicted circle of radius r_{abc}.

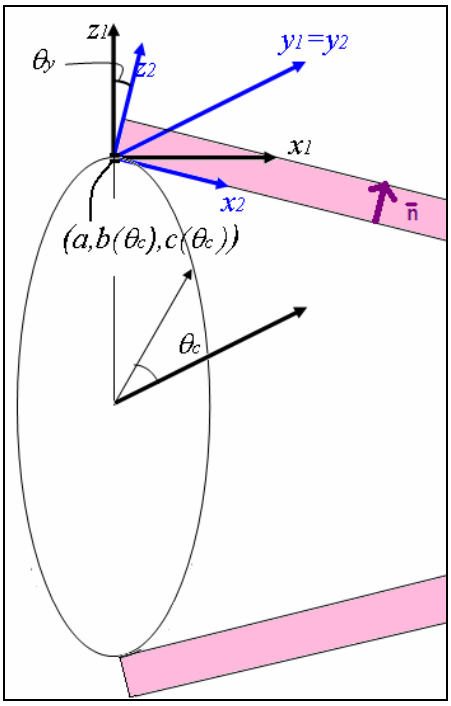

Fig. 31 Sketch of the rototranslated axis to define axon hillock variables and to perform extrusion along normal direction to the axon hillock membrane domain (pink)

Moreover, in order to define the $\bar{J}_{ext}$ three components along x,y and z basis system axis, the following projections are derived, taking into account the variability of the normal vector $\bar{n}$ with θ_c. This leads to the definition of the compontents f_x, f_y, f_z:

$$\begin{cases} f_x = sin(\theta_y) \\ f_y = cos(\theta_y) \cdot cos(\vartheta_c) \\ f_z = cos(\theta_y) \cdot sin(\theta_c) \end{cases} \tag{38}$$

Analogous modelling has been performed for the junction section domain D_{m_j} In particular a new set of axis [X_3 Y_3 Z_3] is defined with x_3 parallel to the light blue segment of Fig. 32 and the locus (P_a,P_b,P_c)

is defined in full analogy with (*a,b,c*) in the axon hillock.

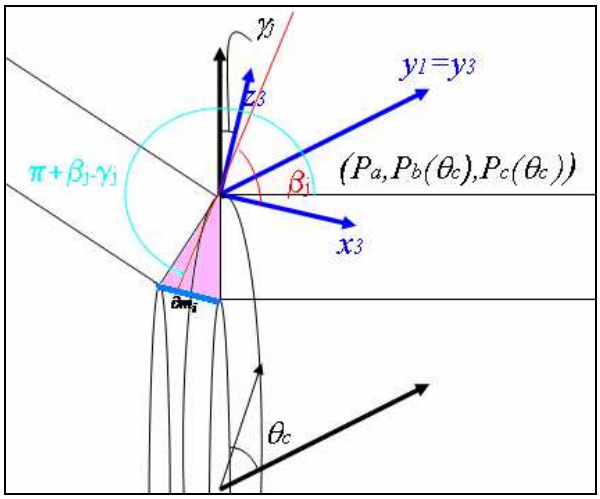

Fig. 32 Sketch of the rototranslated axis [X_3 Y_3 Z_3]to define junction section variables and to perform extrusion from boundary delimiting the bottom of D_{m_j} domain (whose section in plane x-z is colored in pink). A generic β_j is represented

The definition of the compontents f_x, f_y, f_z here (in analogy with the axon hillock considerations just made) is:

$$\begin{cases} f_x = cos(\pi + \beta_j - \gamma_r) \\ f_z = sin(\pi + \beta_j - \gamma_r) \cdot cos(\vartheta_c) \\ f_y = sin(\pi + \beta_j - \gamma_r) \cdot sin(\vartheta_c) \end{cases} \tag{39}$$

while β_j is defined as:

$$\beta_j = \begin{cases} a\tan 2(z_3, x_3) & \text{if } z_3 \neq 0 \\ 0 & \text{if } z_3 = 0 \end{cases} \tag{40}$$

In the end, it is necessary to explain that since in literature, over the axon hillock, Na and K channels are reported to have spatial density typically ten times higher than in the other sections of the neuron

membrane, new constants G'_{Namax} and G'_{Kmax} have been introduced, scaled by this factor.

Finally, membrane domain meshing has been selectively refined in the zones where the Delaunay algorithm had not still massed a sufficient amount of tetrahedra to assure the solver a sufficiently low spatial gradient for variables to solve for, between the vertexes belonging to each one of them (this was particularly true for parameters defined over membrane, especially in correspondence with soma and junction domains). Finally, we recall that axon segment settings are exactly those reported in §3.3.1.

Table 12 reports the extrusion settings for all the sections of the membrane domain, implemented as previously done in order to define TMV, V_m, within the membrane domain D_m.

Table 12 Extrusion implemented for the membrane sections.

Soma (D_{m_s})	
Source Transformation	**Destination Transformation**
$\begin{cases} X_{src} = S_x(x,y,z) = \varphi_s \\ Y_{src} = S_y(x,y,z) = \theta_s \end{cases}$	$\begin{cases} X_{dest} = D_x(x,y,z) = \varphi_s \\ Y_{dest} = D_y(x,y,z) = \theta_s \end{cases}$
$V_o(\theta_s,\varphi_s) = V(\theta_s,\varphi_s)\big\|_{r=r_2}$ → Extruded Variable: $V_o(\theta_s,\phi_s) = V(\theta_s,\phi_s)\big\|_{r\in[r_1,r_2]}$ $V_i(\theta_s,\phi_s) = V(\theta_s,\phi_s)\big\|_{r=r_1}$ → Extruded Variable: $V_i(\theta_s,\phi_s) = V(\theta_s,\phi_s)\big\|_{r\in[r_1,r_2]}$	
Axon Hillock (D_{m_ah})	
Source Transformation	**Destination Transformation**
$\begin{cases} X_{src} = S_x(x,y,z) = x_2 \\ Y_{src} = S_y(x,y,z) = \theta_c \end{cases}$	$\begin{cases} X_{dest} = D_x(x,y,z) = x_2 \\ Y_{dest} = D_y(x,y,z) = \theta_c \end{cases}$
$V_o(x_2,\theta_c) = V(x_2,\theta_c)\big\|_{z_2=z_{22}}$ → Extruded Variable: $V_o(x_2,\theta_c) = V(x_2,\theta_c)\big\|_{z\in[z_{21},z_{22}]}$	

$V_o(x_2,\theta_c) = V(x_2,\theta_c)\big|_{z_2 = z_{21}}$ → Extruded Variable:

$V_o(x_2,\theta_c) = V(x_2,\theta_c)\big|_{z \in [z_{21}, z_{22}]}$

Junction section

Source Transformation	**Destination Transformation**
$\{X_{src} = S\ (x,y,z) = \theta_c$ for V_o	$\{X_{dest} = D(x,y,z) = \theta_c$
$\begin{cases} X_{src} = S_x(x,y,z) = \theta_c \\ Y_{src} = S_y(x,y,z) = \beta_j \end{cases}$ for V_i	$\begin{cases} X_{dest} = D_x(x,y,z) = \theta_c \\ Y_{dest} = D_y(x,y,z) = \beta_j \end{cases}$

$V_o(\theta_c) = V(\theta_c)\big|_{@(Pa,Pb,Pc)}$ → Extruded Variable:

$V_o(\theta_c) = V(\theta_c)\big|_{\text{over Dm\_j}}$

$V_i(\theta_c,\beta_j) = V(\theta_c,\beta_j)\big|_{\partial m_i}$ → Extruded Variable:

$V_i(\theta_c,\beta_j) = V(\theta_c,\beta_j)\big|_{\text{over Dm\_j}}$

Axon extrusion transformation has been already reported in Table 9.

3.3.2.3 Simulation results: AP elicitation and propagation simulation with the moving active zone for the model with soma.

Exactly following the same philosophy we have adopted to test 2D and 3D axon model we, now, proceed in the description of only some of the simulations results obtained stressing the model with a triangular waveform under and overthreshold.

Boundary conditions resemble very closely those of the single axon, as they are synthetically reported in Table 13.

Table 13 Boundary conditions assignments for the model depicted in Fig. 29

Boundary	**Imposed condition**
Bottom of the external box	Ground
Upper and later boundaries of the external box	Electrical insulation
Inner lateral surface of D_m	Current source: $\overline{\boldsymbol{J}}_{source} = \hat{\boldsymbol{r}} J_{sta}$
Circular upper base of the nanoelectrode	Electric potential: $V_{input}(t)$
Other inner boundaries	Continuity of the normal component of current density

Over the boundaries delimiting D_m, for the activation variables, the Neumann condition is set, fixing to zero the their normal derivative.

Let us consider the first stimulation case: an absolute value of the slope and a peak amplitude of the symmetrical triangular voltage input are respectively 35V/s and -35mV, Fig. 33 and Fig. 34 show the expected response of the examined structure of the cell.

Instead, with a greater absolute value of the input voltage slope, 200V/s and a peak amplitude of -80mV the results are depicted in Fig. 35 and Fig. 36. It is remarkable to note that the proximity of the nanoelectrode to the axon hillock “helps” the activation of APs and thus facilitates the neural stimulation with respect to the zones far from the soma along the axon.

Also propagative phenomenon is observed as in the 2D case and in axon segment stimulation (see Fig. 37).

Moreover, when the input signal amplitude is too high, the so-called *potential block* occurs as it can be inferred by our simulation results Fig. 38 in full accordance with literature foreseen behaviour as reported in Fig. 39.

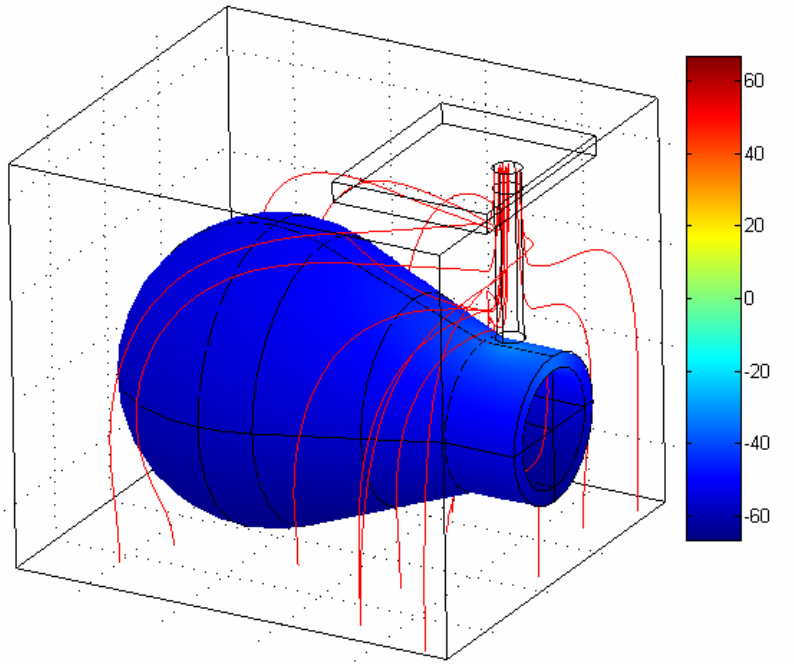

Fig. 33 Understhreshold expected behaviour V_m[mV]. No active zone

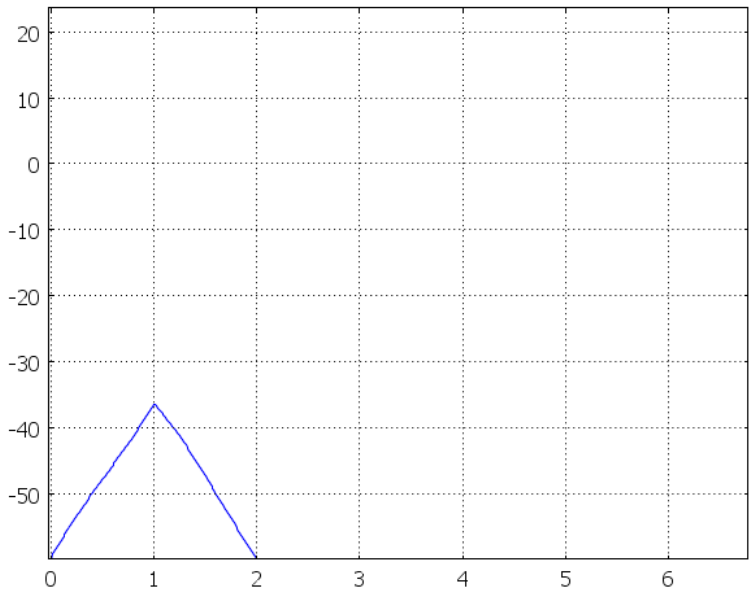

Fig. 34 $V_m(t)$[mV] vs t[ms].Underthreshold correct behaviour.

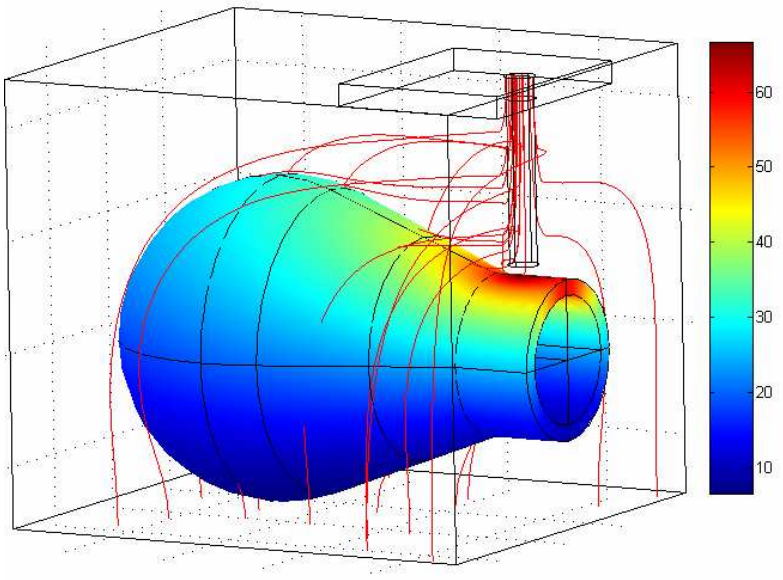

Fig. 35 Overthreshold behaviour. Colormap: V_m [mV]. Red fluxes lines : current density

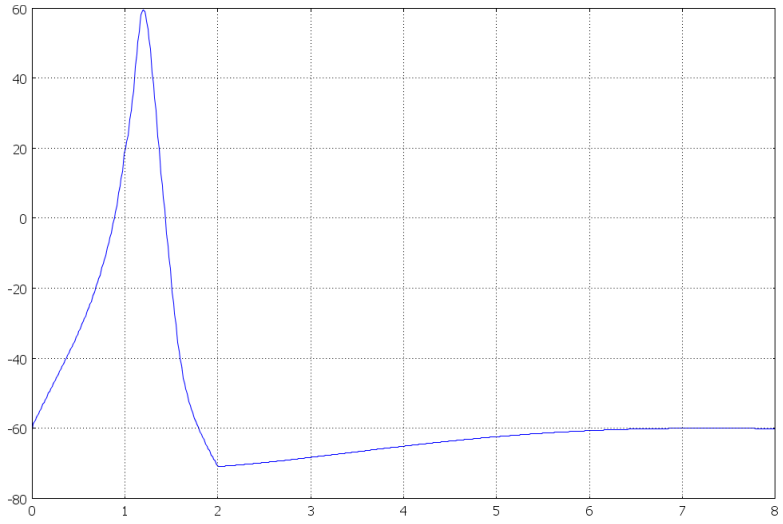

Fig. 36 Transmembrane voltage Vm(t) [mV], t[ms]

a)

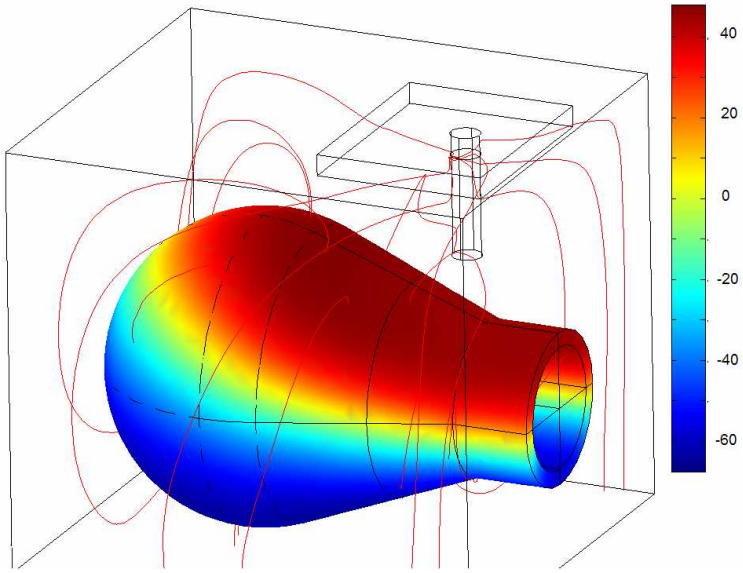

b)

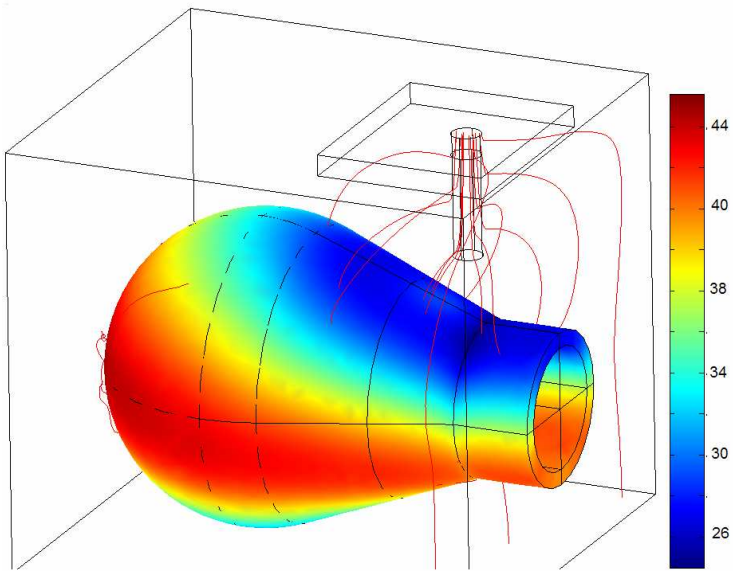

Fig. 37 Propagative effect: colormap of TMV [mV] at a) t=1ms and b) t=1.5ms

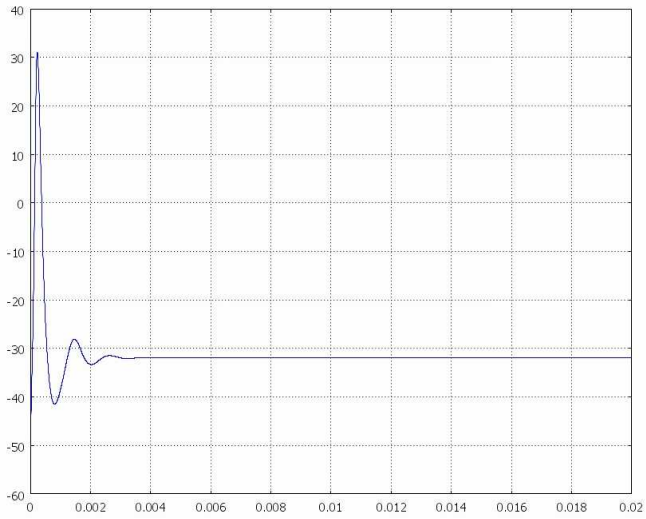

Fig. 38 Very narrow AP (V_m[mV] vs t[s]) elicitation due to a triangular waveform. As expected when the stimulus is very strong a block of the action potential generation occurs

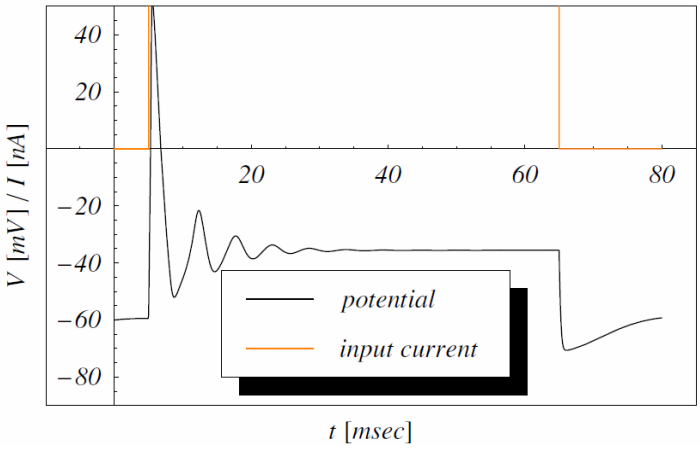

Fig. 39 Figure extracted from [46]

3.3.3 Thin layer approximation in 3D whole neuron modelling

Analogously to what we have done in the 2D case, here we have adopted thin layer approximation, in order to reduce the computational burden and memory consumption of the simulations . This proves to be particularly useful now that we work in a three-dimensional case and 3D FEM models are particularly expensive in terms of resources drain. Indeed, we have implemented the model with membrane in order to have the possibility to compare this approximated one and contrast them in 3D case as we have already done and shown for the 2D. Here memory request and time consumption are greatly reduced by substituting the membrane domain with the already mentioned (§ 3.2.3) mathematical condition accounting for the jump in voltage at the boundary surface. The current density J_{eq} adopted in this case is set all over the discontinuity surface separating inner and external medium; thus V_2 is the dependent variable within the inner medium and V_1 is defined in the external medium. J_{eq} is defined according with (41)

$$J_{eq} = \sigma_m \frac{(V_2 - V_1)}{d_m} + J_e + \frac{\varepsilon_m \varepsilon_0}{d_m} \frac{\partial (V_2 - V_1)}{\partial t} \tag{41}$$

All variables definition is made according to HH model equations as defined in §3.2.2.

Moreover, the use of the two Electro Quasi Static system of equations has been adopted (as previously done) in conjunction with the PDE model for the definition of the channel activation variables.
Although apparently this could look like the straightforwardly easiest modelling task achieved, some implementation troubles have come forth(as in the 3D case for the model with soma and axon hillock etc.), even if its implementation has required certainly a considerable inferior amount of time.

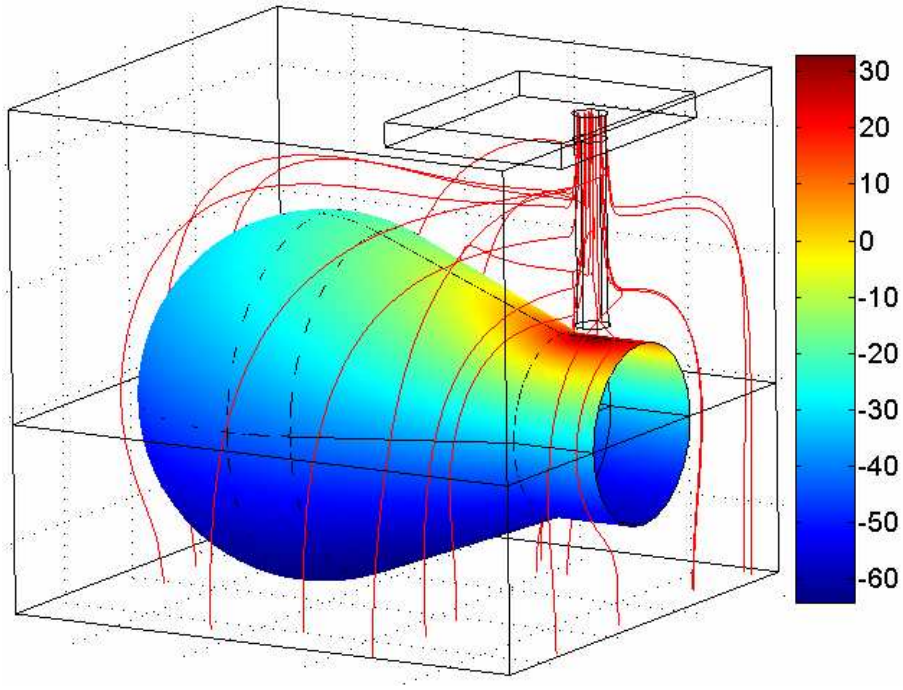

Fig. 40 Overthreshold behaviour. Colormap TMV [mV]. Input stress: symmetric triangular waveform (peak amplitude -100mV, absolute value of slope 200V/s)

3.3.4 Comparison between models implementing membrane domain and those exploiting the Thin Layer Approximation in 3D

This paragraph shows the numerical simulation advantages in the Thin Layer Approximation modelling solution in 3D, with respect to the previously analysed whole model (with membrane). Once defined MODEL1, the one implementing the membrane domain and MODEL2, the thin layer approximated, we can compare their performances in terms of namely a chosen (an relevant) model output variable. In this case we have realized the comparison observing the TMV in an assigned reference point of the structure (2.88μm,0,0.72μm). To be fair the same FEM element type (Lagrange, quadratic) relative tolerance (10^{-4}) and absolute tolerance (10^{-8}), the same time vector ([$0:8\cdot10^{-6}:2\cdot10^{-3}$]) and even the same type

of solver have been employed as well as the same stimulating conditions in terms of relative positioning of the cell and the nanoelectrode and in terms of input signal absolute slope, 200V/s, and peak amplitude, 100mV, of a real voltage step.
The measured root mean square error amounts to approximately 4mV, which shows that MODEL2 is a really good approximation of the simulated structure, also because only in a very few points of the simulation time vector there is a certain relative difference between the two models predictions, while a very conspicuous decrease in DoF to solve for, elements of the mesh and as a consequence in memory and time consumption, as well as in terms of employment possibility of the MODEL2 in possible serial parametric analysis.Table 14 synthesizes the comparison terms.

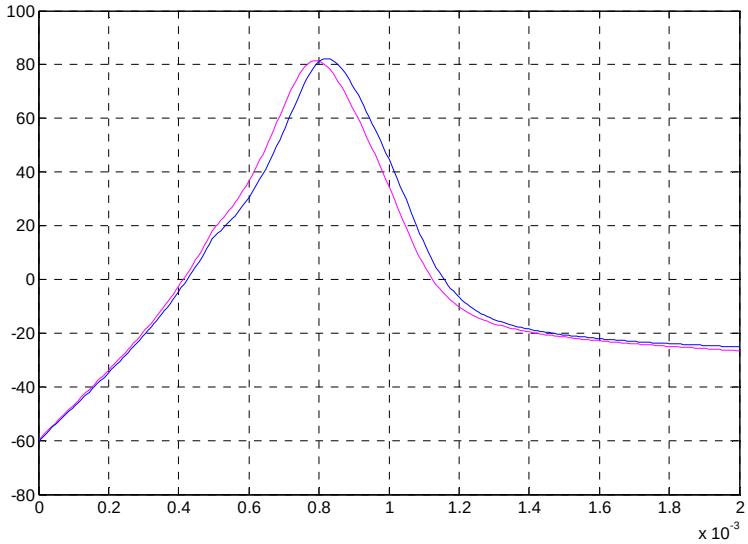

Fig. 41 Comparison between the two different TMVs Vm1(t) and Vm2(t) [mV] vs t[s] (@ point of coordinates (2.88μm,0,0.72μm). simulated with MODEL1 (with membrane- magenta) and MODEL2 (with thin layer approximation-blue)

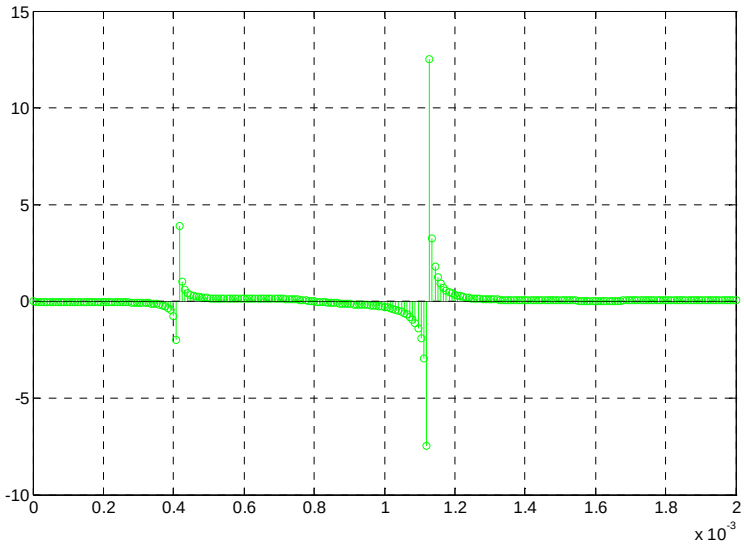

Fig. 42 Relative error of the V_m [mV] vs t[s]: only in a very few points there is a significant difference between the the two models predictions, thus leading to an RMSE of almost 4mV

Table 14 Comparison of the MODEL1 with MODEL2. Main simulation parameters (Overthreshold stimulation).

Parameter	**MODEL1**	**MODEL2**
Simulation duration [s]	3815	1243
Number of Degrees of Freedom	67720	38703
Number of mesh points	5752	4448
Number of elements	30682	22834
Number of tetrahedra	30682	22834
Number of boundary faces	6625	4524
Number of triangular boundary faces	6625	4524
Number of boundary quadrilateral faces	0	0
Number of edges elements	798	480
Number of vertex elements	83	50

A second comparison in arranged in exactly the same conditions except for the stimulation which is set to a an underthreshold real step (absolute slope 20V/s and peak amplitude -40mV).

Table 15 Comparison of the MODEL1 with MODEL2. Main simulation parameters. (Underthreshold stimulation)

Parameter	**MODEL1**	**MODEL2**
Simulation duration [s]	2800	658

The reduction in the time spent in simulating is thus of almost one third in the overthreshold case reported in Fig. 41 and in Fig. 42, while in the second underthreshold case the reduction is even more sensible with a rate 1 to 4. Moreover an RMSE in the waveform simulated with MODEL2 of about 1mV is verified and relative error in Vm calculation even gets reduced to less than 0.07.The results are shown in Fig. 43 and Fig. 44 and Table 15.

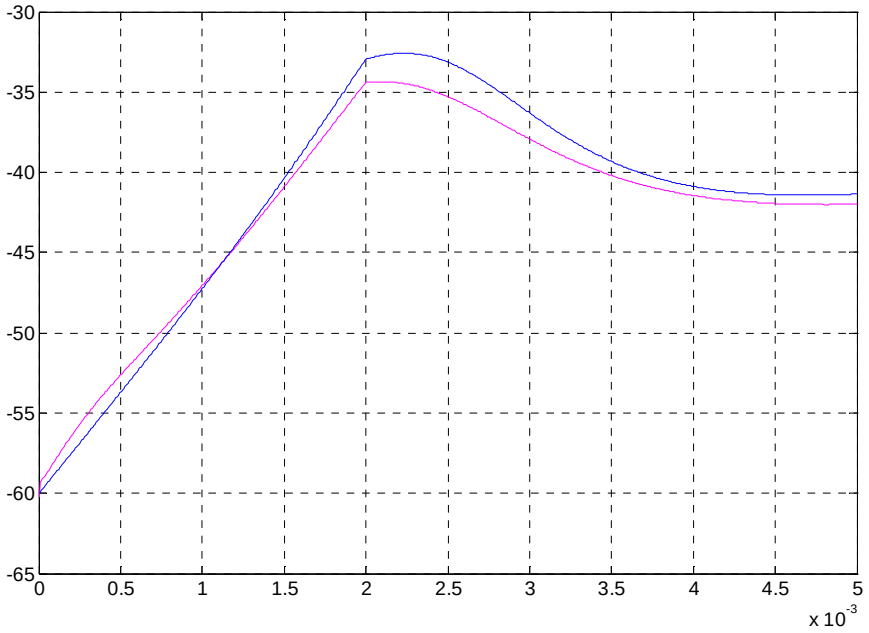

Fig. 43 $V_m(t)$ [mV] vs t[s] according to MODEL1 (magenta) and MODEL2 (blue)

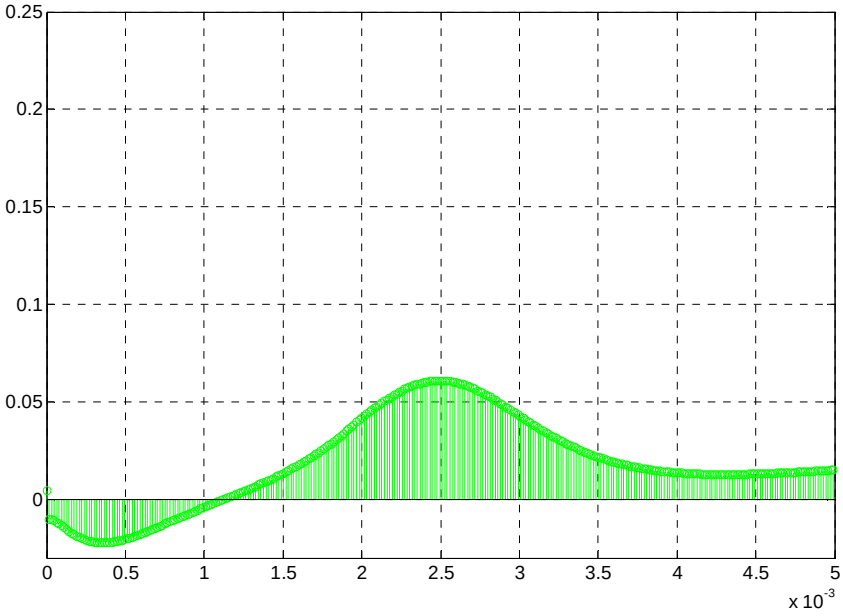

Fig. 44 Relative error on the calculation of $V_m(t)$ vs t[s]

3.4 The selectivity problem: verification of the selective neuron triggering (the biaxonal model).

A new model containing two different axon segments is introduced in this paragraph, purposely to be able to show how a stimulus targeting one axon can invest and then trigger an AP also in neighbour cells structures and eventually how it does not. As we have already described in the introductory part of this thesis work nanoelectrodes (especially CNT- nanoelectrodes) can be seen as the nanotechnology answer to an extremely important issue: the spatial resolution in the functional restoration of sight [3], [58]. Indeed, it is well known in literature that to achieve a minimum required visual acuity of 20/80, is equivalent to assure approximately 2500 pixel (or electrodes units)/mm^2 [58]. Moreover, as we noticed previously *micro*electrodes

(and thus MEA) (even those using the donut-shaped ones, in literature reported as much effective) are very far behind that target, therefore requiring different solutions to enlarge the stimulation effectiveness and quality through elevating its spatial density. In §3.4.1 the brief description of the modelling adaptations necessary for the described equations used to model HH in the axon segment in 3D (see §3.3.1) and its exploitation helps us in showing how at this scale the low voltages that can be employed, facilitate in being effective in selectively triggering APs only across the membrane of the target cell and finally, in increasing the neurostimulation system resolution.

3.4.1 A couple of axons 3D FEM model

In order to obtain the simulations needed to accomplish this, nevertheless a few tiny changes in the modelling bulk had to be performed. Translation of some equations parameters as a function of the distance (Y_A=5μm) between the two centres of the axons had to be performed in the expressions governing the model of a single axon, in order to model the "victim" axon behaviour (in green in Fig. 46). The external current density. $\bar{\boldsymbol{J}}_{\boldsymbol{ext}}$ had to be redefined accordingly (42):

$$\bar{\boldsymbol{J}}_{\boldsymbol{ext}} = \begin{cases} J_e \hat{\boldsymbol{r}} = J_e \cos(\theta_2(y,z))\,\hat{\boldsymbol{x}} + J_e \sin(\theta_2(y,z))\hat{\boldsymbol{y}} & \text{on } \mathrm{D_m} \\ 0 \text{ elsewhere} \end{cases} \tag{42}$$

where J_e is defined as in (16) and θ_2 is:

$$\theta_2(y,\mathrm{z}) = \begin{cases} a\tan 2(z, y - Y_A) \\ \left| a\tan 2(z, y - Y_A) \right| + \pi \end{cases} \tag{43}$$

The fundamental setting of the initial condition for the TMV, *Vm(t),*

$$V_m(t=0): Ar_a + B \tag{44}$$

with

$$r_a = \sqrt{(z^2 + (y - Y_A)^2)} \tag{45}$$

and *A* and *B* defined as in (33).
In the following pictures two different working conditions are simulated: the parallel targeting of the two (one intended and the second at the right, the victim axon) and the second a selective elicitation achieved with different signal parameters. Better and clearer understanding of the dependencies on system factors of the neural activity will be reached in §4.3.3.

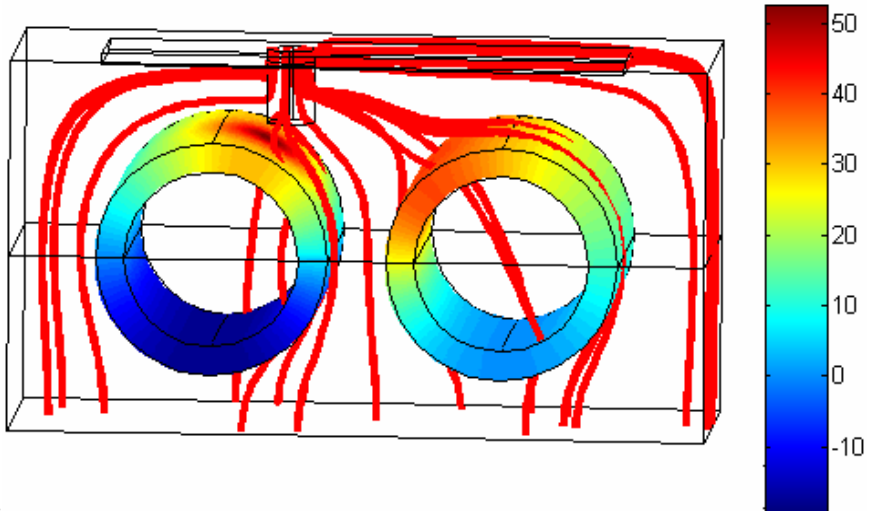

Fig. 45 Ps are triggered on both axons: no selectivity obtained. Color map: Vm [mV]. Fluxes lines in red: current density entering also the second neuron are sufficient to elicit an AP also in the latter

In that section, indeed, interesting conclusions can be drawn on the main factors discriminating the targeted or parallel APs activation for this configuration of neighbor fibers.

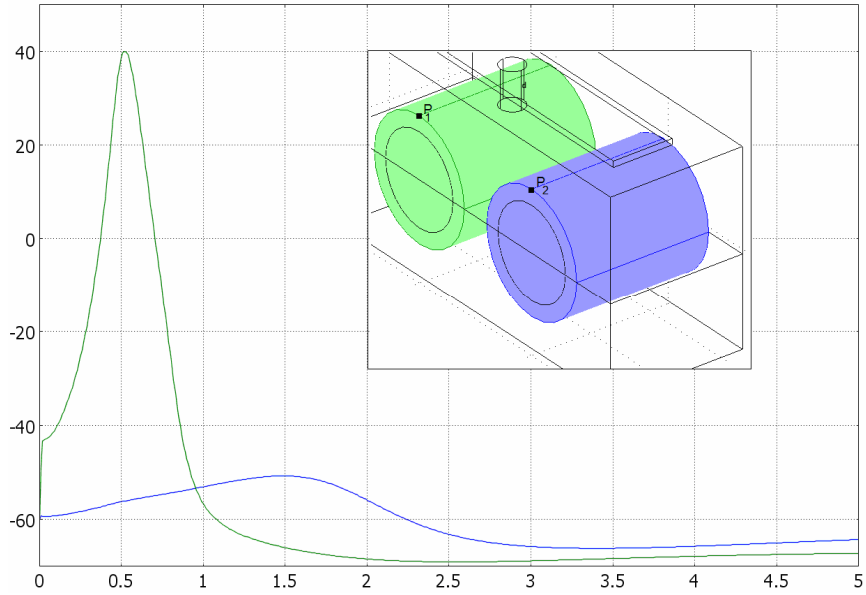

Fig. 46 TMV [mV] vs *t*[ms], evaluated across the membranes of the two axons. V_m(t) in the target cell (green) and in the "victim" cell (blue)

Chapter 4

Performance analysis for Neurostimulation

4.1 Design of Experiment Technique Adoption

Simulation and optimization are nowadays a key success factor for cost effectively and timely development, manufacturing of competitive products and processes. Thus, we have decided to approach the study of our neurostimulation system performances by means of the typical numerical prototyping procedures, based on a sequence of numerical simulations, done in an iterative form (exploiting the previously described FEM models –Chapter 3). In this case, numerical prototyping, is specially focused on the DoE approach, leading to a substantial reduction of numerical experiments [59],[60].

Numerical prototyping methods rely on a sequence of uncorrelated simulations and follow up procedures.

There are basic steps typically performed. First of all, the capture of the simulation sequence necessary to be able to simulate the desired design attribute. In our case, it can be identified with stress simulation main characteristics, in terms of signal time evolutions, geometrical parameters and positioning of the nanoelectrode with respect to the target system (a single axon segment, a couple axons or a complex of soma, axon hillock and initial axon segment). This procedure proves to be effective, because typically in literature design attributes are taken into account not in a systematic overall perspective, thus loosing the global effectiveness and validity of the approach sight. Furthermore, it often happens that simulation sequences are derived by hand on the basis of orally handed down

among experts.

The next step is the exploitation of the DoE (Design of Experiments) technique, in order to scatter the simulations in the region of interest, according to the chosen scheme, e.g. orthogonal, random and so on. The last step in the procedure is the RSM (response surface methodology), allowing the interpolation/approximation of the response, using a mathematical model.

It must be also said that, besides the advantages (well documented in the literature) [59], there are some drawbacks hidden in any numerical prototyping based on the above summarized procedures. The primary ones are: the ability to automate capturing and organization of the necessary simulation sequences, secondly the efficiency, due to the required number of simulations, which in turn grows exponentially with the number of input factors (variables) and last but not the least the quality, due to the reliability or credibility of the response model, which can be in turn used for introducing an optimization procedure. The first is a limiting factor since the engineer needs to perform a lot of error tedious and time consuming manual work. Furthermore, most often the engineer faces the decision on a compromise because it seems unrealistict to improve the quality of the response model and at the same time to reduce the number of tests in the chosen experiment.

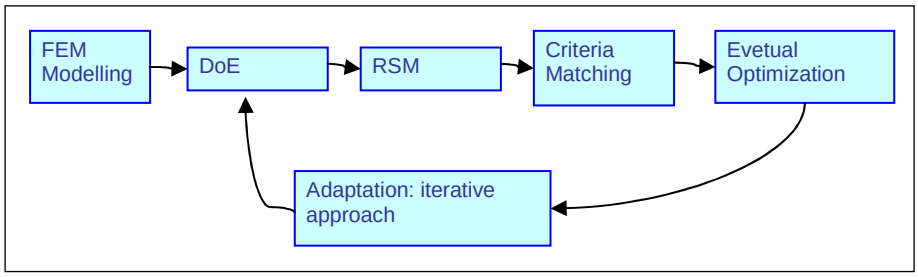

Fig. 47 Schematic diagram of an elaborated advanced numerical prototyping algorithm [59].

The scheme of the well known method we are applying in this particular context of the neurostimulation is presented in Fig. 47 and it can be summarized by the following steps. Building up numerical FEM models-of a product or process capturing the physics of the problem. Automating the design process, also realizing a screening

experiment based on orthogonal DoE scheme procedure to discover the correlation binding the response and input factors (thus interactions are included) and eventually defining their meaningfulness in terms of mean, variance or median, selecting the most essential or significant input factors and adding additional experiment tests according to (e.g.) a Latin Hypercube design scheme. Then interpolating the initial RSM model of the response in a form capable of reflecting relationships between the response and the most significant factors. In the end, if necessary, implementing the iterative approach in order to improve the final model of the response by sequential adding additional experiment points basing on the estimation of the interpolation error.

4.1.1 Some details for Design of Experiments (DoE)

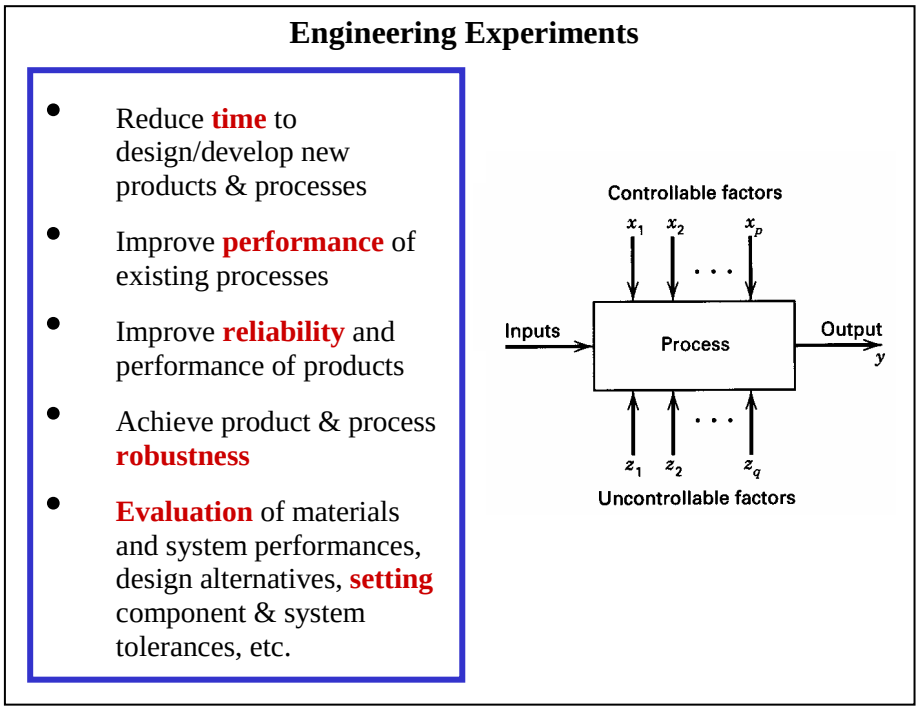

Fig. 48 A schematic representation of experiments main features and applications for the DoE technique [60]

Experiments are performed by investigators in virtually all fields of inquiry, usually to discover something about a particular process or system. Literally, an experiment is a *test***.** More formally, we can define an *experiment* as a test or series of tests, in which purposeful changes are made to the input variables of a process or system so that we may observe and identify the reasons for changes that may be observed in the output response. It is always of paramount importance to wonder whether:

-the chosen parameters represent the only factors of potential interest to be controlled within the experiment context ,

- which are the possible methods to elaborate data and analyze them,

- in which order data must be collected and organized during the analysis,

-what difference in average observed output data between different parameters must be considered important etc.

This is why, in some critical and complex situations , it is clear that a scientific approach to planning the experiment is to be employed, instead of an non automated one. *Statistical design of experiments* refers to the process of planning the experiment so that appropriate data that can be analyzed by statistical methods will be collected, resulting in valid and objective conclusions. The statistical approach to experimental design is necessary if we wish to draw meaningful conclusions from the data. DoE steps include: 1. statement of the problem. 2. Choice of factors, levels, and ranges 3. Selection of the response variable. 4. Choice of experimental design.5. Performing the experiment. 6. Statistical analysis of the data. 7. Conclusions to draw.

Some useful classifications are design factors, heldconstant factors, and allowed-to-vary factors. The design factors are the those actually selected for study in the experiment. Held-constant factors are variables that may exert some effect on the response, but that, for purposes of the present experiment, are not of interest, so they will be held at a specific level. The potential design factors are those the experimenter may wish to vary in the experiment.

Once the experimenter has selected the design factors, he must choose the ranges over which these factors will be varied, and the specific levels at which runs will be made. Thought must also be given to how these factors are to be controlled at the desired values

and how they are to be measured, when dealing with physically implemented experiments.
This process knowledge is usually a combination of practical experience and theoretical understanding. It is important to investigate all factors that may be of importance and not to be overly influenced by past experience, particularly when we are in the early stages of experimentation or when the process is not very mature. When the objective of the experiment is factor screening or process characterization, it is usually best to keep the number of factor levels low. Generally, two levels work very well in factor screening studies.
The selection of the response variable is oriented to provide useful information about the process under study. Statistical methods could be used to analyze the data so that results and conclusions are objective rather than judgmental in nature. It is also usually very helpful to present the results of many experiments in terms of an *empirical model*, that is, an equation derived from the data that expresses the relationship between the response and the important design factors. Moreover, it must be taken into account that statistical methods cannot prove that a factor (or factors) has a particular effect. They only provide guidelines as to the reliability and validity of results. The primary advantage of statistical methods is that they add objectivity to the decision-making process. Statistical techniques coupled with good engineering or process knowledge and common sense will usually lead to sound conclusions. Once data have been collected conclusions can be drawn Moreover, throughout this entire process, it is important to keep in mind that experimentation is an important part of the learning process, where we tentatively formulate hypotheses about a system, perform experiments to investigate these hypotheses, and on the basis of the results formulate new hypotheses, and so on. This suggests that experimentation is iterative. As an experimental program progresses, we often drop some input variables, add others, change the region of exploration for some factors, or add new response variables.

Once delineated this scenario, we must say that our initial approach, in the stimulation system analysis considered, is, as theoretically prescribed in literature, a 2^k full factorial design approach. Factorial designs are widely used in experiments involving several factors where it is necessary to study the joint effect of the

factors on a response.. However, there are several special cases of the general factorial design that are important because they are widely used in research work and also because they form the basis of other designs of considerable practical value. The most important thing of this special study is that each of the *k* factors assume only two levels. A complete replicate of such a design requires $2\times2\times2. \ . \ . \times2=2^k$ observations and is called a *factorial design*. The 2^k design is particularly useful in the early stages of experimental work, when there are likely to be many factors to be investigated. It provides the smallest number of runs with which k factors can be studied in a complete factorial design. Consequently, these designs are widely used *in factor screening experiments*. Because there are only two levels for each factor, we assume that the response is approximately linear over the range of the factor levels chosen. In many factor screening experiments, when we are just starting to study the process or system, this is often reasonable .

A potential concern in the use of two-level factorial designs is the assumption of *linearity* in the factor effects. Of course, perfect linearity is unnecessary, and the 2^k system will work quite well even when the linearity assumption holds only very approximately. In fact, if *interaction terms* are added to a main effects or first-order model, we have a model capable of representing some curvature in the response function. This curvature, of course, results from the twisting of the plane induced by the interaction terms $\beta_{ij}x_ix_j$**.** There are going to be situations where the curvature in the response function is not adequately modelled by eq (46).

$$y = \beta_0 + \sum_{j=1}^{k} \beta_j x_j + \sum\sum_{i<j} \beta_{ij} x_i x_j + \varepsilon \qquad (46)$$

In such cases, a logical model to consider is where the β_{jj} represent pure second-order or *quadratic effects***.** Equation (47) is called a *second-order response surface model.*

$$y = \beta_0 + \sum_{j=1}^{k} \beta_j x_j + \sum\sum_{i<j} \beta_{ij} x_i x_j + \sum_{i=1}^{k} \beta_{jj} x_j^2 + \varepsilon \qquad (47)$$

There are also some extensions and variations of these designs that are occasionally useful, such as the designs for cases where all the factors are present at three levels: the3^k *factorial design*

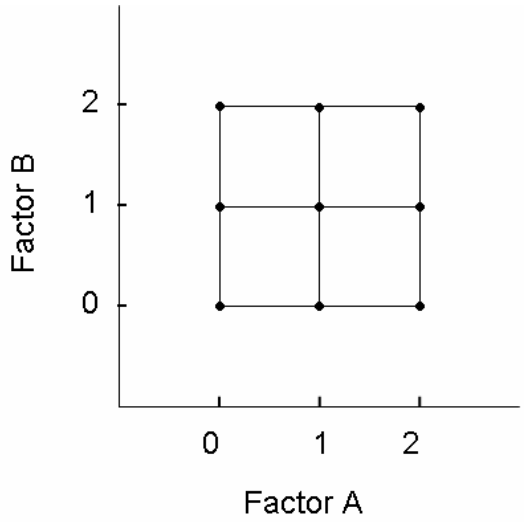

Fig. 49 Notation for the 3^k Design

In the 3^k system of designs**,** we often denote the low, intermediate, and high levels by -1, 0, and +1, respectively. This facilitates fitting a *regression model* relating the response to the factor levels. For example, consider the 3^k design, and let x, represent factor A and x^2 represent factor B. A regression model relating the response y to x_1 and x_2 that is supported by this design is:

$$y = \beta_0 + \beta_1 x_1 + \beta_2 x_2 + \beta_{12} x_1 x_2 + \beta_{11} x_1^2 + \beta_{22} x_2^2 + \varepsilon \qquad (48)$$

Notice that the addition of a third factor level allows the relationship between the response and the design factors to be modelled as a quadratic. The 3^k design is certainly a possible choice by an experimenter who is concerned about curvature in the response function.

All is based on the idea that it can be useful to fit a *response curve* to the levels of a quantitative factor obtained so that the

experimenter has an *equation* that relates the response to the factor. This equation might be used for interpolation, that is, for predicting the response at factor levels between those actually used in the experiment. When at least two factors are quantitative, we can fit a *response surface* for predicting the function at various combinations of the design factors. In general, *linear regression methods* are used to fit these models to the experimental. The method of least squares is typically used to estimate the regression coefficients in a multiple linear regression model.

4.2 Sensitivity Analysis on the neural membrane main electrophysiology: DoE investigations

4.2.1 Analysis of Simulations Results

This section is devoted to the description of the "experiments" we have chosen to conduce, exploiting the DoE theory in order to achieve a better understanding of some of the main features of neuron membrane active behaviour. The objective is to determine the extent of sensitivity of the different modelled configurations to some chosen input controllable parameters and /or to discover the best operating conditions for the elicitation of the AP, by observing the effect that some of these factors produce on the TMV.

The first analysis we have conduced is dedicated to the prediction of the AP triggering and its speed, once an appropriate search is conduced of suitable parameters ranges. It could be useful when a constraint on a particularly high frequency of bursting (several APs per unit of time) is needed to code optical information.

The second exploits our axon segment model to investigate quantitative dependence of the AP spike duration (similarly to what we have done for the 2D case, but in a more systematic way) on the operating temperature.

The third and the fourth analysis, that we have conduced,

investigate the sensitivity of TMV peak value to variations in the same parameters of the stimulation apparatus and in the practical case adopted for the first analysis. In particular we investigate neurostimulation effects, when it is performed along the axon and in proximity with the soma, axon hillock and axon initial segment zones.

Then another experiment is considered, aiming at studying the influence of the cited controllable design parameters on the possibility to selectively elicit APs, by focusing on one rather than another close axon.

4.3.1 Analysis on a single axon segment

4.3.1.1 Analysis of the system promptness dependence on stress input parameters with linear regression

Before going though the summarized description of the design phases carried out to perform our experiments devoted to determine the most relevant factors for the PFs, a clarification must be made.

All the analysis we have implemented on the realized models aim at furnishing a (though partial) helpful background pre-information on the effectiveness of certain types of nanoelectrodes simulations on neurons, with respect to certain others. Then, we remind that our particular interest is cast on retina ganglion cells performances under neuroprosthetic devices and that we are imaging of modelling the effects of an neurostimulating system which is a tiny constitutive part of a much greater apparatus (NEA). It must be said that its positioning and fixing, in particular, is constrained by the eyes anatomy (the distance of the retinal ganglion cells to the internal limiting membrane). Nevertheless, with nanotechnology, it is possible to arrive nearer to the target zone with respect to what was possible until few years ago. Thus, instead of considering an electrode-target tissue distance within the range of tens of microns, we can imagine to build a support layer sufficiently thick as to bring nanoelectrode more precisely and more closer to the target. This could be useful since it leads to a reduction in the signal strength necessary to elicit APs in ganglion cells (which are our target), in turn, reducing the probability of the observed focal phosphenes (spot of light) in patients with retinal prosthetics .

It is, indeed, possible that also other retinal cells (apart from the target ganglion ones) are excited by electrical stimulation even though ganglion cells are physically closer to the electrodes. This is particularly true for massive and invasive action of microelectrodes as opposed to the possibly softer one of nanoelectrodes.

In particular, this is due, for example, to much lower activation thresholds (5μV) of retina photoreceptors paving the outermost layer of the eye from the back (as cited in Chapter 2).

As a matter of fact, within this context they are victim and, thus unwanted, targets, perceiving the stimulus aimed at the ganglion axons of the innermost layer and triggering the spots of light cited.

If photoreceptor or bipolar cells are easier to electrically stimulate, they tend to give focal responses since their processes and receptive fields have limited spread in areas outside the fovea.

In addition to this, as we said in Chapter 2, there are more photoreceptors than bipolar cells and more bipolar than ganglion cells. Thus, a greater number of deeper cells (photoreceptors or bipolar) might be stimulated compared to the number of superficial cells, if the stimulus manages to affect all layers approximately equally [3].

Once made all this necessary practical considerations, it is clear that nanolectrode *designable* most prominent parameters (at least for the knowledge in this initial phase of the experiments) can be identified with in its diameter, its transversal positioning with respect to the axon symmetry axis and with in its length. For the last two, in particular, it must also be evidenced that there are still technologic controllability troubles.

We still cannot know precisely in a NEA where the axon falls with respect to its nearest electrode (problem of reachability and as a consequence of selectivity: §4.3.3 too) and, for the second one, it is still difficult to exactly predict its produced value when the nanoelectrode is made up of one ore more CNTs (nanofibres) because of well known nanoscale technical production precision limitations. Thus, (this applies especially for the first one) these two parameters are only partially under the designer control, leading to an uncertain operating conditions, that can surely benefit from the systematic sensitivity analysis we have set up.

In this particular section, we first focus on the elicitation of the AP and then on its readiness. Since we needed to select our Performance

Function (PF), we have chosen to estimate it by observing the instant, be it t_{th}, when the axon membrane TMV crosses the time axis (Fig. 50), as a function of the main (signal and geometrical) input stress parameters.

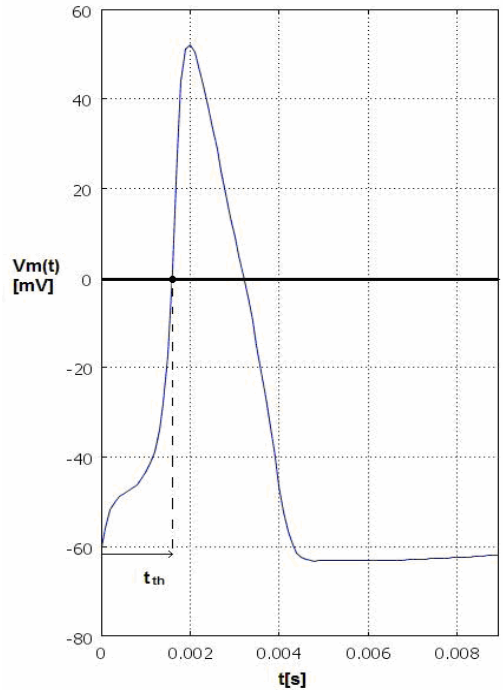

Fig. 50 Definition of t_{th}

Here the axon segment stimulation is performed in the same way reported in § 3.3.1, applying a voltage signal $V_{in}(t)$ to the nanoelectrode upper face.

The waveform considered in this initial approach experiment (in accord with the previously cited iterative and gradually focussing iterative procedure typical of DoE technique) is constituted by a trapezoidal one, whose shape parameters are the absolute value of its rise and fall slope (*S*) (they are set to the same value), its minimum amplitude (*Amp*) -the applied voltage is negative- and its "on" time (*Dur*).

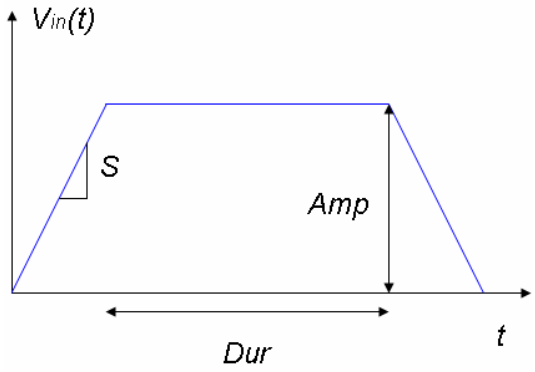

Fig. 51 Time shape of $V_{in}(t)$

Geometrical variable parameters of our model are, instead: the radius of the nanoelectrode (r), its transversal displacement (D_y) with respect to its starting position, which is obviuosly centered on the y-axis and, in the end, its length (l_n) leading also to a univocal definition of d (parameter more frequently found in literature and, for this reason, to which in this context we refer) as in Fig. 52. In particular the latter is defined as the distance from the base of nanoelectrode to the tangent plane at the uppermost point of the axon in section y-z, as reported in Fig. 52.

The number of variable parameters considered is thus 6, therefore, choosing a 2^k DoE scheme we needed to run 64 (2^6) simulations varying one-factor-a-time.

In order to set up an efficient and meaningfully predictive model choice of the starting ranges for parameters is fundamental.
The firstly chosen are trial ones and are reported in Table 16, they obviously take into account the general pre-information acquired studying literature on this topic.

In particular the choice of the “on” time for the waveform in not dictated by the values typically used in literature, because it is by far larger than tens of μs usually adopted, but by our desire to experiment whether (with the adopted ranges of the other parameters and especially for the adopted value of temperature) it is was really little influent or not on the activation of the AP.

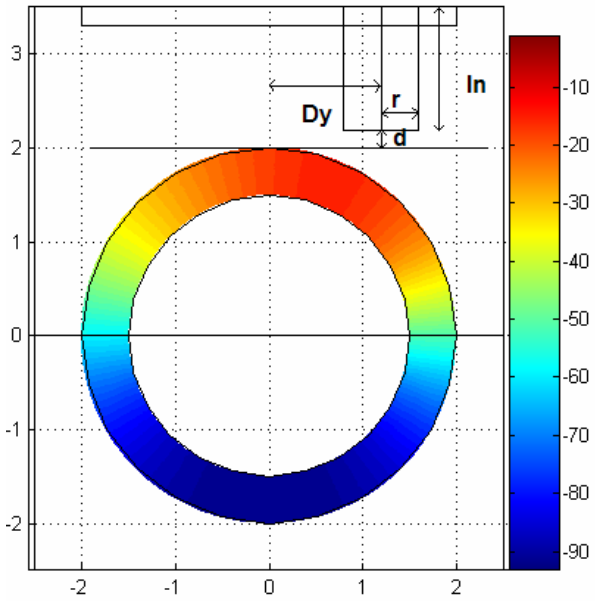

Fig. 52 Plane y-z: a simulated particular stimulation condition for the geometrical parameters, reproduced as an example to graphically represent D_y, r and l_n and d(axis values are expressed in μm)

Table 16 Adopted ranges for first trial DoE iteration

Parameter	**Adopted range**
S	[20,200]V/s
Amp	[-100mV,-40mV]
Dur	[0,14ms]
r	[100nm, 350nm]
d	[100,1100]nm
D_y	[0,1.5μm]

At this point of the work a transformation of COMSOL Multiphysics ® integration with MATLAB environment has proved necessary: MATLAB script code has been generated for defining opportune functions aiming at the systematic management and variation of model parameters as well as comfortable simulations results elaboration. An automatic procedure has, then, been implemented in MATLAB , sampling the space of the parameters and building a

matrix containing all the input n-ples. Once collected all the PF samples calculated by a COMSOL file (the cited function) implemented in MATLAB interface, the vector of the output values have been exploited with the objective of determining a fitting linear model for the time APs start as a function of the reported variable parameters.

First of all, analyzing simulations results, we must precise that since our ranges were trial ones, we have realized that not every parameter combination led to an AP elicitation, thus posing the problem of the definition of the t_{th} in this cases.

We can deduce from this that, since it is not intrinsically meaningful to try to obtain a regression model for a variable which can be also non-existing for some parameters combinations, we look for ranges leading to assured AP triggering: making evaluations on the data obtained where all the unfeasible n-ples are crossed out would bias our main factor inferring. To understand this, we can fix our attention on a single parameter and we can suppose that there can be some combinations of the remaining variables leading to the birth of APs for its maximum value but not for the minimum one. Thus, ignoring the (n-1)-ples with the same combinations (as far as all the other variables are concerned) and keeping the one corresponding to this parameter maximum, unfairly biases our estimation of the "strength" of its effect, being one output uncomparable with the corresponding one.

We have thus, decided to exploit these 2^k simulations (always in accordance with the prescription of DoE which invites to derive the maximum information on each feature or response of the system under analysis), *only* in order to estimate their effect on the activation of the AP. In addition to this we have decided to search other ranges to obtain a certain triggering, also on the basis of this analysis .

It must also be pointed out that all considered parameters have a certain amount of effectiveness on the activation or missed activation of the AP, nevertheless none of them is really crucial for the on-off phenomenon of the threshold crossing of the TMV. This can be seen, because passing from the minimum to the maximum of all the variables there is no concentration of the PF samples on activation or not (in Dex scatter plot of Fig. 53 we refer to a discrete variable defined on purpose assuming a value equal to 1 if the AP has started

and 0 if not). We have chosen to represent our results by Dex scatter plots because it is the primary data analysis tool for determining if and how a response relates to another factor. Determining if such a relationship exists is a necessary first step in converting statistical association to possible engineering cause-and-effect. From such a foundational plot, the analyst invariably extracts information dealing with location shifts, variation shifts, and outliers. Such information may easily be washed out by other "more advanced" quantitative or graphical procedures (computing and plotting means), hence there is motivation for the Dex scatter plot. If we were interested in assessing the importance of a single factor, and since "important" by default means shift in location, then the simple scatter plot is an ideal tool. A large shift (with little data overlap) in the body of the data from the "-" (minimum parameters values) setting to the "+" setting of a given factor would imply that the factor is important. A small shift (with much overlap) would imply the factor is not important.

In our case also Fig. 54 is used as a means to synthetically and quickly represent the “strength” of each parameter in determining an activation or not. A notation highlight must be done: in all figures reported in the following text the design parameters measurement units are missed for brevity, they are reported in advance in the summary tables. Indeed, out of 64 simulations only 30 APs are triggered, distributed according to the bar diagram reported in Fig. 54. Although they are not sufficient to derive information for the dependence of t_{th} on the variables we can infer from this distribution that within the ranges of chosen parameters D_y is the least important factor in determining whether an AP starts or not (15 APs when it is at its minimum 15 at its maximum), while *Dur* follows (12,18), then comes *r*, *Amp* and *d* have the same weight (10, 20), (20,10) and (20,10) respectively and *S* is the most prominent one (8, 22). Thus, at this stage of our analysis, (although it is only qualitative and it does not give us the opportunity to obtain a regression model for the activation phenomenon (matter that will be further and more deeply investigated in § 4.3.1.4 and in § 4.3.2 with a suitable choice of the PF) we can already deduce that at least as a tendency, the most meaningful parameter is the slope *S* of the waveform (better when higher), afterwards, *r* and *Amp* (better when higher), and *d* (better when lower) and in the end *Dur* (better when higher); *Dy* is indifferent

in the chosen range.

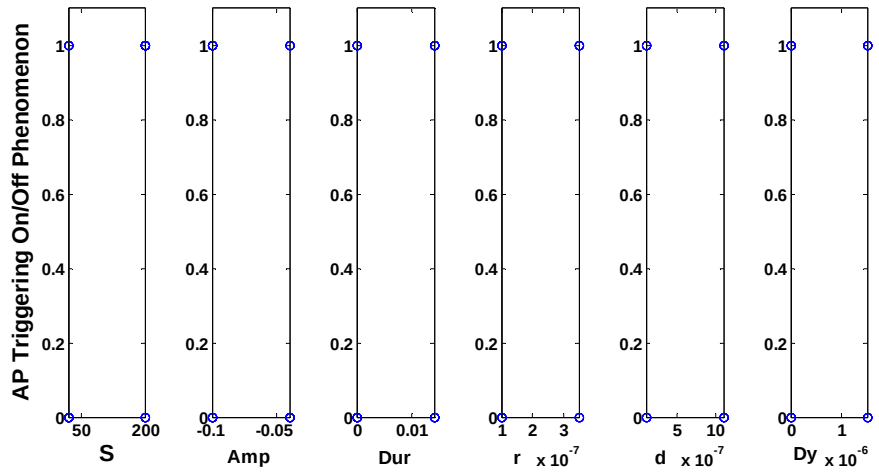

Fig. 53 Dex scatter plot representing PF values when a variable is fixed to its extreme values (minimum and maximum), while the others are free to vary

Now, as far as t_{th} is concerned, we decided to assign new trial ranges (Table 17), obtained following the hints dictated by the results just gained: we have extended the investigation ranges, with a particular attention in increasing the lower limit of *S* and *r* and decreasing the upper for *d* and *Amp* (we remind it is a negative value).
Moreover for *Dur* parameter, we have decided to drop it out just because it has low influence even when it is varied on a much wider range than the typical adopted in literature (of the order of μs).

Table 17 New adopted ranges for the second DoE iteration

Parameter	**Adopted range**
S	[120,500]V/s
Amp	[-500,-100] mV
r	[400,700]nm
d	[100nm, 900nm]
D_y	[0,1.2μm]

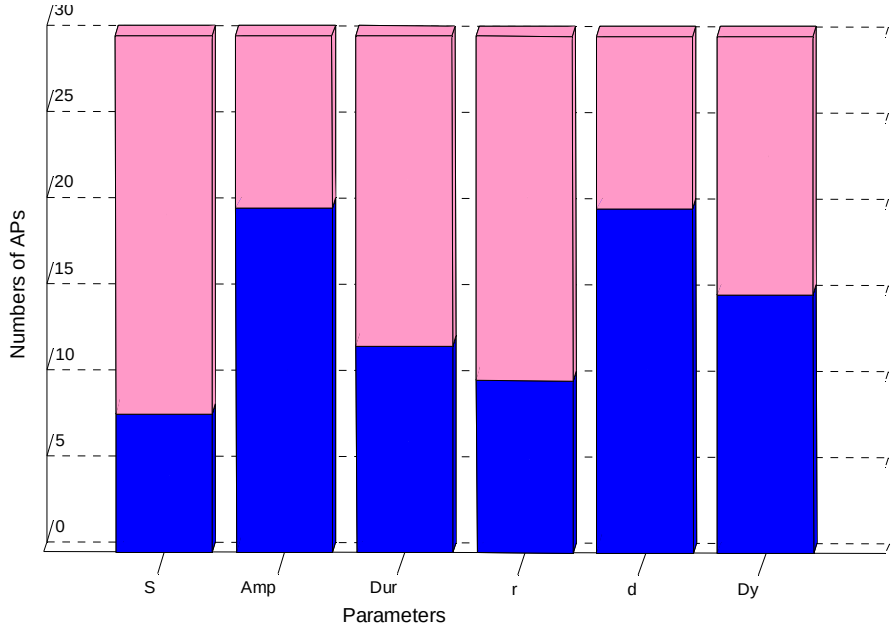

Fig. 54 Number of triggered APs when each parameter is at its minimum (blue) or maximum (pink)

To summarize: these ranges assure a well defined t_{th} because there is always an AP elicitation: we have acted according to the DoE intrinsically iterative and adaptive procedures in redefining the ranges and eventually the choice of the parameters to investigate. Fig. 55 depicts the data scattering in determining the PF $t_{th.}$.

Here we can observe how again, also for the rapidity of AP birth, the main factor is certainly by far the slope of the input waveform because there is no overlapping of data thanks to a shift from minimum to maximum of approximately 0.1ms in the PF.

Now it is possible to build a regression model for the data, interpolating them. We have decided to exploit MATLAB *rstool* functionalities, providing the possibility to obtain exploring graphs of multidimensional polynomials. The function can be used to perform an interactive fit and plot of a multidimensional response surface (RSM). Moreover this GUI offers an environment for exploration of the graph of a multidimensional polynomial.

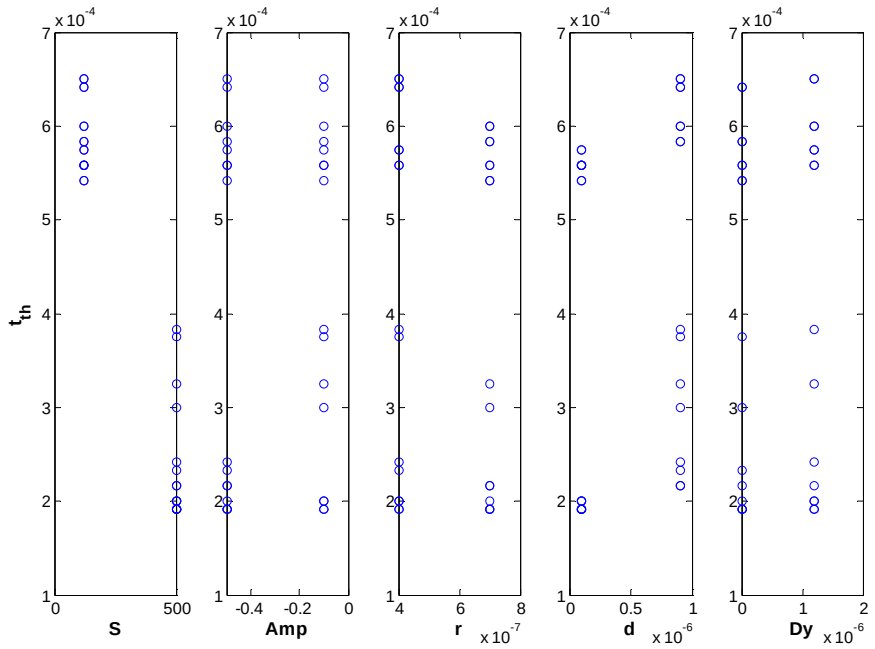

Fig. 55 Dex scatter plot for t_{th} PF [s]

In Fig. 56, each plot shows the fitted relationship of the PF to the independent variable at a fixed value of the other independent ones. The fixed value of each independent variable is also editable in a text box below each axis, and is marked by a vertical dashed blue line (in the reported case it is the middle point for each factor).

It is thus possible to change the fixed value of any independent variable by either typing a new value in the box or by dragging any of the vertical lines to a new position and this is particularly useful for searching the best parameter combination minimizing or maximizing the PF.

Indeed, changing the value of an independent variable, all the plots update to show the current picture at the new point in the space of the independent variables.

With this particular choice of the parameters PF, estimation value can thus be easily obtained, moving the blue cursors along the regression function representation (green), thus t_{th}= 0.414 ms together with its estimation uncertainty ($2.688 \cdot 10^{-5}$s), which is calculated on the bases of the chosen extent of confidence (in our case 99%), with which the

model makes the prediction that a further sample could fall within the green line delimited zone.

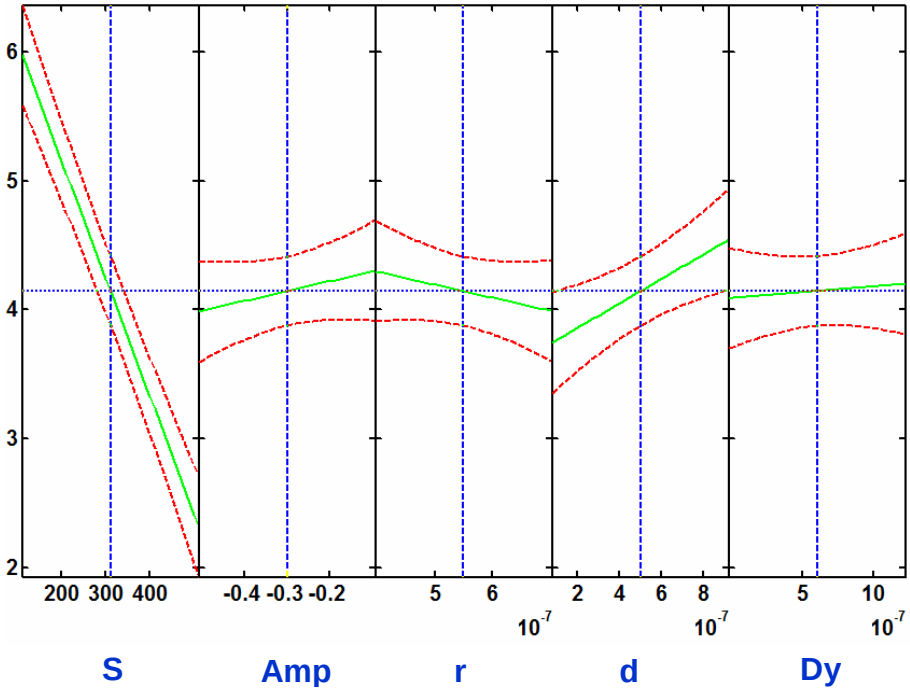

Fig. 56 Linear prediction plot t_{th} (measurement units: 0.1ms)

The interpolating function obtained is instead:

$$t_{th} = \beta_0 + \beta_1 S + \beta_2 Amp + \beta_3 r + \beta_4 d + \beta_5 D_y + \varepsilon \qquad (49)$$

where β_0=7.218·10^{-4}, β_1=-9.155·10^{-7}, β_2=7.552·10^{-5}, β_3=-97.222, β_4= 95.05, β_5= 86.806 (the βs have each the opportune measurement units as to obtain seconds, in the multiplication by their factors) and ε = 3.275·10^{-5} represents the RMS regression error. This last value is particularly important since it gives us (as pointed out in the summary of the theory underlying regression and curve fitting) the opportunity to estimate the quality of the approximation made by the interpolating function. Furthermore, it is necessary to precise that, obviously, the weight of a factor does not depend only on its interpolation coefficient

β, but also on the values it assumes on its assigned variation range.
Thus, taking into account all the observations made until now, from the analysis we have conducted on the rapidity with which the AP starts and also observing slopes of the function for each plot in Fig. 56, it can be inferred that the phenomenon (within variation domain of the parameters) is mostly sensitive to *S*, the slope of the waveform, then in decreasing order, to the distance from the nanoelectrode and the axon, then to nanoelectrode radius and signal stress more or less at the same rate and in the end to the transversal displacement.
This information could be very useful for a NEA designer when he has to unavoidably tradeoff choices among the typical adopted ranges of these parameters.
With this in mind, if we search the best parameter solution (as far as a linear prediction can attain) with the tool presented, we obtain:

Table 18 Best solution set of parameters minimizing t_{th}

Parameter	**Adopted range**
S	509.5 V/s
Amp	-510mV
r	707nm
d	80nm
D_y	-30nm

It must be noticed that it is not strange that the obtained best values exceed the minimum or maximum because the regression implemented makes prediction also for tiny areas beyond the assigned ranges and that certainly symmetry considerations on D_y make us understand that its although its estimated best value is -3nm its real one should be 0.

Moreover, It could be useful to refine our study on the behaviour of the PF, by choosing (always in the iterative approach scenario of the DoE) to investigate better the case when we fix the position of the nanoelectrode and more accurately predict the behaviour of t_{th}, adopting a 3^k (k=2 parameters) levels full factorial experiment, where the to variable parameters are obviously *S* and *Amp* (the waveform parameters). We will thus have the opportunity to determine a full quadratic regression of the promptness of the system as a function of these two parameters.

4.3.1.2 Quadratic regression model for the AP starting time

The quadratic regression model we have set up uses the ranges reported in Table 19. Each variable assumes each of the three values.

Table 19 Adopted ranges for the quadratic regression model fot t_{th}.

Parameter	Adopted range (with middle point)
S	[120, 310,500]V/s
Amp	[-500,300,-100] mV

These new iteration more deeply investigates the behaviour of the PF with respect to the two signal parameters *S* and *Amp*. The results summarized in Fig. 57 show that again *Amp* for the considered values is not too relevant as far as the speed of activation is concerned, but we can infer the quadratic model for t_{th}

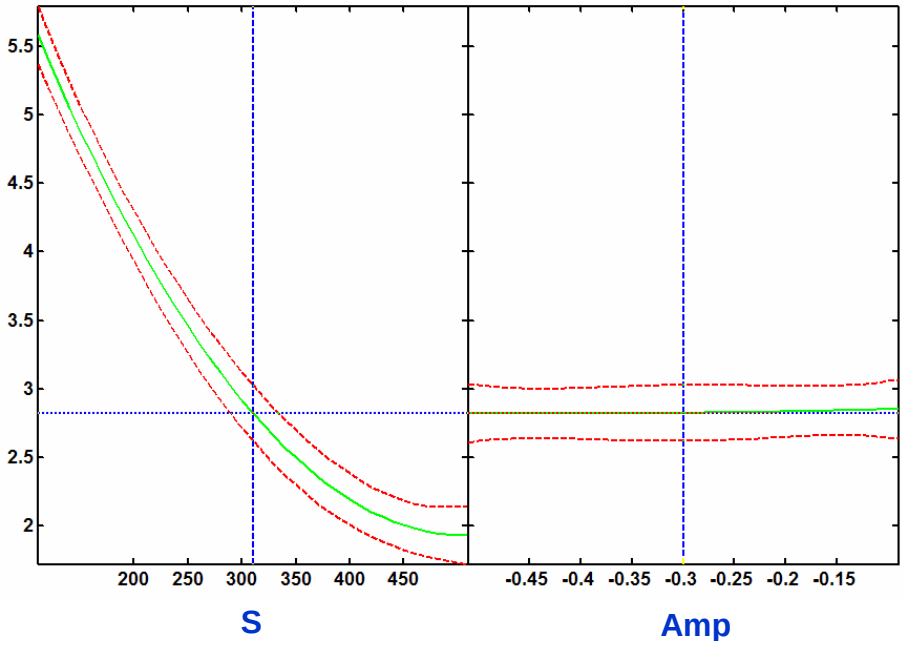

Fig. 57 Quadratic prediction plot t_{th} [0.1ms]

Indeed we obtain the following fitting model:

$$t_{th} = \beta_0 + \beta_1 S + \beta_2 Amp + \beta_{12} SAmp + \beta_{11} S^2 + \beta_{22} Amp^2 + \varepsilon \qquad (50)$$

while the new quadratic model interpolation coefficients are: β_0=7.913·10^{-4}, β_1=-2.352·10^{-6}, β_2=1.078·10^{-5}, β_{12}=5.482·10^{-8}, β_{11}=2.346 10^{-9}, β_{22}=3.472·10^{-5} and ε= 2.121·10^{-6}. We can also represent this function as in Fig. 58.

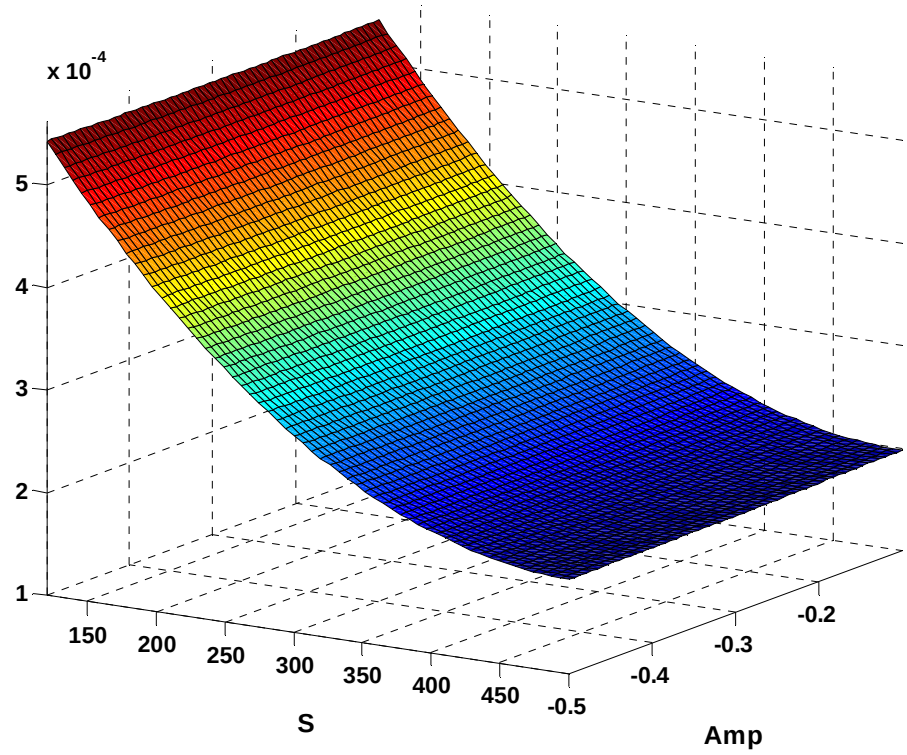

Fig. 58 Response surface as deduced by quadratic regression model for t_{th} [s]

4.3.1.3 AP duration Temperature dependence analysis

After having analyzed the effect of signal and geometrical parameters of the input stress on the promptness of the system response, now we

perform another analysis whose investigation is still concerned about time membrane dynamics, but takes into account a new variable: the operating temperature.

During this experiment we have fixed our attention to the first of the implemented and described stimulation system (axon segment undergoing a nanoelectrode induced stimulation as for the last section).

Here the stimulus parameters are fixed (in terms of geometrical characteristics of the nanoelectrode and time shape of the input stressing signal) with exception of the waveform absolute value of the slope which is varied together with temperature.

We chose the variation range for the it to be [18 26]°C because it is nearer to the temperature measurements Hodgkin and Huxley performed during their research activity, oriented to capture axon membrane physics and thus we are more confident on the reliability of the approximation HH FEM model makes on the real neural cell behaviour [49].

The objective of this investigation is to furnish a regression function describing the correlation between temperature (T) variation and signal slope shifts on the duration of the AP (which in turn affects also the constraint on the maximum per unit of time number of APs that can be activated to code retina ganglion cells information). The knowledge we can obtain this way, could be useful even if T is not a design parameter, but even just to dig more deeply into the mechanisms underlying axon membrane behaviours.

First of all it must be highlighted that our choice for the stress parameters has fallen within the same ranges already adopted for the study on the t_{th} performed with a T=22°C, this value had been chosen because it is typically adopted in literature when modelling HH behaviour. It is worthwhile reminding that although HH equations are by far the most frequently used and have many computational and general adaptability to different types of situations, they nevertheless, suffer from the fact that they do not propagate action potentials above 31 °C.[3] Now we can go through the description of the adopted experimental choices. We have, indeed, assigned to nanoelectrode radius, to its length and to its transversal displacement the middle values of the cited ranges. We wanted to determine a generic function binding rapidity of membrane dynamics temporal evolutions to

temperature and stress signal parameters variations and not the one that could emerge from "forcing" the system to work at its best conditions for the other studied case (4.3.1.1) .

In addition to this it must be said that, in this section, we have conventionally defined the *PF*, *w*, in terms of time difference between the instants of consecutive crossings of AP and the time axis).

Again we perform a 3^k experiment with variables defined in the ranges reported in Table 20.

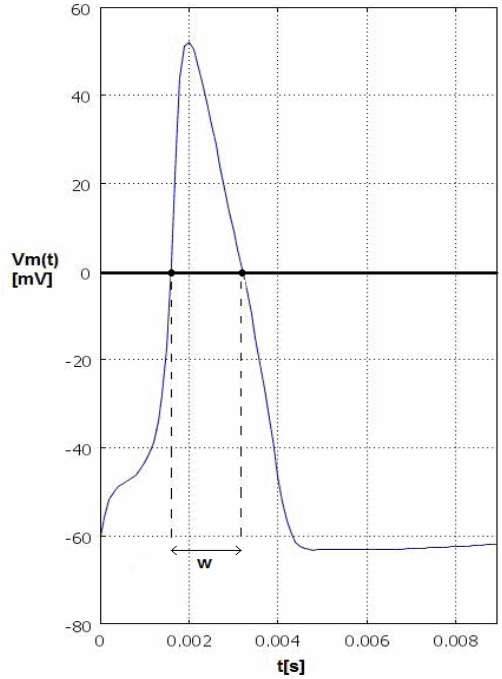

Fig. 59 Definition of PF *w*.

Table 20 Adopted ranges for the quadratic regression model for t_{th}.

Parameter	**Adopted range (with middle point)**
S	[120, 310,500]V/s
T	[18,22,26] °C

The quadratic regression implemented on the set of data obtained brings to:

$$w = \beta_0 + \beta_1 S + \beta_2 T + \beta_{12} ST + \beta_{11} S^2 + \beta_{22} T^2 + \varepsilon \quad (51)$$

with, β_0=7.925·10^{-4}, β_1=·9.256·10^{7}, β_2=2.595·10^{-6}, β_{12} =7.675·10^{-8}, β_{11}= -4.039·10^{-9}, β_{22}= -1.302·10^{-6} and ε= 4.547 ·10^{-5}.

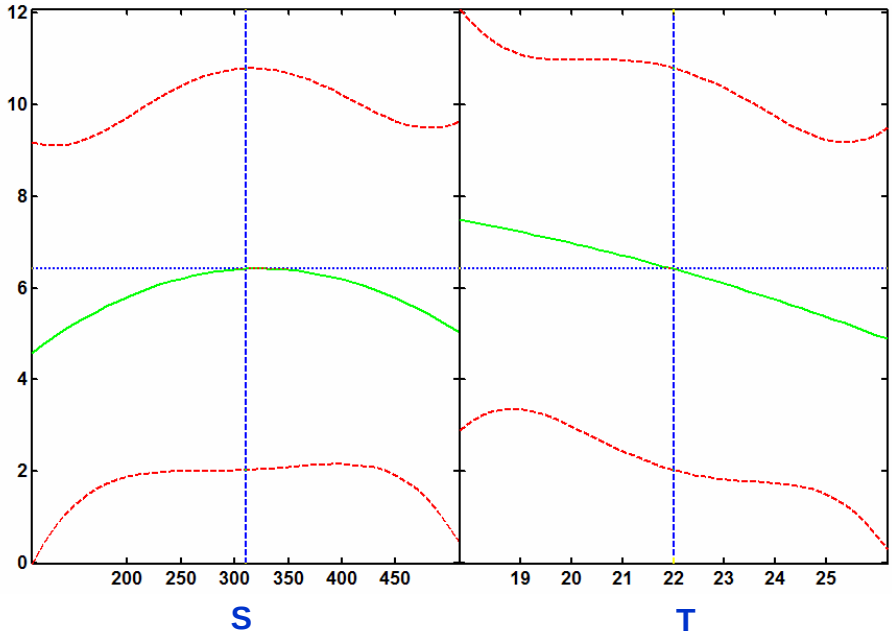

Fig. 60 Quadratic prediction of the PF *w* (measurement units: [0.1ms])

We can observe from Fig. 60, that apart from the promptness of the system (estimated with t_{th}), membrane dynamics are (more in general) deeply affected by the waveform input slope *S*. We can also observe that the dependence on temperature is in keeping with theoretical expectations since data announce a non linear but decreasing dependence from the it of the AP duration *w*. We have just highlighted and also estimated qualitatively what we had already qualitatively described in our 2D model. Indeed the specific behaviour of *w* with an increase of *T* is explainable with the effect of the correction coefficient that HH equations report for the channel dynamics (§ 3.2.4). Tridimensional representation of the fitting curve is also

reported in Fig. 61.

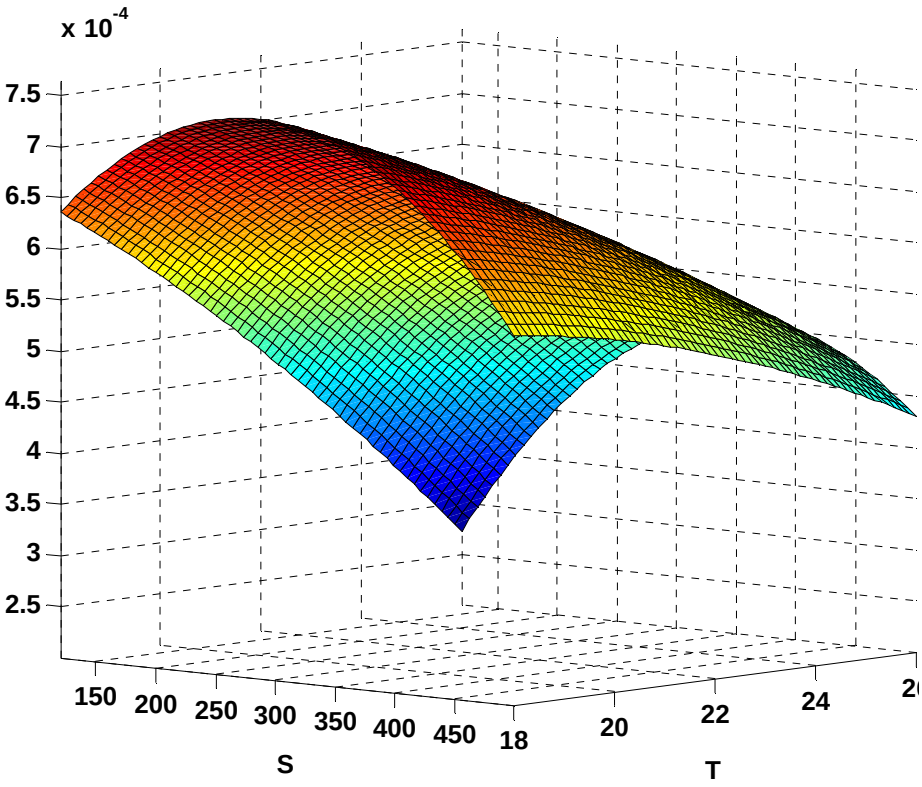

Fig. 61 Response surface as deduced by quadratic regression model for *w* [s]

4.3.1.4 Analysis of peak value of TMV dependence on stress input parameters

We have realized even more clearly during our first working phase that it is worthwhile finding a way to model more *quantitatively* dependences of PFs on variable factors of the system under study. We have, thus, wondered whether it was possible to refine our knowledge on the values that the TMV assumes under the types of stimulation we are considering, since perhaps among the various membrane electrophysiological parameters that we can imagine to analyze the TMV is the most important since it is strongly bound with the birth of the nervous signal. Thus, implemented an iterative search of the peak

value that the TMV assumes for the axon segment stimulated (with parameters ranging within the windows reported in Table 16), we have defined the analogical PF as the maximum value V_{mM} of the TMV itself, calculated all over the nervous fibre under stress.

Indeed, by observing it we can infer the slopes of the PF and thus not only generically the directions towards which it is desirable to move along parameters ranges, but also quantitatively the extent of the dependencies, thus obtaining a fitting function from simulated data.

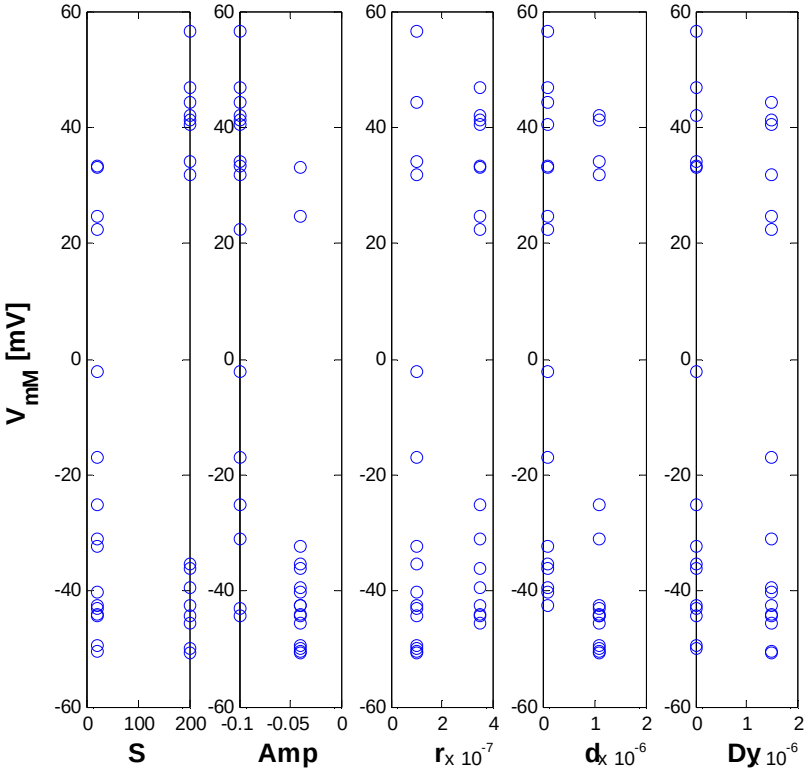

Fig. 62 Dex scatter plot for V_{mM} PF [mV]

The interpolating function for V_{mM} is, in the end, reported below . It must be noted that V_{mM} is expressed in mV and that this regression presents a percent greater variability due to the nonlinear triggering (or not) of the APs and thus, perhaps, a tiny worse quality.

$$V_{mM} = \beta_0 + \beta_1 S + \beta_2 Amp + \beta_3 r + \beta_4 d + \beta_5 D_y + \varepsilon \qquad (52)$$

with, β_0=·-74.249, β_1=0.104, β_2=-8.082·10^2, β_3 =6.669·10^7, β_4=-2.671·10^7, β_5= -3.577·10^6 and ε= 25.6.

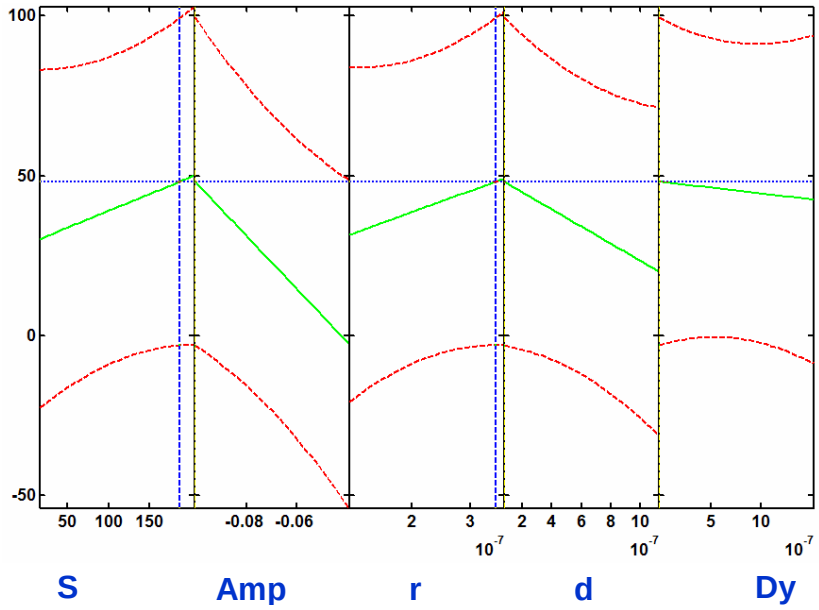

Fig. 63 Linear prediction plot for V_{mM} at the optimum solution[mV]

The analysis of the results obtained in the simulations elaborations leads us to observe that since we know from § 4.3.1.1 that elicitation of APs is principally favoured by a greater signal waveform slope, even though the evaluation of the peak amplitude of TMV over the stressed neuron axon is important, it cannot be used exactly as direct estimator of the on-off phenomenon of spike generation. There, indeed, can be cases favoured by a growth in the most prominent factor, which is also intuitively the signal amplitude, *Amp*, that lead in the direction of an increase of TMV peak but they are not sufficient to elicit AP. This also demonstrates (if necessary) the high nonlinearity of the phenomenon under observation. Moreover, for the same reasons, it is interesting to note that there is a much greater general dependence of this new PF on the set of parameters than for $t_{th.}$ This is

in accordance with Fig. 54 (where the number of born APs is represented): greater distributed dependence can be observed when the PF is t_{th}. It is worthwhile noting that this deeper and more quantitative analysis is in perfect accordance with the previously shown bar diagram qualitative predictions of the same cited figure (Fig. 54), as for the directions towards AP triggering. Moreover, the slightness of the dependence of AP triggering phenomenon on D_y (here more precisely estimated), was not clarified by the coarser estimation made counting the APs.

4.3.2 Analysis on the model with soma, axon hillock and axon initial segment (in the thin layer approximation)

What we have observed and modelled until now is relative to an axonal stimulation, but it is interesting to examine what happens if, not just the axon, but the zone near the ganglion cell soma undergoes a stress voltage in order to promote its signalling activity. We know from literature [3] that soma are more easily activated because of a smaller surface curvature with respect to the one offered by axon, thus we have chosen to simulate a slightly small soma with respect to the typical ones in the retina in order to reduce computational burden and also knowing that stresses capable of triggering APs in somas with smaller radii certainly stimulate them better in those with a smaller surface curvature, because the “effective area” underneath is bigger. Therefore we have decided to investigate a worst case situation Thus the model implemented (as described in §3.3.3) has been used (with a soma radius of 5μm) to investigate this new situation main features. The imposed voltage waveform has the same shape as in Fig. 51 with *Dur*=0 (thus collapsing into a triangular wave as in all the cases previously examined with *Dur* parameter fixed). Initially we had decided to use, where possible for the way the parameter is defined, the same ranges adopted for the analysis on the case of the singular axon.

Nevertheless, (as more than on time discussed in the section dedicated to the theory of DoE, ranges good choice is one of the most difficult and laborious things to achieve) a slightly different definition has proved necessary together with a change in a variable parameter.

In particular since as we have already pointed out in §4.3.1.1 anatomical considerations suggest to fix the upper base of the nanoelectrode support distance from the neuron, here in presence of the geometrical shape of the soma we cannot say that fixing the length of the nanoelectrode means fixing the distance from the neuron, thus within we refer directly to nanoelectrode length l_n .In addition to this we introduce another observation variable: D_x defined (as reported in Fig. 64) as the displacement of the electrode from the longitudinal positioning along x axis just on the upper pole of the soma (D_x = -12.25μm) or to the middle of the axon segment (D_x=0).

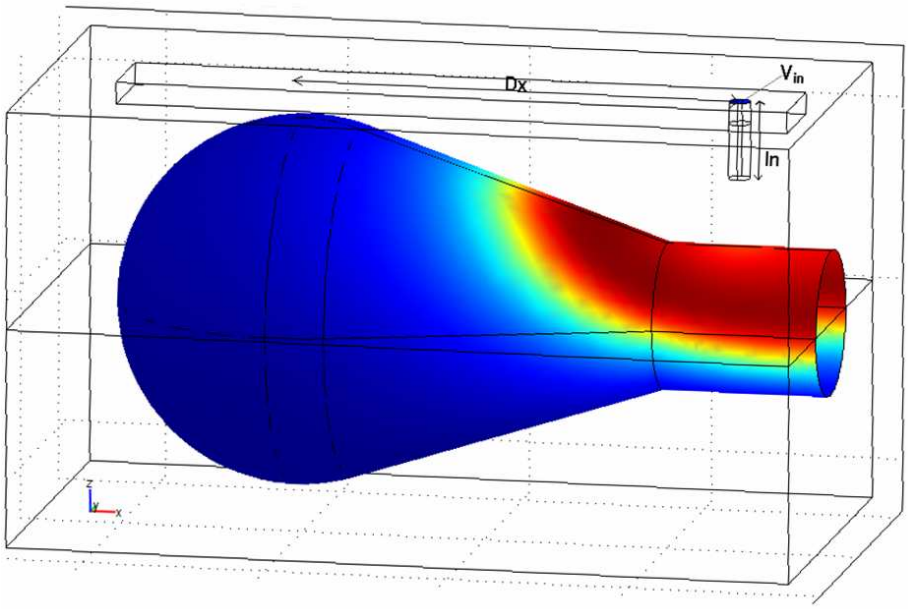

Fig. 64 Example figure with an activated AP under the electrode (TMV is higher toward the red color) used to show parameters definition: D_x, l_n.

In order to try to furnish a better representation of reality, since this model is much more complex than the other until now analyzed, we have widened some ranges, changing the extreme that led in the direction of a much greater number of APs births to better observe a situation that more likely would have brought to their elicitation. We have managed to do this, by exploiting the information gained by observing the slopes of linear prediction plots obtained in the case of

singular axon stimulation.

Table 21 Range of parameters adopted for the analysis on the initial zone of the axon near the soma.

Parameter	Adopted range
S	[40,200]V/s
Amp	[-200mV,-40mV]
r	[300nm, 800nm]
ln	[600,1400]nm
D_y	[0,1.5µm]
D_x	[-12.25,0] µm

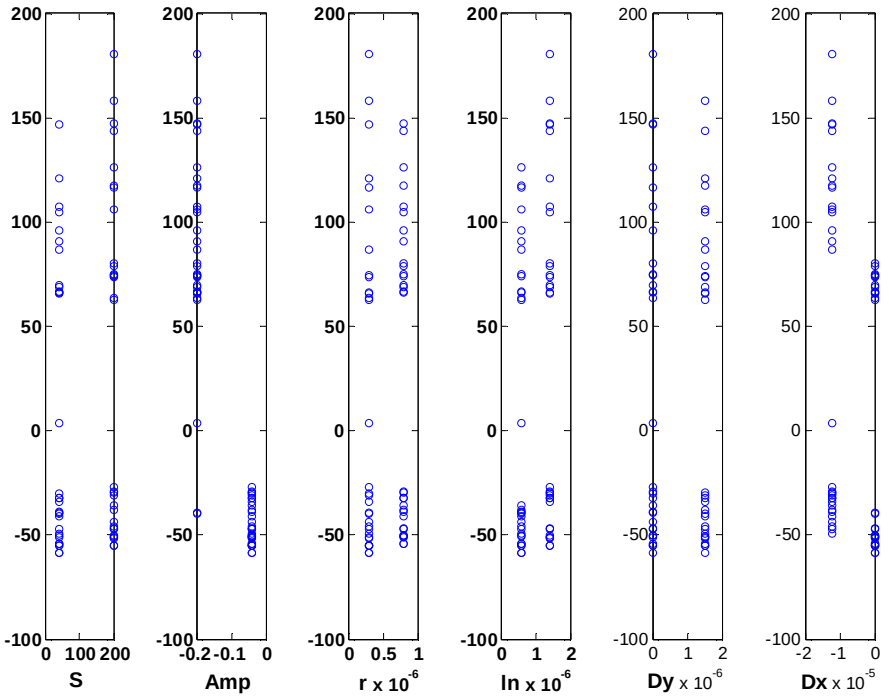

Fig. 65 Dex scatter plot for V_{mM} PF [mV] in the case of a stimulation near the soma

The interpolation of scattered data brings to:

$$V_{mM} = \beta_0 + \beta_1 S + \beta_2 Amp + \beta_3 r + \beta_4 l_n + \beta_5 D_y + \beta_6 D_x + \varepsilon \quad (53)$$

with, β_0=-1.515·10^2, β_1=12.71, β_2=-8.189·10^2, β_3 =2.078·10^7, β_4= 2.882·10^7, β_5==-4.508·10^5, β_6==-3.071·10^6,and ε= 25.3.
Moreover, we must precise that although the interpolation is not of high quality as in the case for the single axon, the PF V_{mM} that we have selected can still be used as a guideline for the nanoelectrodes system designer, who can now benefit from the knowledge on the weight of a parameter with respect to the others (Fig. 66).

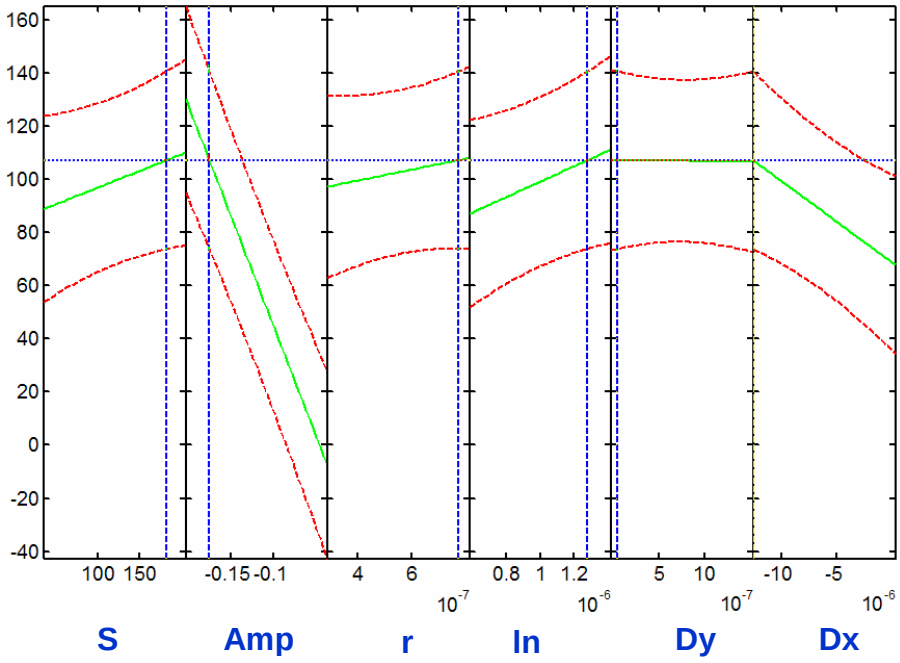

Fig. 66 Linear prediction plot for V_{mM} at parameters best solution[mV]

Again general variability with the parameters (and unfortunately also a tiny coarseness of the interpolation) has grown with respect to the time dynamics observed in § 4.3.1.1 and 4.3.1.3 as for the case of V_{mM} with which obviously shares the signs in the rates of change of the linear interpolation for each of the common parameters (S, Amp, r and D_y) and this is quite intuitive. For l_n we must remind that, in the axonal model, defining d or l_n was equivalent since they added up to

generate the total distance from the upper tangent plane to the neuron and the upper base of the support for the nanoelectrode (Fig. 52). Since here this is not true any more, for a fixed l_n (the parameter that we can really design) different distances from the upper profile of the neuron are assumed depending on the position along x axis of the nanoelectrode. Thus if in the other model we had reported the dependence on l_n instead of d it would have had the same sign of this case analysis. Moreover no comparison can be done for linear approximation rate of dependence on D_x. because it was undefined in the other analyzed situation. It is possible to notice also that D_y has decreased in importance likely because of the presence in this model of the axon hillock. It indeed, with a ten times greater membrane channels density with respect to the other zones (soma and axon) represents the most "sensitive" zone to the triggering of APs, thus making more in general soma zone stimulation easier than near the axon. Thus we obtain a confirmation of what expected from literature data. Nevertheless it is not completely advisable to stimulate here. Reportedly, ([3]) since in the reality, near soma zone there are also dendrites, that, due to their arborisation create sensible neuron segments overlapping, a reduction in the spatial resolution of the stimulations and thus the AP elicitation selectivity would emerge.

Anyway this phenomenon could be better investigated adding a third point in the range of D_x and refining our analysis on the dependences choosing the most relevant factors and implementing a 3^k (as already done) full factorial experiment.

4.3.3 Analysis on the biaxonal model for the selectivity (parameters design to avoid parallel neurons activation)

One of the most pernicious troubles of neurostimulation as we know from § 3.4 is the difficulty to be selective in addressing a specific neuron (or a group of neurons/axons), because, as we have already mentioned, this leads, especially in the case of the retina dense neuronal patterns, to a distortion of the coded information induced on the axon themselves by the neurostimulation device. It is keeping this in mind that we have concluded our analysis on neuron dynamics by trying to determine the most relevant factors predisposing a voltage

stressed simple couple of axons to be selectively activated. Ranges adopted are those of Table 17, exception made on the parameter *S*.
For this, a wider range lowering the minimum value (60V/s) has been chosen, trying to obtain also cases where the "victim" did not activate any AP, to better distinguish between cases, but always seeking the triggering in the first one (as it has really happened). We must evidence that for D_y parameter, its upper limit is chosen as the 24% of the distance between the centres of the two axons, in order to keep the nanoelectrode in any case nearer to the target axon: the first one. The definition of the performance function has been done trying to find an analogical variable that could convey information on a on off phenomenon (the selective triggering of APs in the first one and not in the second one). The most suitable PF in this case appeared to be somehow correlated with the peaks of the TMVs in the target and in the victim axon. In particular, seeking ranges capable of always activating the APs in the first intended target axon, it is sufficient to observe the peak value of the "victim" TMV in order to determine whether the stimulation has been selective or not. If it is negative no AP has born in the second neuron; if not, no selectivity has been granted.

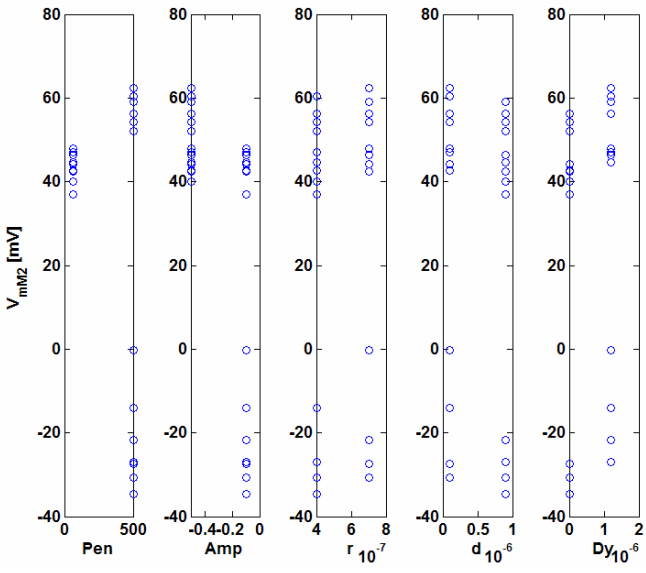

Fig. 67 Dex scatter plot for V_{m2M} PF [mV]

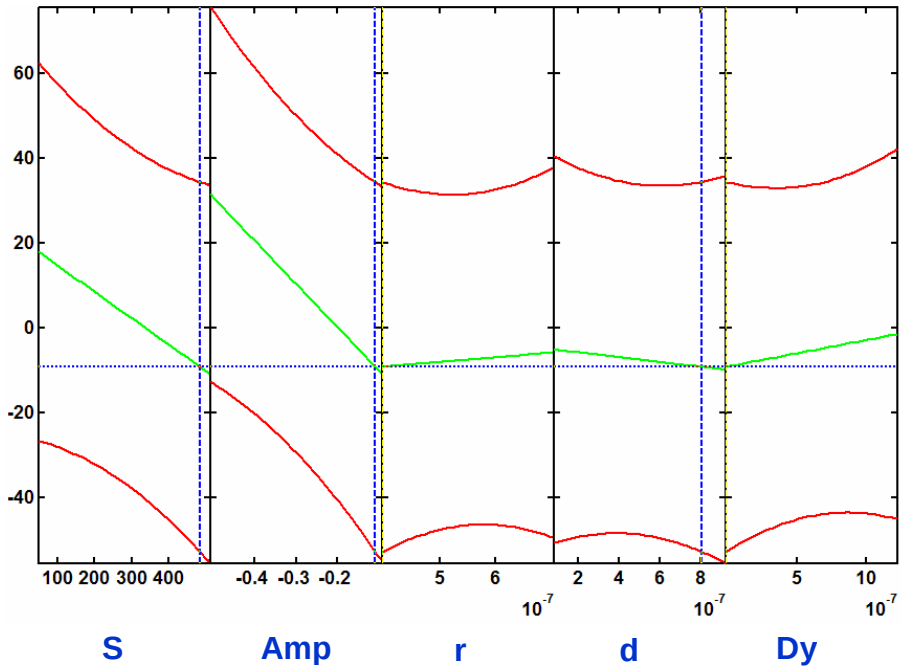

Fig. 68 Linear prediction plot for V_{mM} at parameters best solution[mV]

The interpolation of scattered data brings to:

$$V_{mM2} = \beta_0 + \beta_1 S + \beta_2 Amp + \beta_3 r + \beta_4 d + \beta_5 D_y + \varepsilon \qquad (54)$$

with, β_0=10.976, β_1=-6.237·10^{-2}, β_2=-1.006·10^{-2}, β_3 =1.080·10^{7}, β_4=-5.674·10^{6}, β_5=6.134·10^{6} and ε= 22.4.

It is very interesting to note that while *S* parameter was the most influent for the other performances considered until now, here, for the selectivity, not only does it loose the main factor prominence (*Amp* is much more relevant), but also changes its effect in sign: while for minimizing (as we need to do know) the TVM peak there was the necessity to push the S to lower values, here it is exactly the opposite. This can be explained, thinking that the values assumed by the distance D_y (here becoming much more meaningful) from the "victim" is far beyond the ones simulated until now. It was : at most equal to 1.5µm in the other cases and it now ranges within [(5-1.2)µm, 5µm].

Thus, a different domain for the PF (with respect to the victim axon) is being investigated. Instead for the other parameters the first order dependences have the same sign. This last analysis and discovering could prove very helpful. First of all, the opportunity is offered to determine the optimum combination of parameters minimizing the TMV of the victim axon ,V_{mM2}, as shown in Fig. 68. This, in turn, makes it possible to be more confident that it will be only the AP in the first axon to be triggered (we remind that the chosen ranges have proved effective in always eliciting the first axon AP). Secondly, the behaviour of the function in dependence of the slope *S* of the input waveform can be in general better investigated and exploited since pushing towards higher slopes (at least for these ranges) seems to be an attractive way of assuring the target excitement and also a greater selectivity.

At the end, it would be an interesting goal to achieve in future works , the exploitation of this model in order to investigate (always through the analysis of experiments) the reasons why the second APs is triggered, when it happens: direct elicitation (due only to nanoelectrode effect), the presence of the other close axon perturbing field lines or even both? Applying again DoE to test this hypothesis could lead to an efficient tool to design nanoelectrodes systems also taking into account the issue of the so called *focal confinement* of the input stress current fluxes lines , thus increasing the selectivity of the stimulation and, in a global high-scale vision the, spatial resolution attainable.

Conclusions and future work

The importance of the work lies not only in having used a systematic approach for determining the sensitivity of electrophysiological parameters of nerve cells membrane, in order to better understand its functioning and, eventually, to optimize the parameters of a possible stimulation, but also in having built a tool that can be quite easily expanded and improved, by introducing other dependencies. Indeed, using the potentiality of the field solution, the FEM approach (instead of the classical compartmental one) and the multiphysical nature of the software adopted, the proposed thin layer approximated model allows to overcome calculus burden limitations due to the high nonlinearity of the membrane dynamics and also to its extremely high form factor.

We have studied various stimulation cases: along the axon, near the soma zone, with a couple of fibres.

The implemented models have been validated using literature data and comparing the simulated membrane responses with them (in terms of typical underthreshold and overthreshold stimulations or in terms of dependence on the temperature and on the relationship between distance among repeated input pulses and membrane refractory period).

The other meaningful contribution of the work is also represented by the application of a systematic and typically engineering investigation technique (the DoE) to a different field: the neuron electrophysiology, with particular focus on neurostimulation.

Indeed, often in literature, approaches to similar situations adopt simplified HH equations (e.g. model of FitzHugh-Nagumo) in order to perform quicker analysis or even linearized or passive models when the focus is on the bioelectromagnetic effects generated by applied fields. On the contrary there are various *in depth* modelling approaches that do not realize a systematic analysis procedure on the obtained data. This work, instead, integrates the two typical perspectives, thus being able to foresee complex biological effects an to investigate them from a global point of view.

By now, we are we have offered a general panoramic on the extent of sensitivity of main membrane features on a set of chosen

parameters of interest. Investigation that, in future, could be also widened, to take into account more design and uncontrollable parameters.

All the analysis that we have implemented, on the realized neurostimulation system models, aim at furnishing a (though partial) helpful background pre-information on the effectiveness of certain types of nanoelectrodes simulations with respect to certain others, with especial focus on retinal prosthetics .

The first analysis we have conduced (once an appropriate search is made of suitable parameters ranges) is dedicated to the prediction of the AP triggering speed, which is a measure of the system response promptness. This investigation could be useful when particularly high frequency bursts of APs are needed to code specific optical information. We have analyzed various stress parameters: the slope of the input signal waveform, its peak amplitude, geometrical nanoelectrode parameters, such as radius, length and transversal displacement with respect to the axon symmetry axis. The results obtained show that the most prominent feature for this PF can be identified with the slope of the waveform, then in decreasing order, the nanoelectrode length, its radius and the signal stress parameters (more or less at the same extent) and, in the end, the transversal displacement.

The second analysis (a 3^k experiment) exploits our axon segment model to investigate quantitative dependence of the AP spike duration on the operating temperature. Here we observe a quadratic dependence of the AP duration on the *signal slope*, while, in keeping with theoretical expectations a negative *slope of the PF* with respect to temperature can be observed. This is explainable with the effect of the correction coefficient, that HH equations report for the dependence of channel dynamics on temperature.

The third and the fourth analysis, we have conduced, investigate the sensitivity of TMV peak value to variations with the same parameters ranges of the lately described stimulations. In particular we investigated effects, when neurostimulation is performed along the axon and in proximity with the soma. In particular in the third, we have discovered that also for this new PF, an increase in signal waveform slope has great effects, but here the signal peak amplitude (in absolute value) is more important.

Instead, for the fourth case analysis, where the stimulation is made in presence of the soma, it has been possible to notice that the transversal displacement has lost of importance, because of the different curvature of the soma, compared with that of the axon. Moreover, channels density increase on the axon hillock mitigates the effects of this parameter too. For the same reason, the positioning of the nanoelectrode directly over the top of the soma or at the initial segment of the axon is the most relevant parameter in this analysis.

In the end, another experiment is performed, aiming at studying the influence of the cited controllable design parameters on the possibility to selectively elicit APs, focusing on one axon rather than its neighbour. Our investigation has brought to a pair of remarkable consequences: the opportunity is offered to determine the optimum combination of parameters minimizing the TMV of the victim axon, thus increasing the confidence with which we can assert that we have exclusively triggered an AP only on the first axon. Secondly, we have found out an attractive tendency of the PF, as a function of the slope of the input waveform (at least for the chosen ranges). It could be, indeed exploited, pushing the slope to higher values, because this goes in both the directions: facilitating the first axon spiking and, at the same time, preventing the second axon from being activated. This in turn can be translated in an increase in the system spatial resolution. Which was one of the primary goals in retinal prosthetics.

As far as the future possible developments this work allows, there is a wide range of perspectives that can be enquired about.

- Due to the growing literature interest devoted to applications of magnetic and higher frequencies electromagnetic fields to neural tissue, the study conducted and the models introduced can be used for investigating their effects or to determine the extent of electromagnetic susceptibility of the prosthetics devices to them.

- It would be interesting also to study the dependences that distortion of the coded retinal information has on temperature. This can be accomplished, analyzing its influence on the AP duration and, asa consequence, on the maximum number of spikes per unit of time that are producible.

- Simulations with many nanoelectrodes emulating a greater area of a NEA could be done to better tailor their spatial pitch between nanoelectrodes, as a function of the axons distribution underneath.

- The introduction of a set of equations, describing heat conduction within the cell and within the membrane, in particular; could help in assessing the constraints for the applied signals, in terms of cell viability

- In the end, clusters of axons (instead of two) could be simulated, while undergoing a stimulation (exploiting the thin layer approximation model to reduce power of calculus requirements) to determine best selective set of parameters, when the scenario is much more complicated than the examined one.

References

[1] Cassell AM, Li J, Nguyen-Vu TDB, Koehne JE, Chen H, Andrews R, Meyyappan M (2009) Vertically Aligned Carbon Nanofibers: Interconnecting Solid State Eectronics with Biosystems. Journal of Nanoscience and Nanotechnology, Vol 9, No 8, pp. 5038-5046(9).

[2] Berger et al (2003) Brain-Implantable Biomimetic Electronics as Neural Prosthetics. In Proceedings of the 1st International IEEE EMBS Conference on Neural Engineering, Capri Island, Italy, 20-22 March 2003.

[3] Greenberg RJ, Velte TJ, Humayun MS, Scarlatis GN, de Juan EJ (1999) A computational model of electrical stimulation of the retinal ganglion cell. IEEE Trans Biomed Eng 1999;46:505–14.

[4] Berdondini L, van der Wal PD, Guenat O, de Rooij NF, Koudelka-Hep M, Seitz P, Kaufmann R, Metzler P, Blanc N, Rohr S (2005) High-density electrode array for imaging in vitro electrophysical activity. Biosensors & Bioelectronics, 21:167-174.

[5] Butson CR, McIntyre CC (2006) Role of electrode design on the volume of tissue activated duringdeep brain stimulation. *J Neural Eng*. 2006 March ; 3(1): 1–8. doi:10.1088/1741-2560/3/1/001.

[6] Chiappalone M., Bove M., Vato A., Tedesco M. Martinoia S.(2006) Dissociated cortical networks show spontaneously correlated activity patterns during in vitro development Brain Research Vol. 1093, Issue 1, 6 June 2006, Pages 41-53.

[7] Cogan SF (2008) Neural Stimulation and Recording Electrodes. Annu. Rev. Biomed. Eng. 2008. 10:275–309.

[8] Daliang LL, Journee HL, Rath WT, van Hulzen A, Sclabassi RJ, Mingui S (2006) Finite Element Analysis of Action Potential Generation in the Cortico-Spinal Tract During Transcranial Electrical Stimulation. Proceedings of the IEEE 32nd Annual Northeast Bioengineering Conference, 2006, pp.111-112, doi.10.1109/NEBC.2006.1629777.

[9] Daniel J et al (2003) Chronic Intraneural Electrical Stimulation For Prosthetic Sensory Feedback. In Proceedings of the 1st International IEEE EMBS Conference on Neural Engineering, Capri Island, Italy, 20-22 March 2003.

[10] Massobrio P, Baljon PL, Maccione A, Chiappalone M, Martinoia S (2007) Activity modulation elicited by electrical stimulation in networks of dissociated cortical neurons. Proceedings of the 29th Annual International Conference of the IEEE EMBS Cité Internationale, Lyon, France, August 23-26, 2007.

[11] Rodger DC, Fong AJ, Li W, Ameri H, Ahuja AK, Gutierrez C, Lavrov I, Zhong H, Menon PR, Meng E, Burdick JW, Roy RR, Edgerton VR, Weiland JD, Humayun MS, Tai YC (2008) Flexible parylene-based multielectrode array technology for high-density neural stimulation and recording. Sensors and Actuators B: Chemical, 132 (2). pp. 449-460.

[12] Aguera y Arcar B, Fairhall AL, Bialek W (2006) Computation in a Single Neuron: Hodgkin and Huxley Revisited. MIT Press Journals Vol. 15, No. 8, Pages 1715-1749.

[13] Andrews RJ (2007) Neuroprotection at the Nanolevel—Part II Nanodevices for Neuromodulation—Deep Brain Stimulation and Spinal Cord Injury. Annals of the New York Academy of Sciences Volume 1122, Neuroprotective Agents: Eighth

International Neuroprotection Society Meeting pages 185–196, doi:10.1196/annals.1403.013.

[14] Rattay F, Aberham M (1993) Modeling axon membranes for functional electrical stimulation. IEEE transaction on Biomedical Engineering, vol. 40, no 12, pp.:1201-9.

[15] Rattay F (1998) Analysis of the electrical excitation of CNS neurons. IEEE transaction on Biomedical Engineering vol. 45, No 6, pp: 766-772.

[16] Rattay F (2006) Functional Electrical Stimulation of the Central Nervous System: Analysis of the Primarily Excited Structures. Doctoral Thesis at the Medical University of Vienna within the scope of the "Doctor of Medical Science”.

[17] Bossetti CA, Birdno MJ, Grill WM (2008) Analysis of the quasi-static approximation for calculating potentials generated by neural stimulation. J. Neural Eng. 5 (2008) 44–53, doi:10.1088/1741-2560/5/1/005.

[18] Chader GJ, Weiland J, Humayun MS (2009) Artificial vision: needs, functioning, and testing of a retinal electronic prosthesis. Prog Brain Res. 2009;175:317-32.

[19] Chow AY, Peachey NS (1998) Subretinal microphotodiode array retinal prosthesis. Ophthalmic Research 1998; 30(3): 195-8.

[20] Eckmiller RE, Baruth O, Neumann D. (2005) Learning retinal encoder RE*: results from dialog-based tuning in human with normal vision ARVO Abstracts. Invest Ophthalmol Vis Sci 2005; 5266/B469

[21] Finn W, LoPresti P (2003) The Handbook of Neuroprosthetic Methods, CRC Press.

[22] Humayun M, E. de Juan J, J. Weiland, et al. (1999) Pattern electrical stimulation of the human retina. Vision Res 1999; 39: 2569-76.

[23] Humayun MS, Freda R, Fine I, et al. (2005) Implanted intraocular retinal prosthesis in six blind subjects Proc of the ARVO annual meeting; 2005; Fort Lauderdale (Florida) 2005. p. 1140-45.

[24] Peachey NS, Chow AY (1999) Subretinal implantation of semiconductor based photodiodes: progress and challenges. J Rehabil Res Dev 1999; 36: 372-8.

[25] Rizzo JF III, Wyatt J, Loewenstein J, Kelly Shawn, Shire D (2003) Methods and Perceptual Thresholds for Short-Term Electrical Stimulation of Human Retina with Microelectrode Arrays. Investigative Ophthalmology & Visual Science vol.44, no. 12, pp.:5355-5361.

[26] Schubert MB, Stelzle M, Graf M, et al. (1999) Subretinal implants for the recovery of vision. Proc of the IEEE Int'l Conf on Systems, Man, and Cybernetics 1999; 376-81.

[27] Zhao Y et al. (2006) Micro-stimulator Design for Visual Prosthesis based on Optic Nerve Stimulation. International Symposium on Biophotonics, Nanophotonics and Metamaterials, pp.139-142.

[28] Shire DB, Kelly SK, Jinghua Chen Doyle P, Gingerich MD, Cogan SF, Drohan WA, Mendoza O, Theogarajan L, Wyatt JL, Rizzo JF (2009) Development and Implantation of a Minimally Invasive Wireless Subretinal Neurostimulator. IEEE transaction on Biomedical Engineering, vol. 56, no 10:2502-2511, doi. 10.1109/TBME.2009.2021401.

[29] Saiful A. Joarder, Socrates Dokos, Gregg J. Suaning, ,Nigel H. (2007) Finite Element Bidomain Model of Epiretinal Stimulation Lovell Proceedings of the

29th Annual International Conference of the IEEE EMBS Cité Internationale, Lyon, France August 23-26, 2007.

[30] Peyman G, Chow AY, Liang C, Chow VY, Perlman JI, Peachey NS (1998) Subretinal semiconductor microphotodiode array. Ophthalmic Surg Lasers 1998; 29: 234-41.

[31] Li J, Ng HT, Cassell A, Fan W, Chen H, Ye Q, Koehne J, Han J, Meyyappan M (2003) Carbon Nanotube Nanoelectrode Array for Ultrasensitive DNA Detection, Nano Letters, 2003, 3 (5), pp 597–602, doi 10.1021/nl0340677.

[32] Meyyappan (2004) M, Carbon nanotubes: science and applications, CRC Press; 1 edition , 2004.

[33] Nguyena P, Meyyappan M, Yiu SC (2010) Applications of Nanobiotechnology in Ophthalmology – Part I. Ophthalmic Res 2010;44:1-16, doi: 10.1159/000279436.

[34] Shalek AK, Robinson JT, Karp ES, Seok Lee J, Ahn DR, Yoon MH, Sutton A, et al. (2010) Vertical silicon nanowires as a universal platform for delivering biomolecules into living cells. Biological Sciences – Applied Biological sciences. doi:10.1073/pnas.0909350107

[35] Shoval A, Adams C, Pur MD, Shein M, Hanein Y, Sernagor E (2009) Carbon nanotube electrodes for effective interfacing with retinal tissue. Frontiers in Neuroengineering, vol 2, art 4, doi: 10.3389/neuro.16.004.2009

[36] Gabriel G, Gómez R, Bongard M, Benito N, Fernández E, Villa R (2008) Easily made single-walled carbon nanotube surface microelectrodes for neuronal applications. Biosensors and Bioelectronics. Volume 24, Issue 7, 15 March 2009, 1942-1948

[37] Palanker DV, Vankov A, Huie P, Baccus S. (2005) Design of highresolution optoelectronic retinal prosthesis. J Neural Eng 2005; 2:S105-S20.

[38] Shen J, Wang W, Chen Q, Wang M, Xu1 S, Zhou Y, Zhang XX (2009) The fabrication of nanoelectrodes based on a single carbon nanotube. Nanotechnology 20 (2009) 245307 (6pp), doi:10.1088/0957-4484/20/24/245307.

[39] Rutten WLC, van Wier HJ, Put JHM (1991) Sensitivity and Selectivity of Intraneural Stimulation Using a Silicon Electrode Array. IEEE transaction on Biomedical Engineering, vol. 38, no 2, pp.: 192-198.

[40] Cajal SRY (1911) Axial organization of the retina. Histologie Du Système Nerveux de lHomme et Des Vertébrés, Maloine, Paris, 1911.

[41] Taglietti, Casella C (1997) Elementi di fisiologia e biofisica della cellula. La goliardica Pavese editore, ITALY.

[42] Cellot G, Cilia E, Cipollone S, Rancic V, Sucapane A, Giordani S, Gambazzi L, Markram H, Grandolfo M, Scaini D, Gelain F, Casalis L, Prato M, Giugliano M, Ballerini L (2009) Carbon nanotubes might improve neuronal performance by favouring electrical shortcuts. Nature Nanotechnology, Nature Nanotechnology 4, 126 - 133 (2009) doi:10.1038/nnano.2008.374.

[43] Giugliano M, Prato M, Ballerini L (2008) Nanomaterial/neuronal hybrid system for functional recovery of the CNS. Drug Discovery Today: Disease Models 5, 1:37-43.

[44] Gruner G (2006) Carbon nanotube transistors for biosensing applications. Anal Bioanal Chem (2006) 384: 322–335, doi. 10.1007/s00216-005-3400-4.

[45] Zeng Z., Yu Y, Zhang J.(2009) Electrochemical Corrosion Behavior of Carbon Nanotube-Doped Hard Chromium Coatings Electrodeposited from Cr(III) Baths. J. Electrochem. Soc., Volume 156, Issue 4, pp. C123-C126 (2009)

[46] University of Heidelberg Molecular Biotechnology (Winter 2003/2004) Modelling in molecular biotechnology Dr. M. Diehl Modelling Hodgkin-Huxley Version 1.0 Wadel, K. (2170370)

[47] Rattay F. (1999).The basic mechanism for the electrical stimulation of the nervous system. Neuroscience. 1999 Mar;89(2):335-46.

[48] Einziger PD, Livshitz LM, Mizrahi J (2005) Generalized Cable Equation Model for Myelinated Nerve Fiber. IEEE transaction on Biomedical Engineering, vol. 52, no 10, pp.:1632-1642.

[49] Hodgkin AL, Huxley AF (1952) A quantitative description of membrane current and its application to conduction and excitation in nerve. J Physiol 117:500-544.

[50] Elia S, Lamberti P, Tucci V (2009) A Finite Element Model for The Axon of Nervous Cells. In: COMSOL Europe Conference 2009. Milan, Italy pp.1- 7

[51] COMSOL Multiphysics Modeling Guide (version 3.4).

[52] Egiziano L, Elia S, Lamberti P, Tucci V (2008) FEM Simulation of neuron signal transmission performed by exploiting membrane non-linearity. In proceeding of the 13th Biennial IEEE Conference on Electromagnetic Field Computation (CEFC2008). May 11-15, 2008, ATHENS, GREECE, pp.1-2.

[53] Keynes RD (1951) The ionic movements during nervous activity. J Physiol 114:119-150.

[54] Moulin C (2006), Institut National des Sciences Appliquées de Lyon, Contribution à l'étude et à la réalisation d'un système électronique de mesure et excitation de tissu nerveux à matrices de microélectrodes.

[55] Hodgkin AL, Katz B (1949) The effect of temperature on the electrical activity of the giant axon of the squid. J Physiol 109:240-249.

[56] Malmivuo, Plonsey R (1995) Bioelectromagnetism. Principles and Applications of Bioelectric and Biomagnetic Fields, Oxford University Press.

[57] Elia S, Lamberti P, Tucci V (2010) Influence of Uncertain Electrical Properties on the Conditions for the Onset of Electroporation in an Eukaryotic Cell. IEEE Transaction on Nanobioscience, vol. 9, No. 3, 2010, pp. 204-212.

[58] Talukder MI, Siy P, Auner GW (2008) High Resolution Implantable Microsystem and Probe Design for Retinal Prosthesis, The Open Ophthalmology Journal. 2008; 2: 77–90, doi: 10.2174/1874364100802010077.

[59] Zhang (2004) Advance Numerical Prototyping Methods in Modern Engineering Applications, Proceedings of the 5th International Conference on Thermal and Mechanical Simulation and Experiments in Microelectronics and Microsystems, 2004. EuroSimE 2004.

[60] Montgomery DC (1995) Design and analysis of experiments. 5th edition, Wiley, New York.